

2016

Implementation of Solar Irradiance Forecasting Using Markov Switching Model and Energy Management System

Ayush Shakya
South Dakota State University

Follow this and additional works at: <http://openprairie.sdstate.edu/etd>

 Part of the [Power and Energy Commons](#)

Recommended Citation

Shakya, Ayush, "Implementation of Solar Irradiance Forecasting Using Markov Switching Model and Energy Management System" (2016). *Theses and Dissertations*. 1068.
<http://openprairie.sdstate.edu/etd/1068>

This Thesis - Open Access is brought to you for free and open access by Open PRAIRIE: Open Public Research Access Institutional Repository and Information Exchange. It has been accepted for inclusion in Theses and Dissertations by an authorized administrator of Open PRAIRIE: Open Public Research Access Institutional Repository and Information Exchange. For more information, please contact michael.biondo@sdstate.edu.

IMPLEMENTATION OF SOLAR IRRADIANCE FORECASTING USING MARKOV
SWITCHING MODEL AND ENERGY MANAGEMENT SYSTEM

BY

AYUSH SHAKYA

A thesis submitted in partial fulfillment of the requirements for the

Master of Science

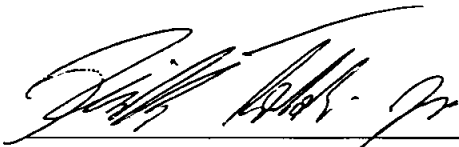
Major in Electrical Engineering

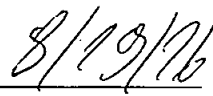
South Dakota State University

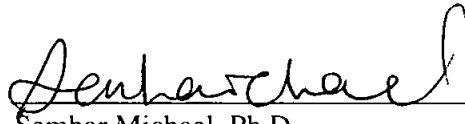
2016

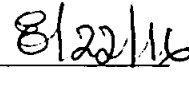
IMPLEMENTATION OF SOLAR IRRADIANCE FORECASTING USING MARKOV
SWITCHING MODEL AND ENERGY MANAGEMENT SYSTEM

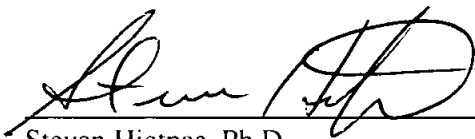
This thesis is approved as a creditable and independent investigation by a candidate for the Master of Science in Electrical Engineering degree and is acceptable for meeting the thesis requirements for this degree. Acceptance of this thesis does not imply that the conclusions reached by the candidates are necessarily the conclusions of the major department.

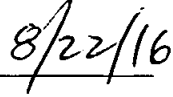

Reinaldo Tonkoski, Ph.D.
Thesis Advisor

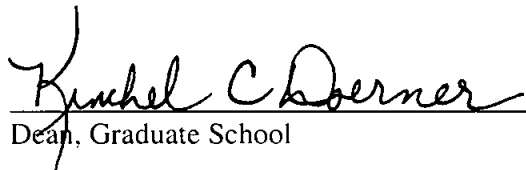

Date

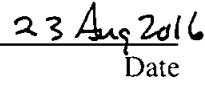

Semhar Michael, Ph.D.
Thesis Co-advisor


Date


Steven Hietpas, Ph.D.
Head, Electrical Engineering and Computer Science


Date


Rachel C. Doerner
Dean, Graduate School


Date

ACKNOWLEDGEMENTS

I would like to express my sincere gratitude towards my research advisors, Dr. Reinaldo Tonkoski and Dr. Semhar Michael for their guidance, teaching, and sharing their profound knowledge and believing in me from the very beginning of the thesis research. Without their persistent support and guidance throughout the various stages of the study, it would not have come out in such an ease. Their guidance and crucial advice have been helpful not only in the development of the technical aspects of my field, but also have helped me to prosper as an individual. Moreover, I would like to thank Dr. Timothy Hansen for being in my committee and reviewing my work.

I am very much thankful to South Dakota State University, Department of Electrical Engineering & Computer Science for providing me the necessary resources for this research work. I am grateful to Dr. Qiquan Qiao for his support in pursuing my Master's degree. I take this opportunity to appreciate Dan Flaskey for helping me to manage the necessary resources in the laboratory.

I am highly obliged to my research group members, Dr. Santosh Chalise and Shaili Nepal for their valuable insight into my research work and to all my friends and the people in the SDSU, who helped me in my research and made my study memorable and fulfilling one.

Last but not least, I would like to especially thank my father, Opil Shakya, mother, Sarina Shakya and brother, Chirayu Shakya for their continuous love, support and motivation. I would not have been able to face the challenges without their encouragement and suggestions.

CONTENTS

ABBREVIATIONS	vii
LIST OF FIGURES	ix
LIST OF TABLES	xiii
ABSTRACT	xiv
CHAPTER 1 INTRODUCTION	1
1.1 Background	1
1.2 Previous work	6
1.3 Motivation	12
1.4 Objective	12
1.5 Thesis outline	13
CHAPTER 2 THEORY	14
2.1 Microgrids	14
2.2 Remote microgrids	15
2.2.1 Centralized EMS	17
2.3 Components of a typical microgrid	21
2.3.1 Natural gas generators	21
2.3.2 PV systems	24
2.3.3 Energy storage systems	30

2.3.4	Hybrid inverter/chargers	33
2.3.5	Loads	35
2.4	Scheduling and optimization	36
2.4.1	Deterministic methods	38
2.4.2	Stochastic methods	39
2.5	Solar irradiance	39
2.5.1	Clear Sky Irradiance	40
2.6	Some of the terminologies used in forecasting irradiance	40
2.6.1	Latitude (ϕ)	41
2.6.2	Declination angle (δ)	41
2.6.3	Hour angle (ω)	42
2.6.4	Zenith angle (θ_z)	44
2.6.5	Solar altitude or elevation angle (α)	44
2.6.6	Solar azimuth angle (ψ)	45
2.6.7	Air Mass (AM)	45
2.7	Fourier basis expansion	45
2.8	Markov switching model (MSM)	46
2.9	Bayesian Information Criterion (BIC)	51
2.10	Standard error metrics for measuring overall performance of forecasting	51
2.11	EMS Algorithm	52
CHAPTER 3 PROCEDURES		54
3.1	Solar irradiance forecasting using MSM	54

3.1.1	Dataset	55
3.1.2	Calculation of clear sky irradiance	57
3.1.3	MSM fit and forecasting	58
3.2	Real-time implementation of solar irradiance forecasting using MSM	60
3.2.1	Photovoltaic panels as irradiance sensors	60
3.2.2	Real-time irradiance measurement using OPAL-RT	62
3.3	Experimental setup for testing EMS (optimization of energy resources) in the microgrid testbed	66
3.4	Optimization model	68
3.5	Procedure for implementing EMS in the testbed	73
CHAPTER 4 RESULTS AND ANALYSIS		78
4.1	Validation of the forecasting method using historical irradiance data	78
4.2	Implementation of solar irradiance forecasting in real-time digital simulator at microgrid research laboratory	86
4.2.1	Irradiance data acquisition using PV panels as sensors	86
4.2.2	Irradiance forecasting at the laboratory	86
4.3	Implementation of EMS in the microgrid testbed	88
CHAPTER 5 CONCLUSIONS		100
5.1	Conclusions	100
5.2	Future work	102
REFERENCES		103

ABBREVIATIONS

AC	Alternating Current
AI	Artificial Intelligence
ALB	Automatic Load Bank
BMS	Battery Management System
BOS	Balance of System
CAN	Controller Area Network
CEMS	Centralized Energy Management System
COTS	Commercial Off-The-Shelf
DC	Direct Current
DEMS	Distributed Energy Management System
DERs	Distributed Energy Resources
ECMWF	European Centre for Medium-Range Weather Forecasts
EMS	Energy Management System
ESS	Energy Storage System
HEMS	Hybrid Energy Management System
I/O	Input/Output
IEA	International Energy Agency
MAPE	Mean Absolute Percentage Error
MGCC	Microgrid Control Controller
MPPT	Maximum Power Point Tracking

MSM	Markov Switching Model
NRMSE	Normalized Root Mean Square Error
PHIL	Power Hardware-in-the-Loop
PV	Photovoltaic
SOC	State of Charge
SOH	State of Health
SRH	Sunrise Hour
SSH	Sunset Hour
STC	Standard Test Conditions

LIST OF FIGURES

Figure 1.1.	Microgrid layout.	4
Figure 2.1.	A typical microgrid.	14
Figure 2.2.	Remote microgrid projects by region [50].	16
Figure 2.3.	A typical architecture of CEMS.	18
Figure 2.4.	OPAL-RT simulator OP5600.	20
Figure 2.5.	Basic components of natural gas generator [55].	21
Figure 2.6.	Electric power generation from gas turbine [56].	22
Figure 2.7.	Plot of generator fuel consumption versus load for 10.4 kW natural gas generator (Kohler 12RES).	23
Figure 2.8.	Plot of generator fuel efficiency versus load for 10.4 kW natural gas generator (Kohler 12RES).	24
Figure 2.9.	Natural gas generator (Kohler 12RES).	24
Figure 2.10.	A simple PV system [59].	25
Figure 2.11.	IV characteristics of PV cell under different illumination levels [61].	26
Figure 2.12.	Solar irradiance and PV power output for January 1, 2012 for Brook- ings, South Dakota from 4.1 kW PV array.	28
Figure 2.13.	Solar panels (Evergreen ES-A-205-FA3) on the rooftop of Daktronics Engineering Hall, SDSU.	28
Figure 2.14.	SMA Sunny Boy (SB-5000US) solar inverter.	29
Figure 2.15.	Lithium-ion rechargeable battery.	32
Figure 2.16.	Xantrex hybrid inverter/charger (XW6048 120/240 60).	34

Figure 2.17. Block diagram of CAN.	35
Figure 2.18. Automatic Load Bank (Cannon L-63).	36
Figure 2.19. Screenshot of load profile manager software.	36
Figure 2.20. Declination angle.	41
Figure 2.21. Hour angle, along with altitude and azimuth angles [60].	42
Figure 2.22. Daylight hour throughout a year.	43
Figure 2.23. Zenith, altitude and azimuth angles for northern latitude.	45
Figure 2.24. Flowchart of MSM.	47
Figure 2.25. Probability transition for a model with 3 states.	50
Figure 2.26. EMS with schedule and dispatch layers [84].	53
Figure 3.1. Block diagram for solar irradiance forecasting using MSM.	54
Figure 3.2. Solar irradiance for years from 2001 to 2012.	56
Figure 3.3. CSI for a year along with actual irradiance for the year 2001.	56
Figure 3.4. CSI and actual solar irradiance from January 1 through January 5, 2001.	57
Figure 3.5. Illustration of solar irradiance incident on a tilted surface ($S_{incident}$), solar irradiance incident on horizontal surface ($S_{horizontal}$) and solar irradiance measured perpendicular to the module surface (S_{module}) [88].	61
Figure 3.6. Block diagram of implementation of irradiance forecasting in OPAL- RT real-time digital simulator.	63
Figure 3.7. MATLAB/Simulink model for measuring solar irradiance with solar panels as sensors.	65
Figure 3.8. Master (SM) subsystem for the model shown in Figure 3.7.	65
Figure 3.9. Console (SC) subsystem for the model shown in Figure 3.7.	66

Figure 3.10. Microgrid testbed.	67
Figure 3.11. Inverter/charger connection with battery and AC bus.	68
Figure 3.12. Plot of generator fuel consumption versus load for the natural gas generator (Kohler 12RES).	72
Figure 3.13. Plot of generator fuel consumption versus load for the natural gas generator (Kohler 12RES).	74
Figure 3.14. Scheduling and dispatch procedures carried out in the laboratory.	74
Figure 3.15. Screenshot of load profile manager software.	75
Figure 3.16. MATLAB/Simulink model for dispatching the scheduled output from the optimization tool.	77
Figure 4.1. Irradiance variation for August 16, 2011.	79
Figure 4.2. Irradiance variation for August 15, 2011.	79
Figure 4.3. Irradiance variation for May 14, 2008.	80
Figure 4.4. Irradiance variation for May 13, 2008.	81
Figure 4.5. Irradiance variation for July 24, 2012.	82
Figure 4.6. Irradiance variation for July 23, 2012.	82
Figure 4.7. Boxplot of monthly RMSE for the year 2001.	83
Figure 4.8. Boxplot of monthly MAPE for the year 2001.	84
Figure 4.9. RMSE for years 2001 to 2005.	84
Figure 4.10. Plot of difference between hourly forecasted and actual irradiance for four different months of year 2001.	85
Figure 4.11. Solar irradiance data logged through OPAL-RT in real-time with solar panels as sensors for 60 seconds.	87

Figure 4.12. Irradiance variation for June 10, 2015.	87
Figure 4.13. Irradiance variation for June 9, 2015.	88
Figure 4.14. Scheduled Power Output.	89
Figure 4.15. SOC of the battery throughout the day.	91
Figure 4.16. Generator power, load power and battery power.	92
Figure 4.17. Comparison between theoretical and actual fuel consumed by the gen- erator.	93
Figure 4.18. Plot of battery voltage versus time.	95
Figure 4.19. Plot of battery current versus time.	95
Figure 4.20. Plot of generator frequency versus time.	96
Figure 4.21. Plot of generator RMS voltage versus time.	96
Figure 4.22. Plot of generator RMS current versus time.	97
Figure 4.23. Plot of load frequency versus time.	98
Figure 4.24. Plot of load RMS voltage versus time.	98
Figure 4.25. Plot of load RMS current versus time.	99

LIST OF TABLES

Table 1.1.	Electricity access in 2013-regional aggregates [3].	1
Table 2.1.	Evergreen solar panel specifications [63].	29
Table 2.2.	Lithium iron phosphate battery specifications [66].	33
Table 3.1.	BIC scores for fitted models	59
Table 3.2.	Coefficients of fuel consumption curve of 10.4 kW generator.	72
Table 3.3.	Twenty four hour original load of January 3, 2012 from Nemiah Valley microgrid in Canada and scaled load used in the experiment	76
Table 4.1.	RMSE for years 2001 to 2005	85
Table 4.2.	Scheduled output obtained from optimization in CPLEX	90
Table 4.3.	Natural gas generator fuel consumption	94

ABSTRACT

IMPLEMENTATION OF SOLAR IRRADIANCE FORECASTING USING MARKOV
SWITCHING MODEL AND ENERGY MANAGEMENT SYSTEM

AYUSH SHAKYA

2016

Photovoltaic (PV) systems integration is increasingly being used to reduce fuel consumption in diesel-based remote microgrids. However, uncertainty and low correlation of PV power availability with load reduce the benefits of PV integration. These challenges can be handled by introducing reserve, which however leads to increased operational cost. Solar irradiance forecasting helps to reduce reserve requirement, thereby improving the utilization of PV energy. In this thesis, a new solar irradiance forecasting method for remote microgrids based on the Markov Switching Model (MSM) is presented. This method uses locally available data to predict one-day-ahead solar irradiance for scheduling energy resources in remote microgrids. The model considers the past solar irradiance data, the Clear Sky Irradiance (CSI), and the Fourier basis functions to create linear models for three regimes or states: high, medium, and low energy regimes for a day corresponding to sunny, mildly cloudy, and extremely cloudy days, respectively. The case study for Brookings, SD, discussed in this thesis, resulted in an average Mean Absolute Percentage Error (MAPE) of 31.8% for five years, 2001 to 2005, with higher errors during summer months than during winter months.

The solar irradiance forecasting method was implemented in OPAL-RT real-time digital simulator using PV panels as sensors. For forecasting irradiance, the first four

hours of irradiance data in the morning are required. These data were measured using the solar panels rather than pyranometers as the sensors . A case study for real-time irradiance forecasting in Brookings on June 9, 2015 showed RMSE and MAPE of $131.08 \text{ W}/\text{m}^2$ and 45.45%, respectively.

The improvement of renewable integration is the future and present prospects for power utilization. Microgrids experience several constraints such as integration of intermittent renewable sources, costlier reliability improvements, restricted expansion of the microgrid system, growth in load, etc. Hence, more research in this field of study is required and a complete laboratory scale microgrid testbed is needed for experimenting different types of microgrid topologies and for studying the coordination of individual components with a well-defined energy management scheme. In this thesis, the development of a laboratory scale single-phase microgrid testbed along with the implementation of microgrid's Energy Management System (EMS) are discussed. The testbed was developed using central controller and Commercial Off-The-Shelf (COTS) equipment. The EMS comprised of double layers: schedule layer and real-time dispatch layer. A case study conducted for the implementation of the EMS showed that the difference in the scheduled and the dispatched powers were handled by the generator and the energy storage system themselves.

CHAPTER 1 INTRODUCTION

1.1 Background

According to the International Energy Agency (IEA) , "Access to electric energy is an indispensable element of sustainable human development" [1]. It contributes not only to the economic growth and household incomes, but also to the improved quality of life with better health services and education. In the absence of sufficient access to electricity with good power quality and reliability, poor countries can further remain in poverty, underdevelopment and social instability. A crucial element in the broader process of human development, involving urbanization, industrialization and increased personal mobility, is the increased use of electricity by households.

Approximately 17% of global population - 1.2 billion people - lack access to electricity in 2013 [2]. More than 95% of the global population without any access to electricity, live in sub-Saharan Africa and developing countries of Asia. Majority of them are in remote locations (around 80% of the world population total). Table 1.1 shows electricity access by region in the year 2013.

Table 1.1. Electricity access in 2013-regional aggregates [3].

Region	Population Without Electricity (millions)
Africa	635
<i>North Africa</i>	<i>1</i>
<i>Sub-Saharan Africa</i>	<i>634</i>
Developing Asia	526
<i>China</i>	<i>1</i>
<i>India</i>	<i>237</i>
Latin America	22
Middle East	17

One of the solutions to provide power to remote locations is remote microgrids with conventional energy sources, renewable energy sources and energy storage systems. According to the U.S. Department of Energy Microgrid Exchange Group, "A microgrid is a group of interconnected loads and distributed energy resources within clearly defined electrical boundaries that acts as a single controllable entity with respect to the grid. A microgrid can connect and disconnect from the grid to enable it to operate in both grid-connected or island-mode" [4]. Similarly, according to CIGRÉ C6.22 Working Group, Microgrid Evolution Roadmap, "Microgrids are electricity distribution systems containing loads and distributed energy resources, (such as distributed generators, storage devices, or controllable loads) that can be operated in a controlled, coordinated way either while connected to the main power network or while islanded" [5]. The isolated grid is known as remote microgrid and it is widely recognized as the remote area electrification technology for the 21st century. Microgrids have a growing range of applications in both civilian and military aspects. For instance, they can be used as research or simulation mediums to test technologies on a small scale or they can be constructed to provide electrical power in remote areas without access to a centralized power grid. Another use would be in temporary military bases. Whatever the application, microgrids have a definite place in the world, but also challenges.

The dominant source of electrical energy for remote communities are diesel fuel gensets. Therefore, access to fuel is required in these communities. Generally, the community supply comes through road access or by air. This leads to the increment in the operational cost (mainly fuel and transportation). Photovoltaic (PV) systems utilization is increasing rapidly in such diesel-based remote microgrids to displace fuel, which is the

main operational cost [6]. However, the load does not always correlate with PV power availability, and the full potential of PV cannot be utilized. A case study in Canada [7] showed that the installation of PV systems which supplied about 14% of the yearly energy needs of a PV-diesel hybrid microgrid resulted in 5% reduction in fuel consumption. A similar study showed 3.3% reduction in fuel consumption with the addition of PV systems which supplied about 14% of the yearly energy needs [8]. There are two basic challenges of PV power: uncertainty, and variability. The challenges of integrating PV systems into the microgrids can be handled by using large reserves to ensure reliable operation.

However, this large reserve requirement actually increases the operational cost because the diesel generators are now forced to operate at lower efficiencies to provide the required reserve margin. In such cases, PV forecasting is needed to schedule the energy resources, and improve the PV energy utilization. With PV forecasting, the Energy Management Systems (EMS) can better manage the dispatchable resources to improve energy efficiency in the microgrid. The integration of renewable energy sources in a microgrid system with Distributed Intelligent EMS (DIEMS) was presented in [9]. Forecasted renewable energy was used in the energy management. With the use of forecasts in the EMS, the operating cost of the system decreased, while the battery lifetime improved. The total cost savings for the case studied was estimated to be 24.83% with DIEMS. Proper scheduling of microgrid components, such as battery, generator, and PV power output forecasting in the scheduling stage, is the key to reducing the cost of operation of remote microgrid [10].

PV power output is directly related to solar irradiance at ground level, so solar irradiance forecasting is the basis of solar power forecasting. The first and most important step in most of the solar power prediction systems is the forecasting of Global Horizontal

Irradiance (GHI) [11], which is the total amount of irradiance falling on a surface horizontal to the surface of the earth.

A typical layout of microgrid with a central controller is shown in Figure 1.1. The central controller is used for communication with the microgrid resources [12]. The central EMS contains required information and details related to various microgrid components. These specifics include forecasted values of non-dispatchable sources, loads, operational limits of dispatchable sources, battery's State of Charge (SOC) and status of the components in terms of ON and OFF states [13]. For real-time operation and optimization of the EMS, a fast and reliable communication link is required.

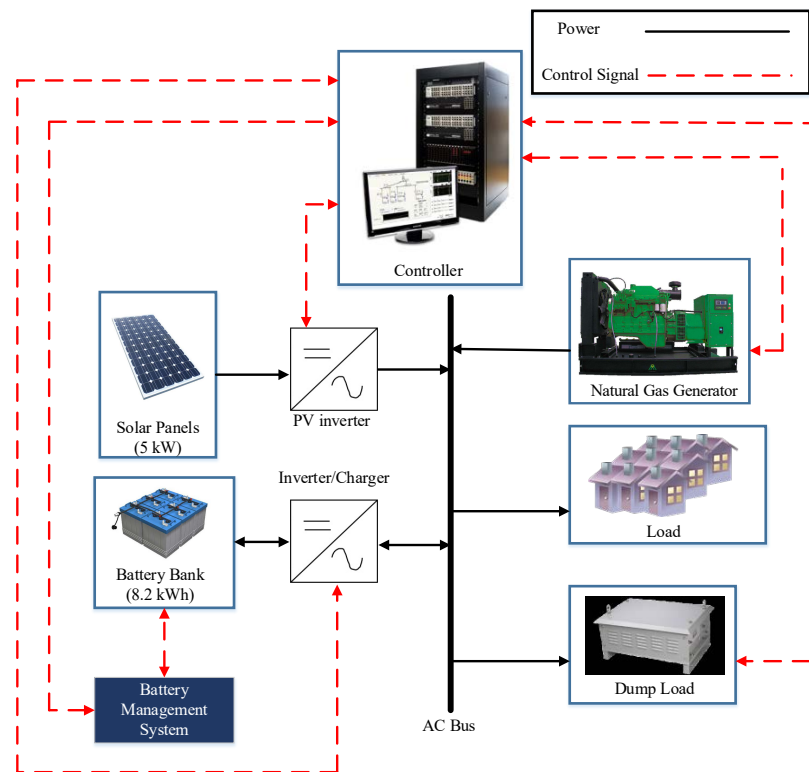


Figure 1.1. Microgrid layout.

The improvement of renewable integration is the future and present prospects for power utilization. Microgrids experience several constraints such as integration of

intermittent renewable sources, costlier reliability improvements, restricted expansion of the microgrid system, growth in load, conflict in policy objective, etc. Hence, more researches in this field of study is required and a complete laboratory scale microgrid testbed is required for conducting such researches. The microgrid testbed is needed for experimenting different types of microgrid topologies and for studying the coordination of individual components with a well defined energy management scheme. There is no any accepted benchmark for microgrid testbed [14]. There are still researches going on in this subject. The CERTS microgrid, located at Columbus, Ohio and operated by American Electric Power, is the most dominant commercialized test system [15].

Most of the solar irradiance forecasting techniques require various information, like weather and satellite data which may not be readily available in remote areas, or may require additional sensors. This thesis proposes a novel solar irradiance forecasting technique for remote microgrids using the Markov Switching Model (MSM), which makes use of past solar irradiance data at the location of the microgrid for day-ahead forecasting. It considers the Clear Sky Irradiance (CSI) and the Fourier basis functions to create linear models for three regimes or states: high, medium, and low energy regimes for a day corresponding to sunny, mildly cloudy, and extremely cloudy days, respectively. The historical irradiance data is required only for fitting the model. Once it is fit, any other information like past irradiance data or weather and satellite data are not needed. So, this method is well-suited for remote microgrids, which do not have access to communication infrastructure.

1.2 Previous work

Due to rapid growth of PV integration in recent years, a number of solar irradiance forecasting methods have been developed. Depending on the forecast horizon, various input data and forecasting models are suitable. Solar irradiance forecasting methods can be broadly categorized as physical, statistical, Artificial Intelligence (AI) and hybrid methods [16]. Physical methods use PV models, NWP models and satellite images to predict solar irradiance and PV generation [17], [18]. There are basically three physical methods: Numerical Weather Prediction (NWP), Total Sky Imagery (TSI) and satellite imagery methods for cloud observations [19], [20]. These methods utilize information such as weather data, satellite images for forecasting, which may not be readily available in remote areas.

Statistical methods are based on time series models. These methods primarily depend upon historical data for fitting statistical models for solar irradiance forecasting. They are persistence forecasting, time series, and Model Output Statistics (MOS) method. Persistence forecasting is a simple and effective forecasting method for short-term forecasting of about 1 hour [21], based on the current solar power output. As the name implies, it supposes that solar irradiance at time $t + 1$ is best predicted by its value at time t i.e. $\hat{X}_{t+1} = X_t$. Time series method is used for long-term solar irradiance forecasting which makes use of various models such as Autoregressive (AR) [22], Autoregressive Moving Average (ARMA) [21] and Autoregressive Integrated Moving Average (ARIMA) models [23]. A large amount of data is required for developing statistical correlations and ensuring accuracy. This implies that statistical methods are not available immediately for

locations without any prior local measurements. MOS method interprets numerical model output and produces the specific forecasts.

AI methods use advanced techniques like Artificial Neural Networks (ANNs) whereas hybrid methods are combination of physical, statistical and AI methods [16]. It takes advantages of various forecasting models. Similar to statistical methods, these methods require large datasets.

Yona et al. in 2007, used neural network methods for one-day-ahead solar power forecasting based on insolation forecasting. In this method, the data required for forecasting were insolation, temperature and relative humidity. They used neural network models such as Feed-Forward Neural Network (FFNN), Radial Basis Function Neural Network (RBFNN) and Recurrent Neural Network (RNN). Mean Absolute Percentage Error (MAPE) were calculated to be in the range of 15.93% to 17.33% using FFNN, 15.1% to 17.21% using RBFNN and 15.20% to 16.86% using RNN. The limitation of this method is that meteorological data are required which may not be readily available in remote locations [24].

Lorenz et al. in 2009, presented a forecasting approach to predict regional PV power output based on forecasts upto 3 days ahead provided by the European Center for Medium-Range Weather Forecasts (ECMWF) . They calculated Normalized Root Mean Square Error (NRMSE) of 36% for one day-ahead irradiance forecasting. The data required for this approach was weather data from ECMWF which may not be accessible in the rural areas [25].

Huang et al. in 2010, compared the two methods of solar power forecasting method, namely physical methods and statistical methods. The physical model was based on the

construction of PV systems and the statistical method was based on historical data with the application of neural network. In this paper, the impact of input data, such as irradiance, air temperature, humidity, cloudiness and position of the sun, was studied for both the forecasting methods. They calculated NRMSE for both the methods. It was calculated to be in the range of 10% to 16% for the physical method and 10% to 15% for the neural network model. They concluded that real-time measured irradiance data can be considered in the input model so as to improve the forecasting performance [26].

Mellit et al. in 2010, proposed a day-ahead solar irradiance forecasting method using Multilayer Perceptron (MLP) taking mean daily irradiance and air temperature as the input parameters. They used dataset from July 1, 2008 to May 23, 2009 and Nov 23, 2009 to Jan 24, 2010, collected in Trieste, Italy. The correlation coefficient was calculated in the range of 98% to 99% for sunny days and 94% to 96% for cloudy days [27].

Chen et al. in 2011, proposed a one-day-ahead PV power forecasting based on weather type classification using advanced statistical method for solar power forecasting based on Artificial Intelligence (AI). This method requires input past power measurements and solar irradiance forecasts, relative humidity and temperature at the location of the PV power system which may not be locally available in the remote areas. To classify the local weather type of 24 hour ahead provided by the online meteorological services, a Self-Organized Map (SOM) is trained. This method calculated MAPE in the range of 8.29% to 10.8% on sunny days, 6.36% to 8.89% on cloudy days and 24.16% to 54.44% on rainy days [28].

Huang et al. in 2012, presented an overview of the existing solar forecasting models and evaluated them. Basically, ARMA model and persistence model were used for

forecasting solar generation within the vicinity of University of California, Los Angeles (UCLA) Smart Grid Energy Research Center (SMERC). The historical solar radiation data were taken from SolarAnywhere in the forecasting procedures. System Advisor Model (SAM) was used to get historical solar generation data from the data obtained from SolarAnywhere. They concluded that ARMA model is better for short and medium term forecasting and the persistence model is better for very short duration of time only [21].

Yona et al. in 2013, developed solar power forecasting method based on insolation forecasting for one day-ahead by using weather reported data, fuzzy theory, and RNN. The proposed technique for application of NN was trained by solar power output data based on the fuzzy theory and weather reported data. The fuzzy theory was used to determine the insolation forecast data and NN was used to train the power output smoothly [29].

Yang et al. in 2014, proposed a weather-based hybrid method for one day-ahead hourly forecasting of solar power output. The proposed method comprised of 3 stages, namely, classification, training and forecasting. In the first stage, SOM and Learning Vector Quantization (LVQ) were used for the classification of historical PV power output data. In the second stage, Support Vector Regression (SVR) was used to train the data sets for temperature, probability of precipitation and solar irradiance of defined hours. In the final stage, fuzzy inference method was used for the selection of an sufficient trained model for forecasting. This approach required weather data. In this paper, the weather information were collected from Taiwan Central Weather Bureau (TCWB). This approach calculated MAPE of 3.295% for a year from May 2012 to April 2013 [30].

Lurwan et al. in 2014, used a MATLAB/Simulink simulation based model for predicting hourly solar irradiance using modified Hottel's model using current values of

day type and geography of the location. The model required weather forecast of the day for predicting PV power output. The model output was found to have correlation coefficient of 97% with the actual irradiance data [31].

Holmgren et al. in 2014, proposed an operational hybrid forecasting system that uses input from three different sources, namely, high-resolution NWP model, satellite imagery, and a network of distributed generation PV systems and irradiance sensors. They combined a short-term forecasting method i.e. total sky images or sensor networks with both medium-term satellite imagery and long-term numerical weather modeling. These data are not accessible in remote areas and cannot be implemented in the remote microgrids [32].

Liu et al. in 2015, proposed PV power forecasting method, considering aerosol index data as an additional input parameter including historical irradiance data, temperature, humidity, and wind speed data. The index indicates the particulate matter in the atmosphere. AI was included as it was found to have strong linear correlation with solar radiation attenuation and have potential influence on the PV power generated by solar panels. Back propagation ANN approach was used for day-ahead PV power forecasting based on seasonal weather classification. The MAPE was calculated to be about 7.65% with this approach [33].

Shah et al. in 2015, developed a high-precision solar irradiance forecasting model based on Grid Point Value (GPV) datasets utilizing precipitation, relative humidity, and three-level cloud covers parameterization in the cities of Japan. During cloudy, rainy and snowy days, further the influence of liquid water path is considered in the model. The correlation coefficients were calculated to be 0.94, 0.91, 0.91, 0.89 and 0.92, for Hitachi,

Tokyo, Nagoya, Osaka, and Fukuoka, respectively when compared with 2012 datasets [34].

Among various models, MSMs have been popular in the wind power community, dealing with forecasting of output power on a large-scale offshore wind farms [35]. It was first introduced in Econometrics by [36]. The models have been commonly used in the field of speech recognition [37], and computational biology [38]. First and second order Markov chains have been used to model wind speed or wind vector [39]–[41]. A Markov switching autoregressive model is introduced in [42] to describe a long-time series data of wind speed measurement on daily and interannual bases. Similarly, a Markov switching autoregressive model with time-varying coefficients has been developed for modeling and forecasting the short-term variations in wind generation [43]. A Markov switching vector autoregressive model has also been used for simulating wind speed and direction as in [44].

In summary, there are a number of solar irradiance forecasting techniques available at present but these techniques require various information like meteorological and satellite data, which may not be available for remote locations that lack communication infrastructure. The irradiance forecasting technique that is discussed in this thesis, mostly applies to remote locations where sophisticated forecasting techniques are not the options. Further, the forecasting technique discussed in this thesis, was implemented in real-time in Microgrid Research Laboratory in the university.

For successfully operating, maintaining, and upgrading microgrids, it is necessary to ensure that researchers, scientists and engineers are experienced and educated in these fields of study. A microgrid testbed is used for research and educational purposes. Che

et al. in 2016, developed a single-phase laboratory-scale microgrid system with a PV simulator, a wind simulator, generator, battery energy storage system and power electronic interface for the connection to the AC grid [45]. Similarly, Guo et al. in 2013 combined Power Hardware-in-the-Loop (PHIL) simulation of electrical power and System-in-the-Loop (SITL) communication network with real hardware. The PHIL system interfaced with other hardware and emulated different systems connected to the testbed, such as renewable energy conversion systems, different utility grid and microgrid topologies [46]. In all these designs of microgrid testbed, simulators were used to emulate real systems like PV and wind. Further, customized power electronic devices were used rather than Commercial Off-The-Shelf (COTS) components. COTS components are cheaper and generally used. With their use in the microgrid testbed, one can know the real performance of the system with such ready-made and readily available products.

1.3 Motivation

Need solar irradiance forecasting method using easily and locally available data for 24 hour scheduling of energy resources for remote microgrids and need microgrid testbed for validation and evaluation of microgrid's EMS.

1.4 Objective

The objective of this thesis was to develop, validate and assess errors for the method to forecast PV output power based on historical data and implement the forecasting in the OPAL-RT real-time digital simulator. In addition, the objective was to implement EMS in the developed microgrid testbed. The specific tasks of this research were to:

Task 1: Develop Markov Switching Model (MSM) for forecasting irradiance using

historical data.

Task 2: Validate and analyze the forecasted data with the actual past irradiance data.

Task 3: Assess forecasting errors.

Task 4: Implement EMS comprising schedule and dispatch layers in the developed laboratory scale microgrid testbed.

1.5 Thesis outline

This thesis has been organized as follows: Chapter 2 introduces microgrids and one of the types of microgrid known as remote microgrid including its centralized EMS. The components of the solar irradiance forecasting method are also presented in this chapter. Chapter 3 details procedure for forecasting solar irradiance using historical data; real-time implementation of the solar irradiance forecasting method in OPAL-RT real-time digital simulator and the EMS in the developed microgrid testbed. Chapter 4 presents the results and analysis of the validation of the solar irradiance forecasting method, its real-time implementation in the real-time digital simulator and the EMS. Finally, chapter 5 presents the conclusions, limitations and possible future work.

CHAPTER 2 THEORY

Chapter 2 introduces microgrids, their EMS and remote microgrids. This chapter presents the components of a typical microgrid, scheduling and optimization of energy resources in the microgrid system and central controller. The theory on solar irradiance forecasting using Markov Switching Model (MSM) is also described in this chapter.

2.1 Microgrids

According to U.S. Department of Energy Microgrid Exchange Group, a microgrid is a group of interconnected loads and Distributed Energy Resources (DERs) within clearly defined electrical boundaries that acts as a single controllable entity with respect to the grid. A microgrid can connect and disconnect from the grid to enable it to operate in both grid-connected or island-mode [47]. Figure. 2.1 shows a typical microgrid. The region within the dotted line can be connected or disconnected to the main grid.

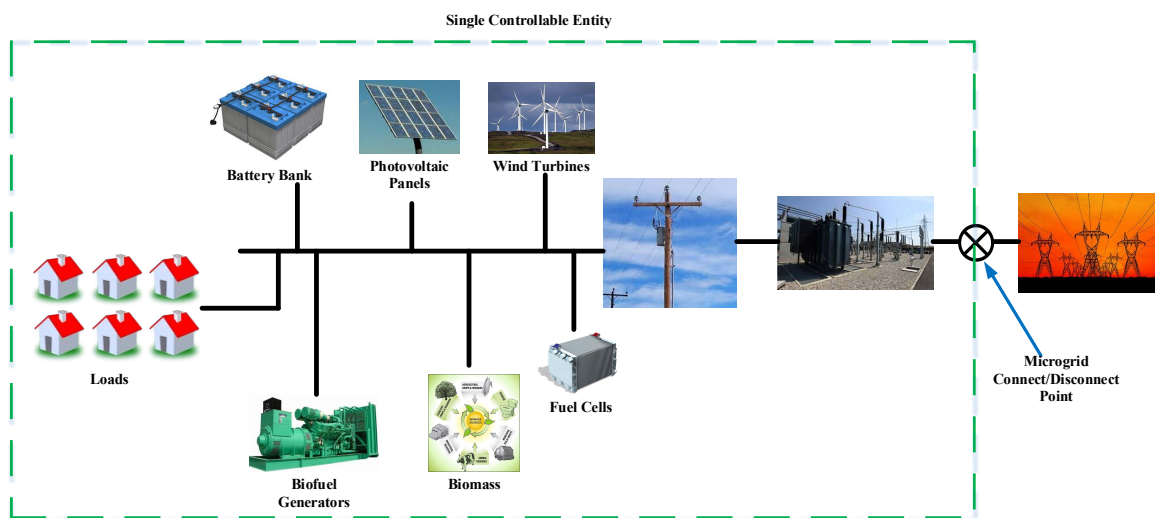


Figure 2.1. A typical microgrid.

A microgrid EMS allocates power output among the distributed generation units

optimally and serves the load economically [48]. On the basis of real-time operating conditions of the microgrid components and the system status, the EMS enables the system resynchronization response to the operating transition between interconnected and islanded modes of operation. In other words, the EMS operates and coordinates Distributed Generators (DGs), Distributed Energy Storages (DESs) and loads in order to serve reliable, sustainable and environmentally friendly energy economically. The DGs are internal combustion engines with wind turbines, photovoltaic panels, microturbines, generators and fuel cells whereas the DESs are battery banks, supercapacitors, flywheels and compressed air energy storage.

According to Pike Research, there are five categories of microgrids [4]. They are:

- Remote Microgrids
- Institutional Microgrids
- Military Base Microgrids
- Commercial and Industrial Microgrids
- Community or Utility Microgrids

Among these categories of microgrids, remote microgrid is discussed in this section.

2.2 Remote microgrids

A microgrid that is independent from a centralized grid is known as remote microgrid. This microgrid operates in an island mode at all times. One of the examples of the remote microgrid are rural village power system in Alaska or islands that usually include diesels or wind generation as in Nome, Alaska. Another example include a microgrid in Bella Coola, British Columbia. It has the objective of reducing diesel fuel by

injecting PV, wind or hydropower [4]. According to the report published by Pike Research, the remote microgrid category is the largest number of current deployments among all the microgrids [49].

The communities in the remote locations and islands are dependent upon the imported fossil fuels for most of their energy requirements. Due to the high fuel cost, the cost of the energy generation in these areas has risen tremendously. These areas are also exposed to high operation and maintenance costs including fuel transportation and bulk storage. PV and wind power technologies can replace or supplement the diesel generators. Most of the remote microgrids are now designed to reduce diesel fuel consumption by integrating PV, wind or other renewable sources of energy.

Figure 2.2 shows remote microgrid projects in the world by region.

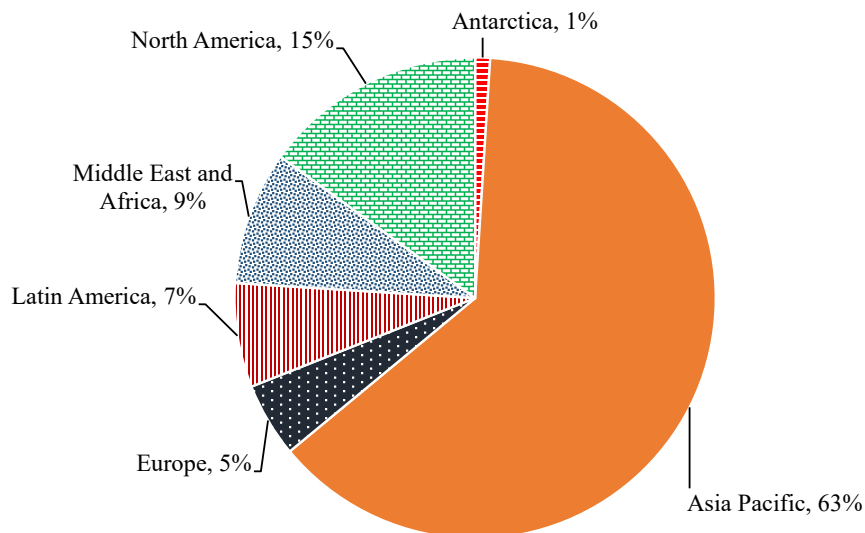


Figure 2.2. Remote microgrid projects by region [50].

One of the major challenges of microgrid operation is the management of non-dispatchable renewable energy sources such as wind and PV [51]. The selection of control strategy relies upon characteristics of resources (dispatchable or

non-dispatchable), requirements of load and distance between sources and loads. A single control strategy may not be suitable for all types of microgrids. Generally, EMS control strategies are classified into three categories [12], [51]:

- Centralized EMS (CEMS)
- Distributed EMS (DEMS)
- Hybrid EMS (HEMS)

The CEMS is described below:

2.2.1 Centralized EMS

This type of EMS has a central controller, known as Microgrid Control Controller (MGCC) which contains the relevant information of the various components of the microgrid. The information may be mode of operation, cost functions, forecasted values of the non-dispatchable sources, operational limits (maximum, minimum and efficient region) of dispatchable sources, technical characteristics, SOC of the battery, state of the components (ON or OFF), network parameters, etc. For real time operation and optimization of the system, a fast and reliable communication link is needed. In other words, a reliable two-way communication infrastructure needs to be established. The means of communication may be power line carrier, telephone lines or wireless. If the transmission distance is long, it could be expensive. Hence, this type of control is mostly appropriate for cases where all the microgrid components are located in a central station.

There are a number of advantages of CEMS. It has the ability for central monitoring and availability of a large amount of system data for optimizing the microgrid operation. Other advantages include easy implementation and standardized procedure [48]. One of the

disadvantages of CEMS is that the failure of the central controller will result in the system failure as the entire microgrid system depends upon it. Similarly, as the number of the components or control devices increases, the communication network capacity also increases and the computational ability has to be increased as well. In other words, it has high computational power and memory requirements for manipulating huge amount of data.

Figure. 2.3 illustrates a typical architecture of CEMS in which each component accepts the command and operates as per the command.

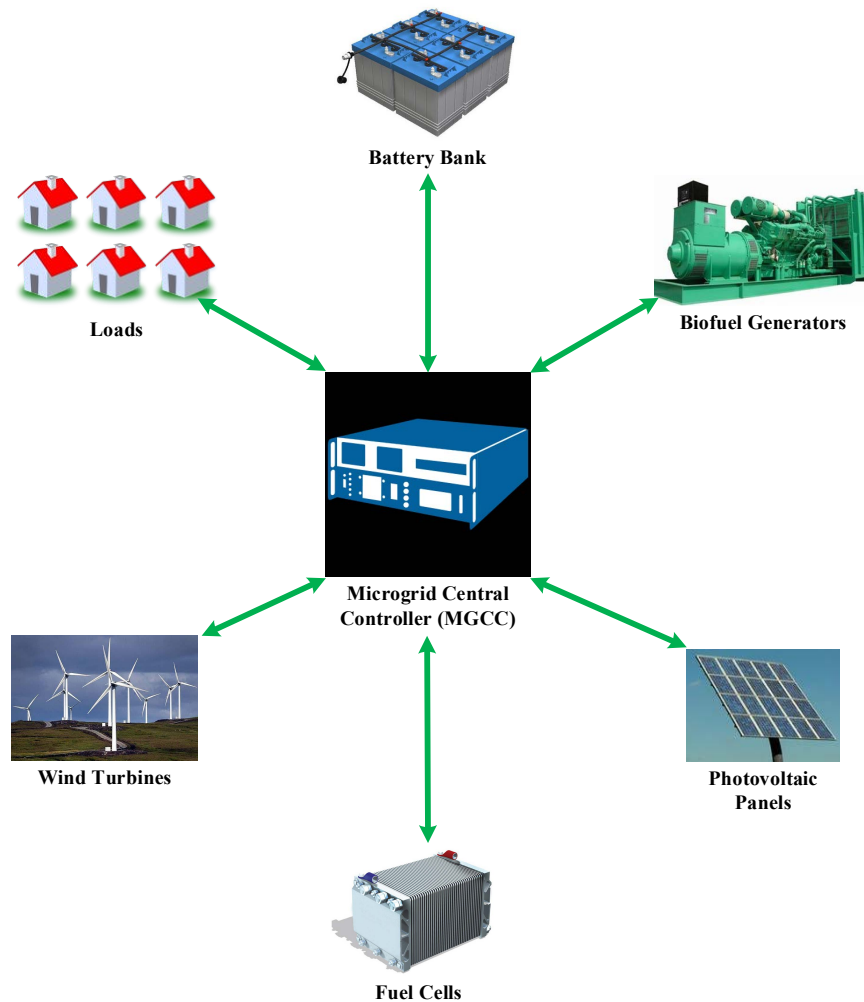


Figure 2.3. A typical architecture of CEMS.

2.2.1.1 Real-time digital simulator

There has been extensive use of simulators for planning, designing and prototyping of electrical systems in the field electrical engineering since the last three decades [52]. This is primarily due to the evolution of computer technologies. The performance of the current computer technologies has been improved and their cost has been decreased, compared to the past technologies. So, the capability of the simulators to solve complex problems in lesser time has also been improved. Moreover, the cost of the simulators is decreasing now-a-days, giving rise to the availability of the simulators to a number of users for various applications.

The offline simulation softwares such as MATLAB/Simulink, SPICE, EMTP-RV, PSS/E and PSCAD/EMTDC do not have ability to interface with the external hardware like digital controllers to the real-time simulations [53]. To have a real-time simulation, a combination of fast computer hardware with efficient software is required for parallel computation. Hence, for simulating complex circuitry with real hardware interaction, a cluster-based, parallel real-time digital simulator, OPAL-RT is developed. OPAL-RT simulator is shown in Figure 2.4. OPAL-RT provides MATLAB/Simulink based environment, called as RT-LAB which has revolutionized the way model-based design is performed. The flexibility of the RT-LAB allows it to be used in any simulation or control system application.

The hardware architecture of the OPAL-RT simulator consists of the target and the host computers [53]. The target computer is also known as target cluster or simply target and the host computer is also known as command station or simply host. There are

Field-Programmable Gate Array (FPGA)-based analog and digital input/outputs (I/Os) and high-speed communication links between the target, host and the external hardware. The target computers are computation engine for the real-time simulator. They are high-speed and high-performance general purpose computers. The target computers run on Linux operating system whereas the host computers run on either Linux or Windows operating system. The communication between the target and the host computer is done through Gigabit Ethernet link.

The software architecture of the OPAL-RT simulator consists of industry standard mathematical modeling software [53]. MATLAB/Simulink environment is used for developing power and control system models. A real-time interfacing software RT-LAB is used to coordinate all the hardware involved for the simulation. Target nodes offer eXtreme High Performance (XHP) mode to achieve high performance real-time simulation. When this mode is activated, one Central Processing Unit (CPU) is dedicated entirely to the simulation while the other CPU handles other target node tasks such as I/O operations, interrupt handling, etc.



Figure 2.4. OPAL-RT simulator OP5600.

OPAL-RT real-time digital simulator can be used as a MGCC. All the functions of the MGCC can be performed by this simulator.

2.3 Components of a typical microgrid

The components of a typical microgrid are generators, PV systems, energy storage systems, hybrid inverters/chargers and loads.

2.3.1 Natural gas generators

Natural gas generators use natural gases such as propane or methane to generate electricity. In natural gas generator, mixture of fuel and air is injected into a combustion chamber by an internal combustion engine. A piston compresses the mixture of fuel and air in the combustion chamber. The fuel is ignited by a spark plug, which drives down the piston, thereby, turning a crankshaft. It spins the generator's rotor in an electromagnetic field which then generates electricity [54]. Figure 2.5 shows four basic components of stationary gas engine and generator. They are gas engine, generator, heat recovery-heat exchanger and control panel. The gas engine is fueled by gases. When the gas is burnt in the cylinders of the engine, the force causes a crank shaft to turn within the engine. This rotation of the crank shaft causes an generator or alternator to rotate, thereby, producing electricity. The heat thus obtained from the combustion process is released from the cylinders. Figure 2.6 shows block diagram of the gas turbine electric power generation.

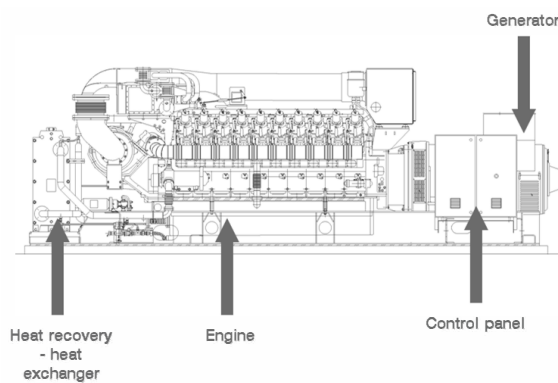


Figure 2.5. Basic components of natural gas generator [55].

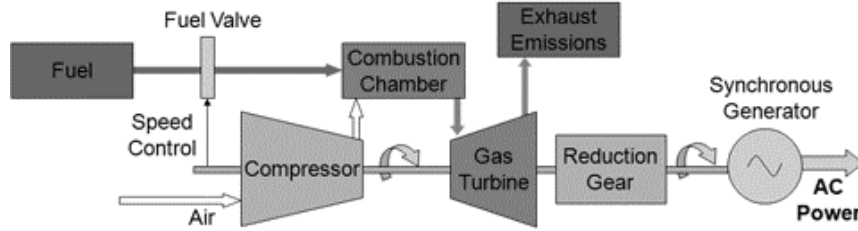


Figure 2.6. Electric power generation from gas turbine [56].

The amount of hourly fuel consumption by a natural gas generator depends upon output power of generator, which can be approximated using the quadratic expression as shown below [57]:

$$\text{Fuel consumption in volume per hour} = aP_t^2 + bP_t + c \quad (2.1)$$

where, P_t is the output electrical power of the generator in W at any time t ; a and b are the coefficients of P_t^2 and P_t , respectively and c is the constant. a , b and c are constants for a particular generator. Equation 2.1 is also known as the input-output characteristic of the generator where the input is the fuel consumption in volume per hour and the output is the electrical power which is limited by the minimal and maximal capacity of the generator, represented by P_{min} and P_{max} , respectively, as shown below:

$$P_{min} \leq P_t \leq P_{max} \quad (2.2)$$

Figure 2.7 shows plot of fuel consumption versus load for Kohler 12RES natural gas generator. It can be observed that as load increases, fuel consumption of the generator also increases. The efficiency (η) of generator is defined as the ratio of the generated electrical

energy to the energy content in the fuel i.e.

$$\eta = \frac{\text{Generated electrical energy}}{\text{Energy content in the fuel}} \times 100\% \quad (2.3)$$

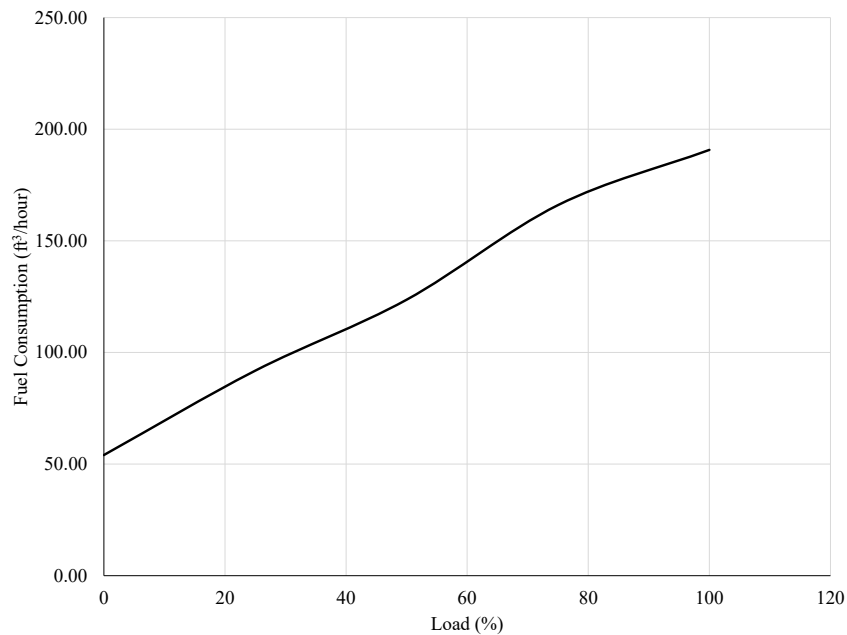


Figure 2.7. Plot of generator fuel consumption versus load for 10.4 kW natural gas generator (Kohler 12RES).

The generator operates at lower fuel efficiency at low load and it operates in maximum efficiency near the full load [58]. Figure 2.8 shows plot of generator efficiency versus load. In a power system, the load demand should be met by the generated electrical power. Similarly, voltage must be within the specified limits.

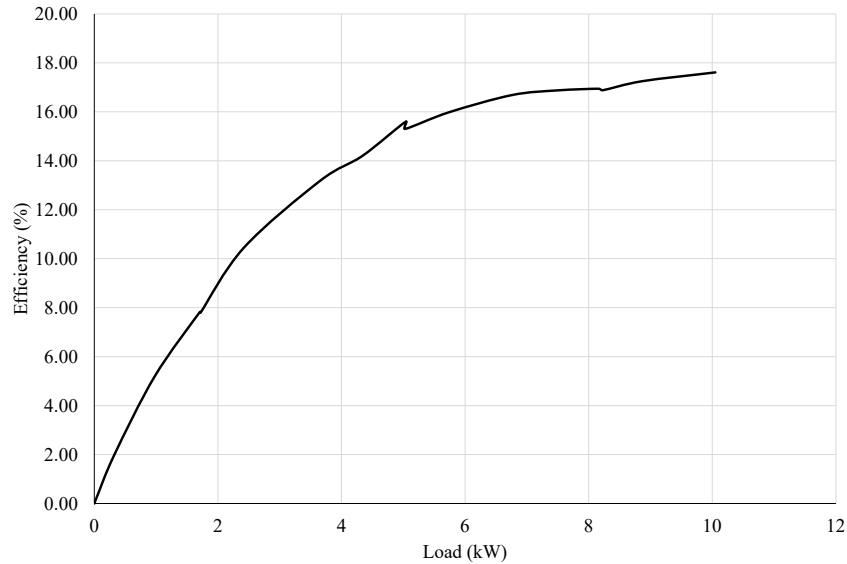


Figure 2.8. Plot of generator fuel efficiency versus load for 10.4 kW natural gas generator (Kohler 12RES).

A 10.4 kW Kohler 12RES, natural gas generator as shown in Figure. 2.9, was used in the microgrid system in this study.



Figure 2.9. Natural gas generator (Kohler 12RES).

2.3.2 PV systems

A system designed to supply solar power by using photovoltaics is a PV system. It comprises of an arrangement of several components, such as, PV or solar panels, solar inverter, mounts, cables and other electrical accessories to set up a working system. The

solar panels convert sunlight into direct current (DC) electricity and solar inverter converts DC into alternating current (AC) .

2.3.2.1 PV panels

PV module produces power when it is exposed to sunlight. PV cells are configured into PV modules and these modules are connected as arrays in PV systems. Figure 2.10 shows a simple PV system illustrating conversion of solar energy into electrical energy. When sunlight falls on the surface of the PV cell, it excites the electrons and causes them to jump from one energy level to another energy level, thereby leaving holes behind. These electrons and holes are the charge carriers. As free electrons are generated, they pass through an external circuit, giving rise to electric current.

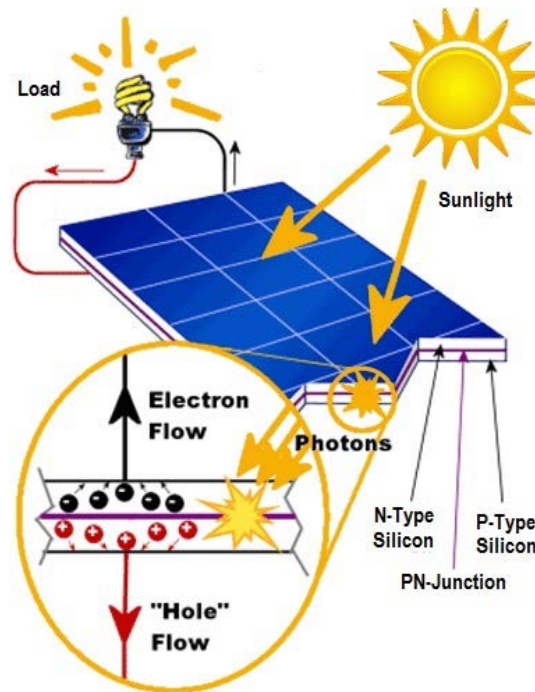


Figure 2.10. A simple PV system [59].

PV arrays produce power only when they are illuminated. So, PV systems are

generally use energy storage system such as battery to make the captured electrical energy available at a later time.

There are basically three approaches for using PV systems [60]:

- grid-connected utility-interactive PV system
 - straight grid-connected with no battery backup
 - grid-connected with battery backup
- standalone PV system

I-V characteristics of a typical solar cell is shown in Figure 2.11. Voltage and current from the cell depend upon the illumination level of the cell.

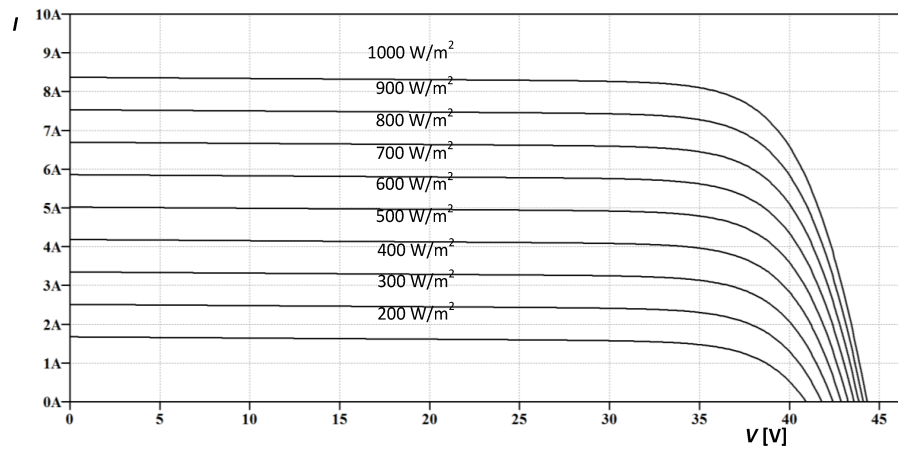


Figure 2.11. IV characteristics of PV cell under different illumination levels [61].

The power produced from the solar cell, P is given by

$$P = VI \quad (2.4)$$

where I is the cell current with voltage V .

The solar cell efficiency is defined as the ratio of energy output from the solar cell to energy input from the sun. The maximum solar cell efficiency, η_{max} is given by

$$\eta_{max} = \frac{\text{Maximum power output}}{\text{Solar irradiance } (G_t) \times \text{Area of the cell } (A)} \times 100\% \quad (2.5)$$

Solar irradiance is an instantaneous quantity which is the measure of the power density of sunlight. It is measured in W/m^2 . It is also known as intensity of sunlight. The manufacturers of solar cells use solar irradiance of $1000 W/m^2$ under Standard Test Conditions (STC) .

The output power of the PV array depends primarily on solar irradiance if the effect of temperature is neglected. The output power of the PV array, $P_{PV,t}$ at any time t is calculated from solar irradiance [62] as given in Equation 2.6.

$$P_{PV,t} = P_{Rated} f_{PV} \frac{G_t}{G_{t,STC}} \quad (2.6)$$

where P_{Rated} is the rated capacity of the PV array at STC in kW , f_{PV} is the PV system derating factor, G_t is the irradiance at t in W/m^2 and $G_{t,STC}$ is the irradiance at Standard Test Conditions (STC) in W/m^2 . Here the effect of temperature on the PV array is not considered. Figure 2.12 shows solar irradiance and the corresponding PV power output from $4.1 kW$ PV array in Brookings, South Dakota on January 1, 2012. Alternatively, the output power of the PV array can be calculated using Equation 2.7.

$$P_{PV,t} = \eta G_t A \quad (2.7)$$

where η is the efficiency of the PV array.

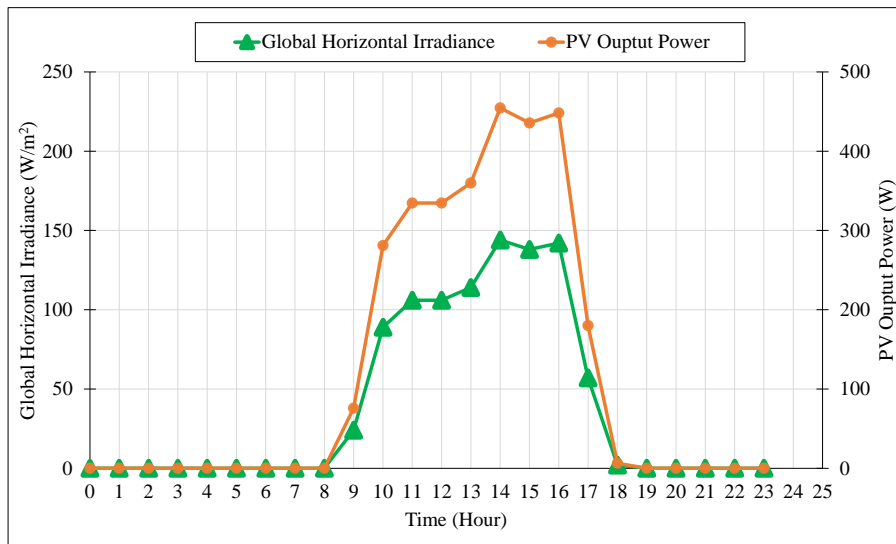


Figure 2.12. Solar irradiance and PV power output for January 1, 2012 for Brookings, South Dakota from 4.1 kW PV array.

Twenty Evergreen solar panels (ES-A-205-FA3) with rated power of 205 W each as shown in Figure 2.13, were used in the microgrid system in this study. The total installed capacity of the PV system was 4.1 kW. The specification of the solar panel is shown in Table 2.1.



Figure 2.13. Solar panels (Evergreen ES-A-205-FA3) on the rooftop of Daktronics Engineering Hall, SDSU.

Table 2.1. Evergreen solar panel specifications [63].

Specification	Parameters
Maximum power point or rated power	205 W
Minimum efficiency	13.04%
Voltage at maximum power	18.2 V
Current at maximum power	11.27 A
Open-circuit voltage	22.7 V
Short-circuit current	11.93 A

2.3.2.2 Solar or PV inverters

A solar inverter is a power electronic device which converts variable DC output of PV panels into AC. It is one of the important components of balance of system (BOS) in a PV system. PV systems are compatible in use with the PV panels, including features such as Maximum Power Point Tracking (MPPT) and anti-islanding feature. The MPPT is a technique to have maximum possible power from the PV panels.

SMA Sunny Boy as shown in Figure 2.14, model SB 5000US, a product of SMA America, was used as a PV inverter in the microgrid system in this study. This inverter is suitable for use with sources such as small wind turbine systems, fuel cells, and other DC current sources [64].



Figure 2.14. SMA Sunny Boy (SB-5000US) solar inverter.

2.3.3 Energy storage systems

Energy storage system delivers many services in microgrids such as load management, optimization of fuel consumption, voltage and frequency regulation, and optimization of renewable resources (PV, wind) [6]. Energy storage technologies, namely, batteries and flywheels are used in microgrids. Among battery, flow, lead-acid, lithium ion and Sodium Metal Halide (SMH) batteries are used in microgrids. Typically, flywheels do not support integration of renewable resources directly. However, they manage the frequency on the microgrid, including disruptions obtained from intermittent wind and PV.

Batteries enable dispatching of the generators in microgrids to meet the demand [7]. Battery can act as a source along with the generators or they can act as a load, ensuring full load operation of the generator. Moreover, batteries store electrical energy from PV, thereby increasing PV resource utilization. One of the important parameters for battery management is SOC. It is the remaining capacity of a battery. In other words, it is the amount of energy available in a battery. It is represented in percentage. It is affected by the battery operating conditions such as temperature and load current. Mathematically,

$$SOC = \frac{\text{Remaining Capacity}}{\text{Rated Capacity}} \times 100\% \quad (2.8)$$

SOC dynamics can be expressed as shown in Equation 2.9 and Equation 2.10 for charging and discharging conditions, respectively [65].

$$SOC(t + \Delta t) = SOC(t) + \frac{P_{batt}(t) \times \eta_{ch}}{C_{batt}} \quad (2.9)$$

$$SOC(t + \Delta t) = SOC(t) + \frac{P_{batt}(t)}{C_{batt} \times \eta_{disch}} \quad (2.10)$$

where $SOC(t)$ is the SOC at any time t , $SOC(t + \Delta t)$ is the SOC after time Δt , η_{ch} and η_{disch} are charging and discharging efficiencies of the battery, C_{batt} is the battery capacity in kWh , and $P_{batt}(t)$ is the battery power at the time t . Equation 2.9 and Equation 2.10 show how SOC after certain time Δt can be calculated. In these equations, positive sign for $P_{batt}(t)$ is used for charging condition and negative sign for $P_{batt}(t)$ is used for discharging condition. $P_{batt}(t)$ is maintained within maximum battery charging and discharging power, denoted by $P_{batt,max_ch}(t)$ and $P_{batt,max_disch}(t)$, respectively:

$$P_{batt,max_disch}(t) \leq P_{batt}(t) \leq P_{batt,max_ch}(t) \quad (2.11)$$

The battery lifetime degrades when it is operated in lower SOC for a long period of time. So, $SOC(t)$ is maintained maximum permissible limit SOC_{max} and minimum permissible limit SOC_{min} as shown below:

$$SOC_{min} \leq SOC(t) \leq SOC_{max} \quad (2.12)$$

The ESS used in the laboratory consisted 48 V, 8.2 kWh lithium-ion rechargeable batteries from International Battery company as shown in Figure 2.15. The cells are available in a rugged prismatic format. The lithium iron phosphate ($LiFePO_4$) cathode material that is used in the battery is intrinsically safe, and is environment-friendly. The battery offers superior quality with high efficiency, high discharge currents, low cell

impedance, longer cycle life, high energy density and low self discharge with wide operating temperature characteristics. These batteries find wide applications in energy storage for solar, wind and tidal applications. They are also used in smart grid, electric vehicles, telecommunications and military applications. The ESS also consists of Battery Management System (BMS) . The BMS manages the entire battery system as well as interfaces with the customer’s application through CAN (Controller Area Network) bus, RS-232/485 and ethernet. It maximizes the safety, performance and life of the battery systems. It has full diagnostic capability and measures voltage, current, temperature, SOC, State of Health (SOH) charge/discharge balancing, and isolation detection. The specification of the battery used in the microgrid system is shown in Table 2.2.



Figure 2.15. Lithium-ion rechargeable battery.

Table 2.2. Lithium iron phosphate battery specifications [66].

Specification	Parameters
Energy Capacity	8.2 kWh
Calendar life	more than 5 years
Nominal Voltage	51.2 V
Maximum Charge Voltage	57.6 V
Minimum Discharge Voltage	40 V
Maximum Continuous Discharge Current	160 A (1C)
System Operating Temperature during charging	0°C to 50°C
System Operating Temperature during discharging	-10°C to 55°C

2.3.4 Hybrid inverter/chargers

A hybrid inverter/charger is a combination of DC to AC inverter, battery charger and an AC auto-transfer switch. Generally, it is capable of being grid-interactive or grid independent. It can even operate with generators and renewable energy sources to provide full-time or backup power [67]. Xantrex hybrid inverter/charger, model XW6048-120/240-60, a product of Schneider Electric as shown in Figure 2.16, was used in the laboratory. It is sine wave inverter/charger which can be used for standalone, grid-backup and grid-tied applications with energy storage system (battery). The Xantrex inverter/charger uses Xanbus which is a network communication protocol, developed by Xantrex. Xanbus is similar to CAN bus and is used to communicate its settings and activity to other Xanbus enabled devices.



Figure 2.16. Xantrex hybrid inverter/charger (XW6048 120/240 60).

A hybrid inverter/charger and battery management system in microgrid system can be controlled through CAN protocol. Control commands can be sent using CAN bus as physical layer of communication. CAN, which transmits data in terms of sequences and packages, is an advanced differential two line serial communication network which supports real-time control [68]. CAN-based networks have been widely used in the automotive field and extended to other industrial environments [69]. CAN is now becoming a good candidate for providing a reliable and safe control and communication network for microgrid EMS.

Figure 2.17 shows a block diagram of the CAN physical layer. It illustrates that CAN has a controller, generally microcontroller that controls and manages the transmit and receive lines. The connection of these lines to the physical CAN bus is through a CAN transceiver which converts the values on the transmit and receive lines to the respective CANH (high) and CANL (low) signals. Transmission of data in CAN takes

place in the binary format with logical 0 and 1.

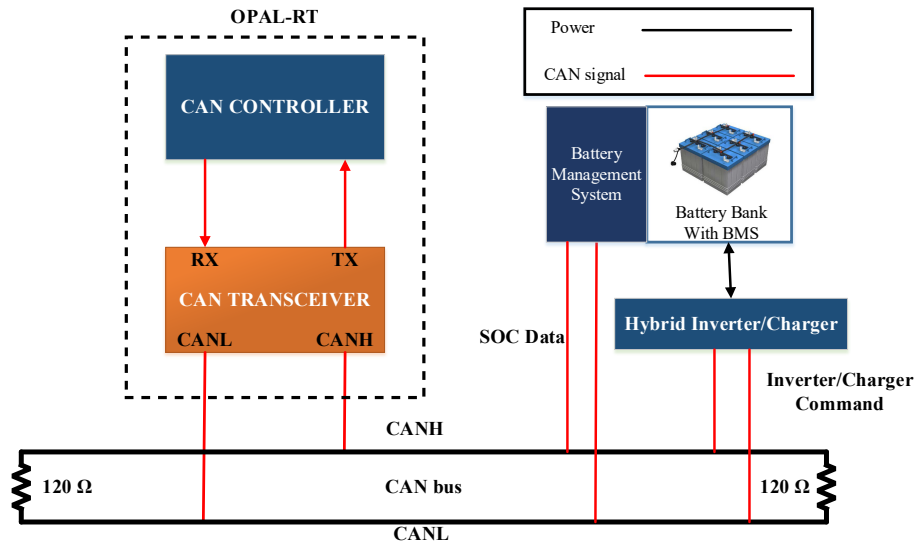


Figure 2.17. Block diagram of CAN.

2.3.5 Loads

An electrical load is a component that consumes electric power. The load used in the microgrid system in this study was Cannon L-63, which is also known as Automatic Load Bank (ALB) as shown in Figure 2.18. It is a portable load bank designed to be used for field servicing and testing generators and inverters. It is rated at 30 kW full loads with all 6 steps turned on. The load steps are 1 kW, 2 kW, 2 kW, 5 kW, 10 kW, and 10 kW.

This gives a 0 to 30 kW range in 1 kW steps which are all continuous. Load Profile Manager software was used for programming the ALB. A screenshot of the software is shown in Figure 2.19. With the use of Load Profile Manager, the load steps are 0.667 kW, 1.333 kW, 2 kW, 2.667 kW, 3.333 kW, 4 kW, 4.667 kW, 5.333 kW, 6 kW, 6.667 kW, 7.333 kW, 8 kW, 8.667 kW, 10 kW, 10.667 kW, 11.333 kW, 12 kW, 12.667 kW, 13.333 kW, 14 kW, 14.667 kW, 15.333 kW, 16 kW, 16.667 kW, 17.333 kW, 18 kW, 18.667 kW, 19.333 kW and 20 kW.



Figure 2.18. Automatic Load Bank (Cannon L-63).

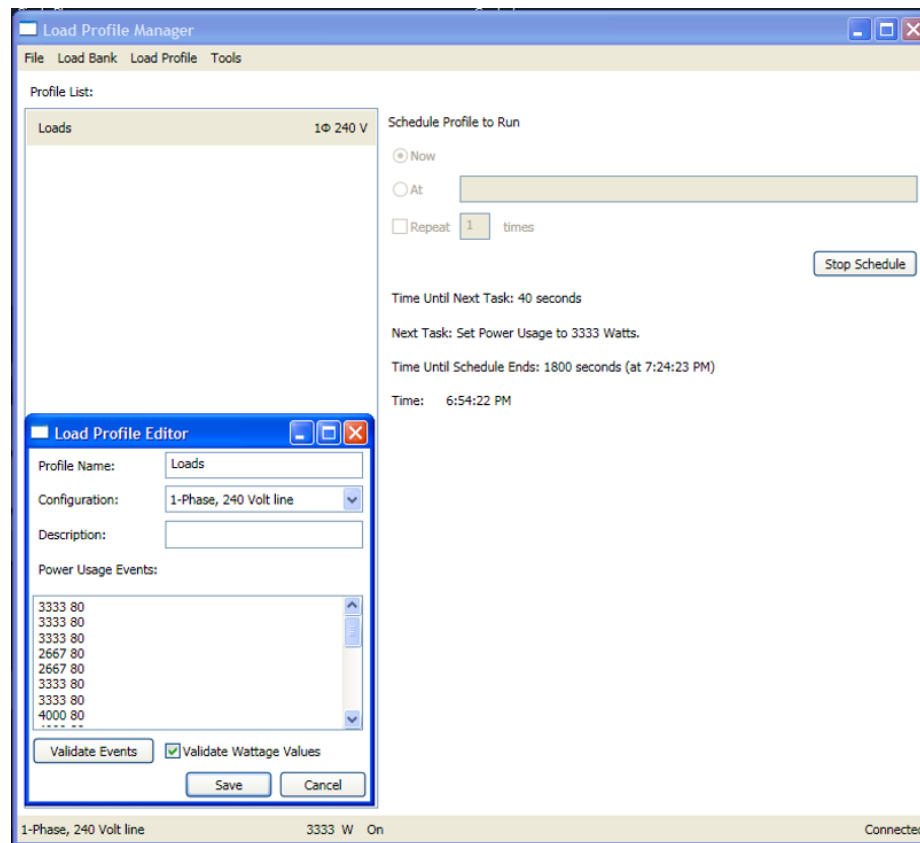


Figure 2.19. Screenshot of load profile manager software.

2.4 Scheduling and optimization

The process of allocation of energy resources ahead of time in order to achieve the desired objective is known as scheduling. It is carried out for the economic operation of

the microgrid. Reference [70] presents two-stage scheduling: day-ahead and real-time scheduling. The day-ahead scheduling determines hourly power settings of DERs and the real-time scheduling updates those settings of the resources, taking into consideration the results of the day-ahead scheduling and signals from the real-time operation of the microgrid.

The scheduling provides economical operation based on the optimization method. It determines the optimal control sequence including the state of the operation and the power of the controllable units [71]. The scheduling requires forecasting of uncertain quantities such as PV output power, loads, etc. For instance, a day-ahead schedule step considers PV irradiance forecasts, load demand, system architecture information and constraints on the system. Generally, these information are utilized for scheduling operation of gensets and energy storage systems such as batteries in the microgrid so as to reduce the fuel consumption [72].

The scheduling method incorporates optimization. The variables in this optimization are energy resources output power and operating states (ON/OFF) of the energy resources. The constraints can be equality and inequality types.

The scheduling is basically carried out in two approaches or methods:

- Deterministic methods
- Stochastic methods

Each of these methods are explained in the following sections:

2.4.1 Deterministic methods

The deterministic approach of scheduling makes an assumption that the problem entries, other than the problem variables, are known fixed data. For example, the assumption may be that the actual values of stochastic quantities such as PV output power and loads are equal to the forecasted values. However, in the real-world problems, the assumption is not true, as many of the parameters correspond to inexact measurements or statistical estimations. Hence, the EMS must address the variability and uncertainty in the stochastic quantities. It can be done by scheduling spinning reserve, which is the unloaded generation that is synchronized and ready to serve the additional demand.

There is high penetration of non-dispatchable energy resources in the remote microgrids. Hence, the spinning reserve is used in these microgrids so as to address the variability and uncertainty. The major causes of the uncertainty may be load and renewable energy resources' uncertainty or equipment failure. Traditionally, deterministic rules are used [73] for the determination of the required spinning reserve. It is set in accordance to the capacity of the largest running unit or a fraction of the load or their combination. However, this method does not consider the stochastic behavior of the system and component failures and the economics. The another approach for the determination of the spinning reserve is probabilistic. In this method, statistical measures such as standard deviation, confidence interval, etc. are used to determine the spinning reserve [74].

2.4.2 Stochastic methods

The deterministic approach is considered as a special case of the stochastic approach with only one scenario corresponding to the point forecast [75]. The deterministic approach ignores the variability in the PV output power in the optimization. This may result in the improper utilization of the energy resources. The accurate forecast of the PV output power cannot be available during day-ahead scheduling stage. Hence, the decisions taken in this stage must have flexibility to incorporate the variability and uncertainty. The stochastic approach of scheduling can be used for the improvement of the system performance. This method incorporates the uncertainties by developing scenarios, which have higher probability of occurrence in the future and minimizing the expected value of the objective function over all the considered scenarios. A set of all the possible future alternatives is known as scenario. Scenario generation is critical to capture the variation in the system, in the sense that the unrealistic scenarios may make the system less reliable and thus, the optimization benefits may be compromised. In summary, in the stochastic approach, rather than minimizing the objective function, $f(x)$ for a single scenario, this approach tries to minimize the expected value, $E(f(x))$ over all the considered scenarios.

2.5 Solar irradiance

Solar irradiance is an instantaneous quantity which is the measure of the power density of sunlight. It is measured in W/m^2 . It is also known as intensity of sunlight. There are three major components of sunlight: direct or beam radiation, diffuse radiation and albedo radiation [60].

- i) Direct or beam radiation: Sunlight that reaches the surface of the earth without

scattering is known as direct or beam radiation.

- ii) Diffuse radiation: Scattered sunlight is known as diffuse radiation.
- iii) Albedo radiation: Sunlight that is reflected from the ground is known as albedo radiation.

The sum of all these three components is known as global radiation. The total irradiance incident on a horizontal plane at the surface of the earth is known as Global Horizontal Irradiance (GHI). The forecasting of GHI is the first and most essential step in most of the PV power prediction systems [11].

2.5.1 Clear Sky Irradiance

CSI is the irradiance under a cloudless sky and can be expressed as the intensity of the direct sunlight. It is defined as a function of the Air Mass (AM) using the following experimentally-based equation [76]:

$$CSI = 1367(0.7)^{AM^{0.678}} W/m^2 \quad (2.13)$$

where 0.678 and 0.7 are empirical numerical constants and AM is air mass, which is the length of path that the solar radiation covers to travel to the surface of the earth and it is a function of the time of year, the time of day and the latitude.

2.6 Some of the terminologies used in forecasting irradiance

This section provides a brief description of the terminologies used in forecasting irradiance.

2.6.1 Latitude (ϕ)

It is the angular location north or south of the equator. The north side is taken as positive. It is denoted by ϕ . It varies between -90° to $+90^\circ$.

2.6.2 Declination angle (δ)

It is the angle between the equator and a line drawn from the center of the earth to the center of the sun [77] as shown in Figure 2.20. It depends upon the revolution of earth and remains constant for a day. It is denoted by δ and is calculated as shown below:

$$\delta = 23.45 \sin \left[\frac{360}{365} (284 + d) \right] \quad (2.14)$$

Also,

$$\delta = 23.45 \sin \left[\frac{360}{365} (d - 81) \right] \quad (2.15)$$

where, d is the day of the year with January 1 as $d = 1$.

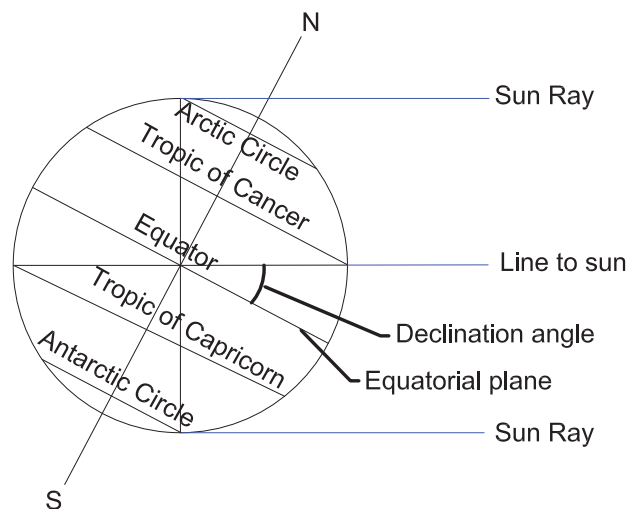


Figure 2.20. Declination angle.

2.6.3 Hour angle (ω)

It is the angular displacement of the sun in the plane of its apparent rotation from the solar noon. It is expressed as difference between noon and the desired time of day in terms of a 360° rotation in 24 hours [60]. It is denoted by ω and is shown in Figure 2.21.

Mathematically,

$$\omega = \frac{12 - T}{24} \times 360^\circ \quad (2.16)$$

where T is the time of day with reference to solar midnight, on a 24 hours clock.

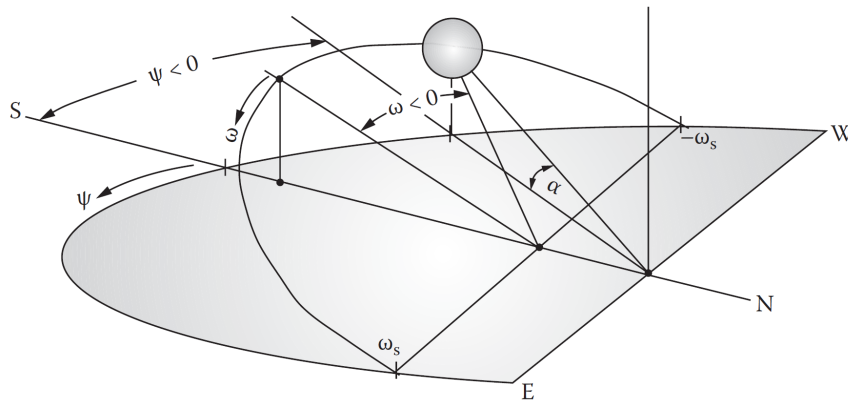


Figure 2.21. Hour angle, along with altitude and azimuth angles [60].

Similarly, the sunrise angle (ω_s) is given by [60]

$$\omega_s = \arccos(-\tan \phi \tan \delta) \quad (2.17)$$

The sunset angle is denoted by $-\omega_s$. The sunrise and sunset angles are used to determine the total number of daylight hours on a particular day at a specific latitude.

The hours corresponding to sunrise and sunset angles are known as sunrise hour (SRH) and sunset hour (SSH), respectively. These hours are calculated using

Equation 2.18 and Equation 2.19, respectively.

$$SRH = T_N - \frac{DH}{2} \quad (2.18)$$

$$SSH = T_N + \frac{DH}{2} \quad (2.19)$$

Here, T_N is the solar noon time for the location for which solar irradiance has to be forecasted and it is given by Equation 2.21 and DH is the daylight hours, i.e. hours for which the sun will be available throughout a day. DH [60] is computed using

$$DH = \frac{\omega_s}{7.5} \quad (2.20)$$

Figure 2.22 shows time for which sunlight is available throughout a year for Brookings, SD. It shows that during the winter i.e. at the beginning and end of the year, the daylight hours are less. During the summer, the daylight hours are more.

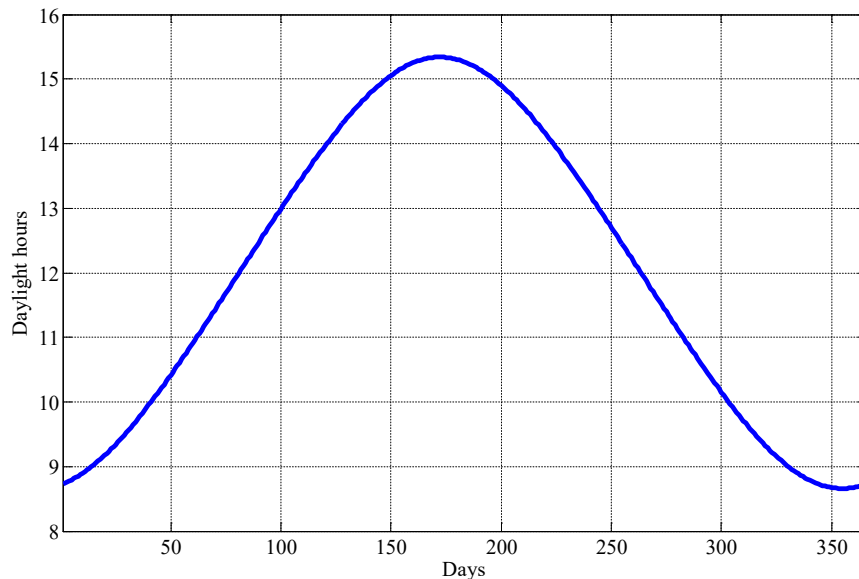


Figure 2.22. Daylight hour throughout a year.

Various time standards are defined for various longitudes. The solar noon occurs at clock noon at multiples of 15° east or west longitude. To find the solar noon at the intermediate longitudes, interpolation can be used. The solar noon time can be determined by using

$$T_N = 12 + \frac{L_{location} - L_{standard}}{15} \times 60 \quad (2.21)$$

where, $L_{location}$ and $L_{standard}$ are the longitudes of the location and standard location, respectively.

SRH and *SSH*, together provide the idea of the time span for which CSI has to be calculated for a day.

2.6.4 Zenith angle (θ_z)

It is the angle between the vertical and the line to the sun [78]. In other words, it is the angle of incidence of direct radiation on a horizontal surface. It is denoted by θ_z and is given by

$$\cos \theta_z = \sin \delta \sin \phi + \cos \delta \cos \phi \cos \omega \quad (2.22)$$

2.6.5 Solar altitude or elevation angle (α)

It is the angle between the horizontal and the line to the sun [78]. It is the complement of the zenith angle as shown in Equation 2.23. It is 0° at sunrise and sunset and 90° when the sun is directly overhead. It varies throughout the day and depends upon the latitude of a particular location and the day of the year. It is denoted by α and is given by

$$\alpha = 90^\circ - \theta_z \quad (2.23)$$

2.6.6 Solar azimuth angle (ψ)

It is the angle which measures the sun's angular position east or west of south [60]. It is 0° at solar noon and increases toward the east. Some authors define this angle with reference to north rather than south. It is denoted by ψ . Figure 2.23 shows zenith, altitude and azimuth angles for northern latitude.

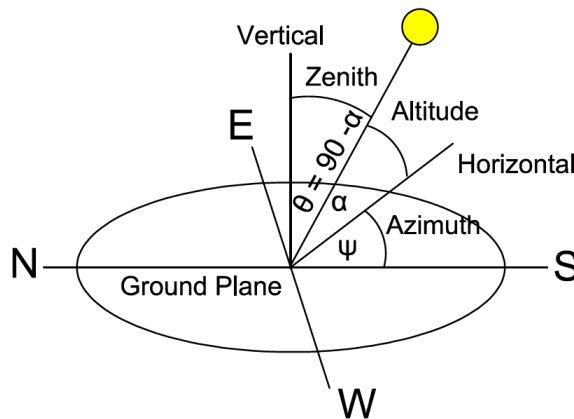


Figure 2.23. Zenith, altitude and azimuth angles for northern latitude.

2.6.7 Air Mass (AM)

It is the path length that the solar radiation covers to travel to the surface of the earth. It is a function of the latitude, the time of year and the time of day. It is computed as the secant of the zenith angle [60] and is given by

$$AM = \sec \theta_z \quad (2.24)$$

2.7 Fourier basis expansion

Fourier basis functions are used for the representation of periodic variation in the observed data. In this thesis, the functions are used to explain the periodic characteristics

of solar irradiance. The Fourier series [79] is given by

$$\hat{x}(t) = \sum_{m=0}^n \beta_m \phi_m(t) \quad (2.25)$$

That is,

$$\hat{x}(t) = \beta_0 + \beta_1 \sin \omega t + \beta_2 \cos \omega t + \beta_3 \sin 2\omega t + \beta_4 \cos 2\omega t + \beta_5 \sin 3\omega t + \beta_6 \cos 3\omega t \dots \quad (2.26)$$

where $\phi_m(t)$ represents basis defined by $\phi_0(t) = 1$, $\phi_{2r-1}(t) = \sin(r\omega t)$ and $\phi_{2r}(t) = \cos(r\omega t)$.

The basis is periodic and the parameter ω defines the time period as $T = \frac{2\pi}{\omega}$. There are two variations in solar irradiance: daily and yearly variation. Solar irradiance is high during midday and low in the evening. This daily variation is represented using nine Fourier basis terms. The value of the coefficients are determined using model fitting. Similarly, the yearly variation of solar irradiance is represented by seven Fourier basis terms.

2.8 Markov switching model (MSM)

The MSM, also known as the regime switching model, is one of the most popular time series models. It considers multiple structures (or equations) that can characterize the time series behaviors in various states or regimes. The model is used to capture complex dynamic patterns by allowing switching between the structures [80]. The switching mechanism in the MSM is controlled by an unobservable state variable, also known as a latent variable that follows a first-order Markov chain. The first-order Markov chain

implies that the current value of the state variable depends on its immediate past value. A structure may persist for a random period of time. It will be substituted by another structure when a switching occurs. Fig. 2.24 shows a flowchart of the development of the MSM.

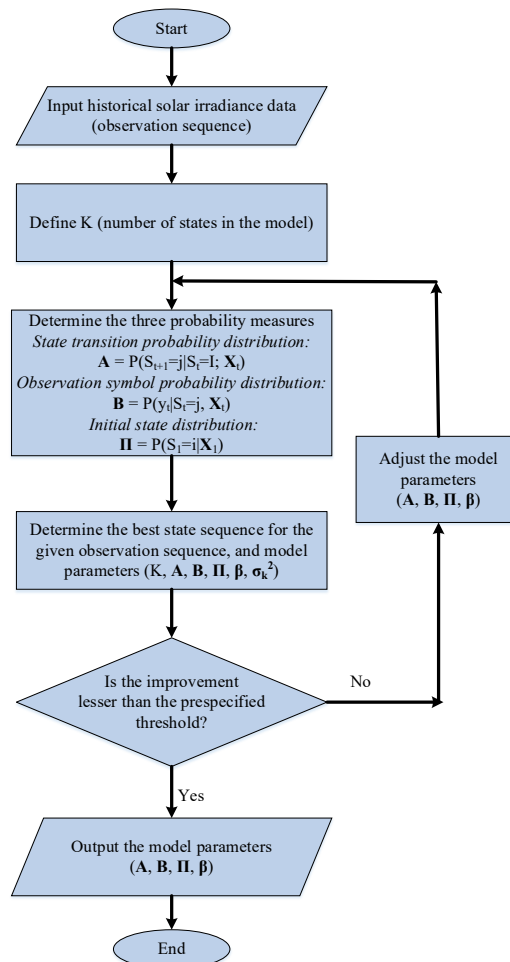


Figure 2.24. Flowchart of MSM.

Let $\mathbf{y} = y_1, \dots, y_T$ be observations from univariate time series of length T and let $\mathbf{X} = \mathbf{X}_1, \dots, \mathbf{X}_T$ denote the matrix of covariates. Then, based on the MSM model, at any time point, the observations are distributed according to a mixture model with K components (hidden states) $\mathbf{S} = (S_1, \dots, S_T)$ where, $S_t \in \{1, \dots, K\}$ for $t = 1, \dots, T$. The

joint likelihood for y_1, \dots, y_T and the hidden states S_1, \dots, S_T , given the covariates \mathbf{X} and the vector of parameters $\boldsymbol{\theta}$ is given as

$$L(\mathbf{Y}, \mathbf{S} | \mathbf{X}, \boldsymbol{\theta}) = P(S_1 = i | \mathbf{X}_1) f_{S_1}(y_1 | \mathbf{X}_1) \prod_{t=2}^T p_{ij}(\mathbf{X}_t) f_{S_t}(y_t | \mathbf{X}_t) \quad (2.27)$$

where $f_{S_t}(y_t | \mathbf{X}_t)$ describes a vector of conditional densities $\mathbf{B} = P(y_t | S_t = j, \mathbf{X}_t)$ for

$j = 1, \dots, K$. A matrix \mathbf{A} is constructed from the transition probabilities

$p_{ij}(\mathbf{X}_t) = P(S_{t+1} = j | S_t = i; \mathbf{X}_t)$, representing the transition probability from state i to

state j given covariate \mathbf{X}_t . The parameters are estimated through maximum likelihood

approach. This is done either through the Expectation-Maximization (EM) algorithm [81]

or numerical optimization of the corresponding log-likelihood using methods such as the

Newton-Raphson. The EM algorithm is a maximum likelihood estimation technique that

consists of two steps, namely, E-step and M-step. In the E-step, the sequence of states are

estimated based on the model basis set and model parameters set. The M-step performs

maximization of the complete-data likelihood resulting in adjusted model parameters.

E-step and M-step are iterated until the given convergence criterion is met. Specifically, in

the E-step, the best sequence of the states S_t for $t = 1, \dots, T$ is estimated using

forward-backward algorithm. This needs estimated parameters from the previous step of

the iteration. At the M-step, the expected complete-data log likelihood function is then

maximized with respect to the parameters given \mathbf{y} , \mathbf{X} and estimated state sequence, \hat{S}_t .

These two steps are iterated until a prespecified convergence criterion is met.

In this thesis, MSM is used to model the nonlinear pattern of solar irradiance. The irradiance at time t is considered to have a latent state. The latent state variable affects the

value of the solar irradiance at time t . The matrix of covariates (\mathbf{X}) consists of CSI, yearly Fourier component $\phi_{1i}, i = 1, \dots, p$ and daily Fourier component $\phi_{2j}, j = 1, \dots, q$. The model is written as

$$y_t(S_t = k) = \beta_0 + \beta_{k,1}CSI(t) + \sum_{i=1}^p \beta_{k,1i}\phi_{1i}(t) + \sum_{j=1}^q \beta_{k,2j}\phi_{2j}(t) + \varepsilon_k(t) \quad (2.28)$$

where $CSI(t)$ is the clear sky irradiance at time t with the corresponding coefficient $\beta_{k,1}$ and β_0 is the intercept of the model. $\beta_{k,1i}$ represents the coefficient corresponding to the i^{th} component of the Fourier basis function for yearly variation in solar irradiance at state k . Similarly, $\beta_{k,2j}$ represents the coefficient corresponding to the j^{th} component of the Fourier basis function for daily variation in solar irradiance at state k . The length of Fourier basis expansions for yearly and daily irradiance are p and q , respectively. $\varepsilon_k(t)$ is a random noise component and is commonly assumed to be a normally distributed random variable with zero mean and constant variance σ_k^2 .

Probability transition matrix is another part of the MSM that needs to be estimated. It gives the probability of movement between the regimes as illustrated in Figure 2.25. A system with K regimes will have a probability transition matrix of order $K \times K$, where a number of rows represents the current or “from” state and columns represent the final or “to” state. Probabilities close to one in the diagonal represent stable states.

The probability transition matrix of 3×3 order is shown below:

$$\mathbf{A} = \begin{bmatrix} p_{11} & p_{12} & p_{13} \\ p_{21} & p_{22} & p_{23} \\ p_{31} & p_{32} & p_{33} \end{bmatrix}$$

The calculation of the elements of the probability transition matrix is done through maximum likelihood estimation using

$$p_{ij} = \frac{\text{Count}(S_{t-1} = i \text{ and } S_t = j)}{\text{Count}(S_{t-1} = i)} \quad (2.29)$$

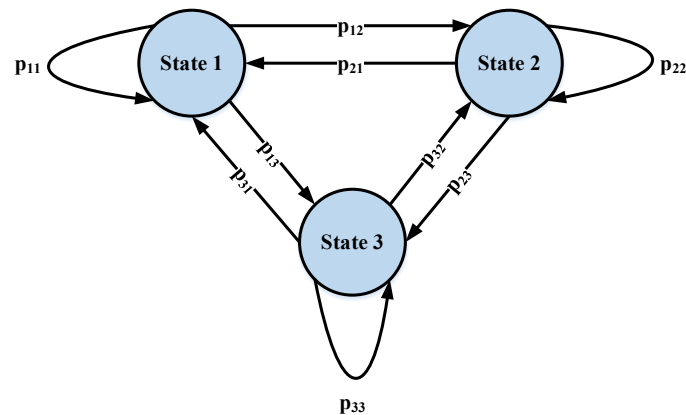


Figure 2.25. Probability transition for a model with 3 states.

The estimated sequence of states obtained from the EM algorithm is used in the computation of (2.29) as the truth is unknown. The Fourier basis expansions and CSI values are used as covariates; and the coefficients and the probability transition matrix are estimated. The fitting of this model is done using the statistical *R* package, *MSwM*[82].

This results in $\hat{y}_t(S_t = k)$, the estimated solar irradiance at time $t = 1, \dots, T$ for state

$k = 1, \dots, K$. For forecasting solar irradiance, firstly estimated parameters are used to find the predicted irradiance for each state. Then the best sequence is selected by looking at the first few hours of the day. The details of the forecasting procedure is given in Chapter 4.

2.9 Bayesian Information Criterion (BIC)

BIC [83], also known as Schwarz Information Criterion (SIC), is an index used to select the best model among the models being considered. Equation (3.1) is used for computing BIC for the model with K states (M_K).

$$BIC_K = -2\log L(\mathbf{y}|\hat{\theta}, M_K) + d_K \log N \quad (2.30)$$

where $\log L(\mathbf{y}|\hat{\theta}, M_k)$ indicates the log likelihood value of the model at parameter estimate $\hat{\theta}$, N is the sample size and d_K is the number of parameters.

This information criterion takes into consideration the number of parameters and goodness of fit of the models. The criterion penalizes the number of parameters required for the model's goodness of fit. Between the given models, the model with the smallest BIC value is chosen for the best fit with fewer parameters.

2.10 Standard error metrics for measuring overall performance of forecasting

Two standard error metrics that are used for the calculation of forecasting errors include Root Mean Square Error (RMSE) and Mean Absolute Percentage Error (MAPE). RMSE is the square root of the sum of the squares of the difference between hourly forecasted irradiance and hourly actual irradiance over a period of a year. RMSE measures a model's overall performance, especially where the extreme events are a concern. It gives

the measure of the largest error or deviation. MAPE is the sum of the absolute values of the differences between hourly forecasted irradiance and hourly actual irradiance over the period of a year divided by the actual irradiance values. MAPE is also a measure of overall performance and is expressed in percentage. RMSE and MAPE are mathematically expressed as shown in (2.31) and (2.32), respectively.

$$RMSE = \sqrt{\frac{1}{T} \sum_{t=1}^T e_t^2} \quad (2.31)$$

$$MAPE = \frac{1}{T} \sum_{t=1}^T \left| \frac{e_t}{y_t} \right| \times 100 \% \quad (2.32)$$

where $e_t = y_t - \hat{y}_t$ with y_t and \hat{y}_t representing the actual and forecasted irradiance, respectively at time t . Here, T is the number of hours in a day or in a year.

2.11 EMS Algorithm

The EMS comprises double layers [71]: day ahead schedule and real-time dispatch layers as shown in Figure. 2.26, which schedules and controls the operation of the generators and batteries. The schedule layer determines economic microgrid operation scheme including state and power of the controllable units, on the basis of forecasting data, system architecture information and operational constraints whereas the dispatch layer uses the scheduled resources and dispatches them in real-time. It compensates the deviations between the actual load and solar data with the forecasted ones using batteries and generators. The dispatch layer also considers batteries and generators' parameters.

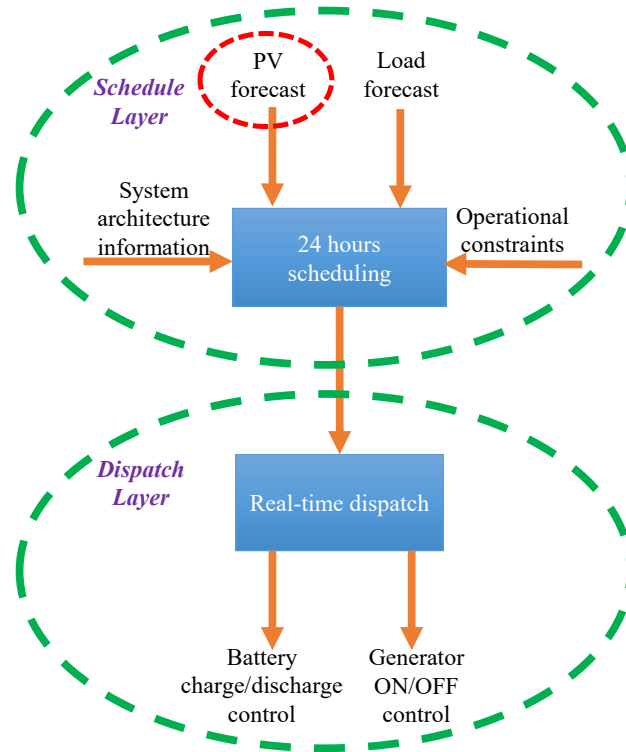


Figure 2.26. EMS with schedule and dispatch layers [84].

CHAPTER 3 PROCEDURES

Chapter 3 presents the procedures that were followed to achieve the objectives of this thesis. The procedures for forecasting solar irradiance using MSM and its real-time implementation in OPAL-RT real-time digital simulator are presented in this chapter, followed by the procedures for carrying out scheduling and optimization of the resources of the microgrid. The steps for developing models in MATLAB/Simulink, integrated with RT-LAB Professional (a real-time digital simulation software), are also shown.

3.1 Solar irradiance forecasting using MSM

For forecasting solar irradiance using MSM, three components are used: CSI, Fourier basis functions, and historical solar irradiance data. Fig. 3.1 shows the block diagram for the solar irradiance forecasting using this model.

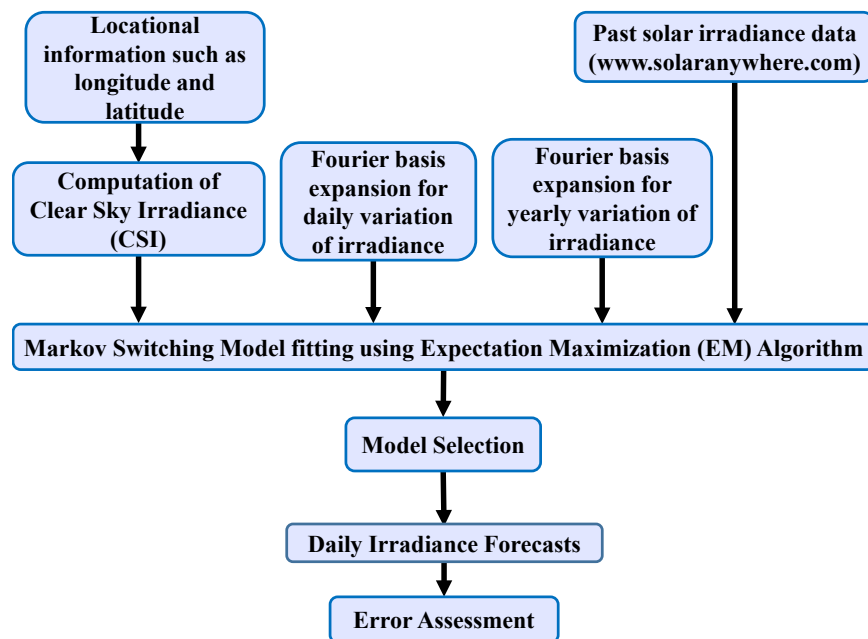


Figure 3.1. Block diagram for solar irradiance forecasting using MSM.

3.1.1 Dataset

Solar radiation data for the past 15 years were obtained from SolarAnywhere [85], a web-based service that offers hourly Global Horizontal Irradiance (GHI), Direct Normal Irradiance (DNI), and Diffuse Horizontal Irradiance (DHI) for various locations within the USA and which dates from 1998 to 2013. The website considers ground based solar resource data as well as satellite based solar resource data and reduces uncertainty in solar resource assessment [86]. The ground-measured data is collected using ground stations, and then the solar resource is evaluated via long term satellite-based irradiance measurement. The area resolution of the solar irradiance data was 100 km^2 and the time resolution was 1 hour. Only GHI was used for data analysis.

The case study was considered for Brookings, SD which has a latitude of 44.3° N and longitude of 96.8° W . Fig. 3.2 shows variation in solar irradiance from 2001 to 2011. The solar irradiance for these ten years illustrate the periodic variation in solar irradiance in the yearly data. Thus, the Fourier basis expansion was used to capture the yearly periodic variation in solar irradiance.

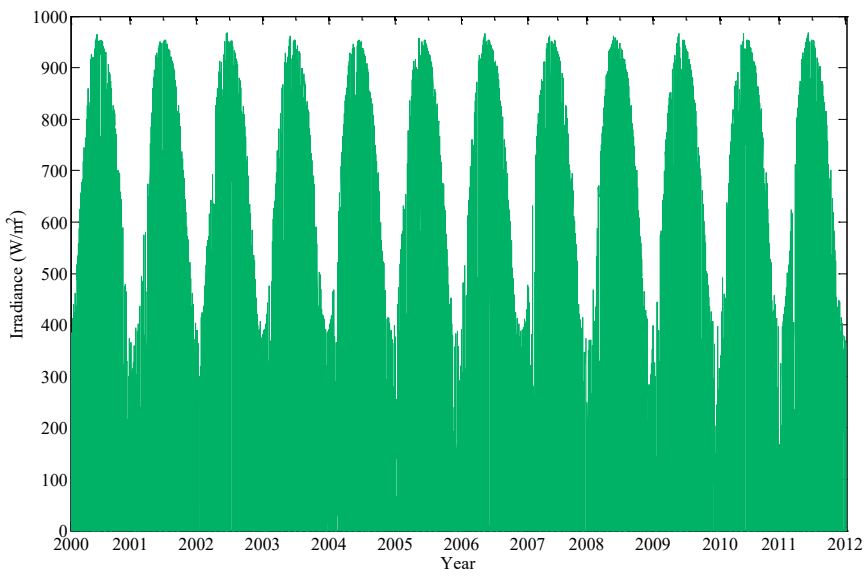


Figure 3.2. Solar irradiance for years from 2001 to 2012.

Fig. 3.3 illustrates the variation in solar irradiance for the year 2001. The daily peaks are high during the summer season and low during the winter season.

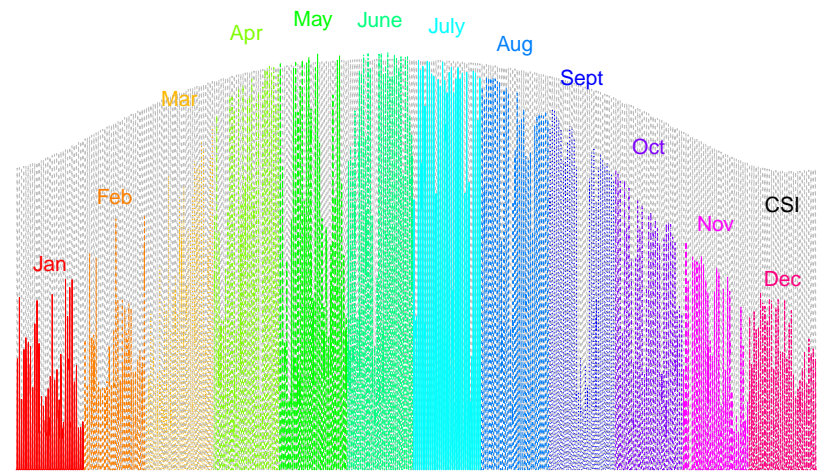


Figure 3.3. CSI for a year along with actual irradiance for the year 2001.

Taking a closer look, Fig. 3.4 depicts the variation in solar irradiance from January 1 to January 5 in the year 2001. It can be observed that the variation in solar irradiance is periodic in nature which implies that solar irradiance is a maximum during the day, a

minimum during the morning and evening, and zero at night. Thus, Fourier basis expansion can be used to capture this periodic nature of irradiance.

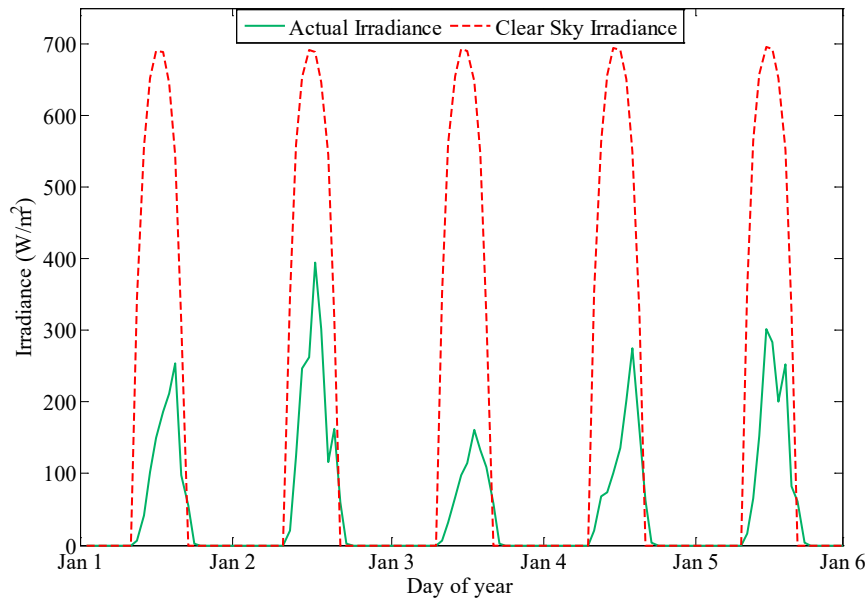


Figure 3.4. CSI and actual solar irradiance from January 1 through January 5, 2001.

Only hourly solar irradiance was considered for forecasting purpose although there may exist intra-hour variations in the irradiance data. In a microgrid system, the intra-hour variations can be handled by using reserves. The hourly irradiance forecasts are used in the scheduling stage of the EMS in the microgrid system. The deviations in the forecasted and actual irradiance in real-time is compensated in the dispatching stage using batteries and gensets [87].

3.1.2 Calculation of clear sky irradiance

For solar irradiance forecasting, the clear sky irradiance for the whole year for which irradiance has to be forecasted, was calculated using Equation (2.13). Fig. 3.3 shows the CSI for the year 2001 in the background. As expected, the CSI is greater than the observed solar irradiance. However, the same seasonal variation is observed in CSI as

the actual solar irradiance.

Figure 3.4 illustrates the variation of calculated CSI for the days from January 1 through January 5, 2001. It can be observed that CSI is zero at the beginning of the day and increases with maximum value during day time and then decreases during evening time thereby showing daily variation of the irradiance. The cycle repeats for the other days. CSI is similar for all the years except for leap years which have one extra day. The figure also shows the variation of actual solar irradiance from January 1 through January 5. The difference between the actual solar irradiance and the CSI exists as the CSI does not consider various components such as clouds, humidity, pollution etc. which have major role in the absorption of the solar irradiance.

3.1.3 MSM fit and forecasting

For fitting and testing the models, a free software environment for statistical computation and graphics, *R* version 3.1.3 was used on a computer with 64-bit Windows 7 operating system with 8 GB RAM and Intel(R) Core(TM)2 Quad CPU at 2.83 GHz. GHI data from years 2000 to 2002 were considered. Eight models with $K = 2$ and $K = 3$ were fitted and tested. Table 3.1 compares the models using BIC scores. The model that minimizes BIC score was selected. The model with $K = 3$ states, varying daily and yearly Fourier coefficients was found to have the lowest BIC score of 145,037. Thus, this model was selected. The three states were named as high, medium and low energy state corresponding to sunny, mildly cloudy and extremely cloudy days, respectively.

Table 3.1. BIC scores for fitted models

Yearly Fourier Coefficients	Daily Fourier Coefficients	K=2	K=3
Constant	Constant	157869	153992
Constant	Varying	155663	149715
Varying	Constant	157464	153294
Varying	Varying	151878	145037

The probability transition matrix for this model was calculated to be:

$$\begin{bmatrix} 0.854 & 0.115 & 0.000 \\ 0.146 & 0.735 & 0.105 \\ 0.000 & 0.120 & 0.895 \end{bmatrix}$$

In the calculated matrix, the diagonal elements are closer to 1 indicating that the states are stable. The matrix shows that the probability of solar irradiance remaining in the high energy regime is 0.854, which is higher than the probability of transitioning from the high energy regime to both the medium and low energy regimes. In fact, the diagonal elements are higher than the off-diagonal elements, indicating that irradiance is highly likely to maintain regime for the next hour. For example, if the morning irradiance is high, then it is predicted to remain high for the rest of the day.

Forecasting of solar irradiance was done by comparing the first four hours of actual irradiance data in the morning with each of the three energy states. The least square error method was used for this purpose. The regime with the least sum of squares of errors would be the forecasted irradiance for the rest of the day. However, for the first four hours of forecasting, the energy state on the previous day was used. For example, if the previous

day's solar irradiance forecasting state was in the high energy regime, then the first four hours irradiance on the next day was predicted to remain in the high energy regime.

The forecasted irradiance were validated with the past irradiance data and the error metrics such as, RMSE and MAPE were calculated. The forecasted PV system power output was then calculated by using Equation 2.6. The derating factor was chosen to be 0.77. The calculated PV power would be used in the EMS of the remote microgrid.

3.2 Real-time implementation of solar irradiance forecasting using MSM

Solar irradiance forecasting using MSM was implemented in a single-phase laboratory-scale microgrid system at Microgrid Research Laboratory in South Dakota State University, Brookings, SD. Real-time simulation platform, known as Real-Time Laboratory (RT-LAB), developed by OPAL-RT Technologies was used.

3.2.1 Photovoltaic panels as irradiance sensors

The power incident on the PV panel depends upon the power contained in the sunlight and the angle between the PV panel and the horizontal plane. The power density on the panel is maximum, when it is perpendicular to the sun. However, as the angle between the sun and the fixed surface changes continually, the power density on the surface is less than that of the sunlight.

The amount of solar radiation on the surface of the tilted panel ($S_{incident}$) is the component of the incident solar radiation. The incident solar radiation is perpendicular to the panel surface (S_{module}) [88].

From the geometry of Figure. 3.5, it can be stated that

$$S_{horizontal} = S_{incident} \sin \alpha \quad (3.1)$$

$$S_{module} = S_{incident} \sin(\alpha + \beta) \quad (3.2)$$

where α is the elevation angle and β is the tilt angle of the panel measured with respect to the horizontal plane.

Using Equation 3.1 and Equation 3.2, Equation 3.3 can be obtained as

$$S_{horizontal} = S_{module} \times \frac{\sin \alpha}{\sin(\alpha + \beta)} \quad (3.3)$$

The above approach is applicable for direct components only [89]. However, it is often used for applications such as system sizing to convert the direct component of mean daily solar irradiance on a horizontal surface for tilted solar panels with some acceptable error.

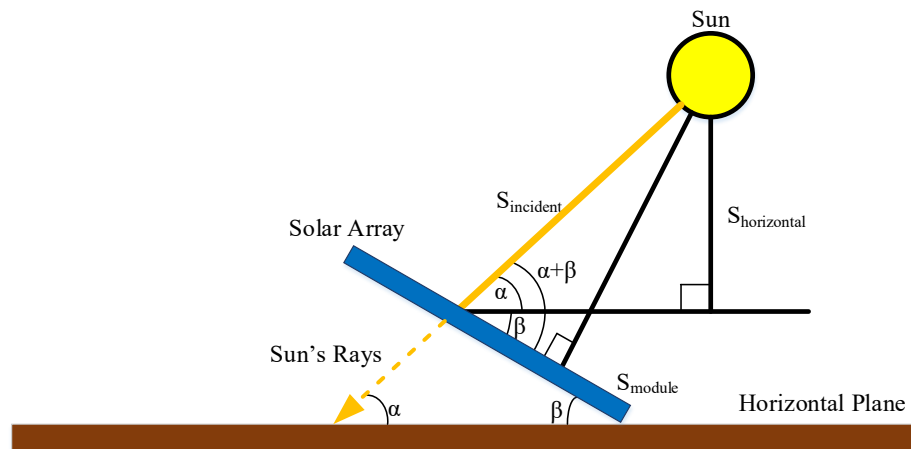


Figure 3.5. Illustration of solar irradiance incident on a tilted surface ($S_{incident}$), solar irradiance incident on horizontal surface ($S_{horizontal}$) and solar irradiance measured perpendicular to the module surface (S_{module}) [88].

3.2.2 Real-time irradiance measurement using OPAL-RT

Generally, pyranometers are used for the measurement of solar irradiance. But in this study, solar panels, themselves were used for measuring solar irradiance. The solar panels are connected to PV inverters which convert dc into ac. The power output from the inverters were calculated by using AC output voltage and AC output current. The area of the solar panels is known. Dividing the ac power output obtained from ac output voltage and ac output current, irradiance was calculated. This value of irradiance is the global tilted irradiance (GTI) as the solar panels are tilted at a certain angle. This value was converted into its corresponding global horizontal irradiance (GHI) using the analysis shown in the previous section. The first four hours irradiance data in the morning was then used from the calculated GHI and they were then used for forecasting irradiance for the rest of the day. Figure. 3.6 shows the block diagram of the implementation of solar irradiance forecasting in OPAL-RT real-time digital simulator.

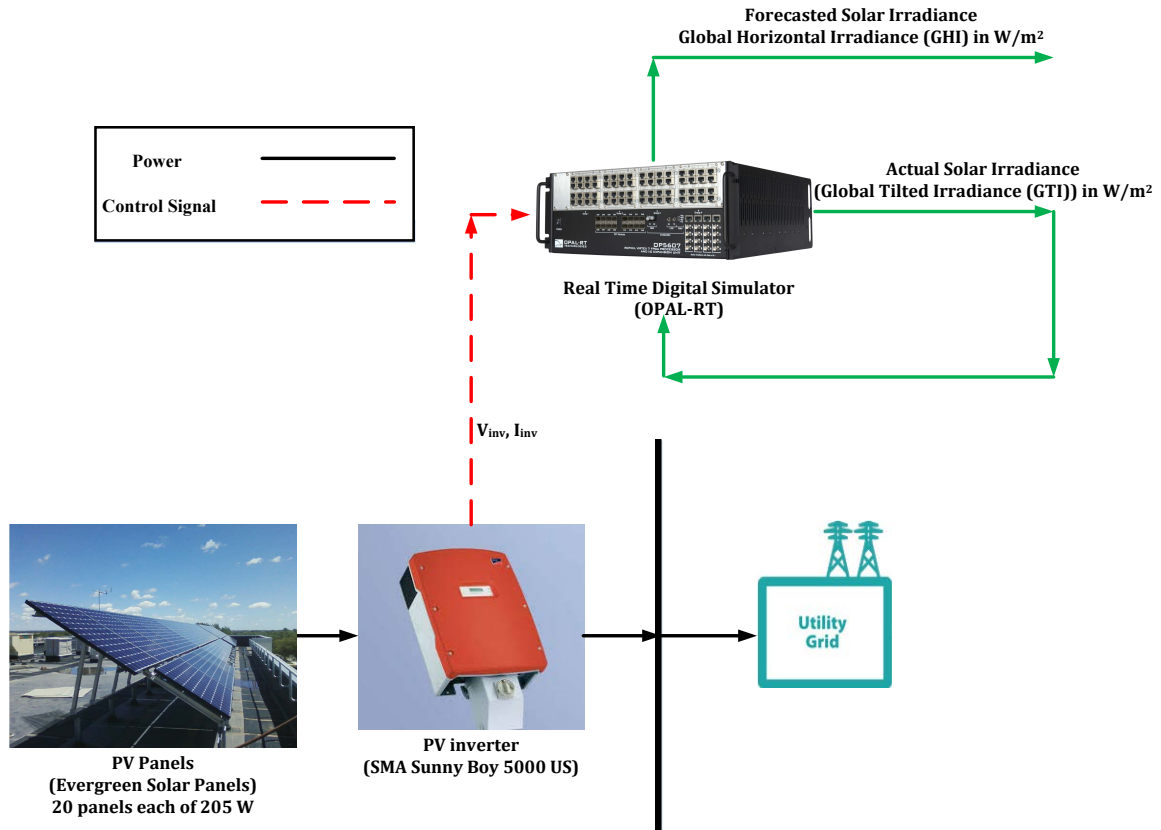


Figure 3.6. Block diagram of implementation of irradiance forecasting in OPAL-RT real-time digital simulator.

In this approach of measuring irradiance from the solar panels, various factors were considered. They are efficiency of solar panel, efficiency of inverter, soiling loss, wiring loss and connection loss. The efficiency of the Evergreen solar panel was taken as 13.04% as obtained from the manufacturer specification sheet [63]. Similarly, the efficiency of the SMA Sunny Boy SB 5000US inverter was taken as 96.7% as obtained from the manufacturer specification sheet [90]. Soiling loss is the loss that occurs due to dirt and other foreign matter on the surface of the solar panel. These foreign matter prevent solar radiation from reaching the cells. Soiling loss was taken to be 2%. Wiring loss is the resistive loss in the DC and AC wires which are used for connecting solar panels, inverters,

and other parts of the PV system. Wiring loss was taken to be 2%. Likewise, connection loss is the resistive loss in the electrical connectors in the PV system. Connection loss was taken to be 0.5%. These losses are taken into consideration as per [91].

Figure 3.7 shows simulation model developed in MATLAB/Simulink, incorporated with RT-LAB to measure solar irradiance in real time. The model contains two top level subsystems: master (SM) and console(SC) subsystems for computations. The master and console subsystems are shown in Figure 3.8 and Figure 3.9, respectively. The master subsystem consists of computational elements of the model whereas the console subsystem consists of Simulink blocks related to display and acquisition of data [92]. The communication between these two subsystems is performed through OpComm blocks as shown in Figure 3.8 and Figure 3.9. These OpComm blocks are used to enable and save communication setup information. The sample time was set to about 5×10^{-5} s for the system.

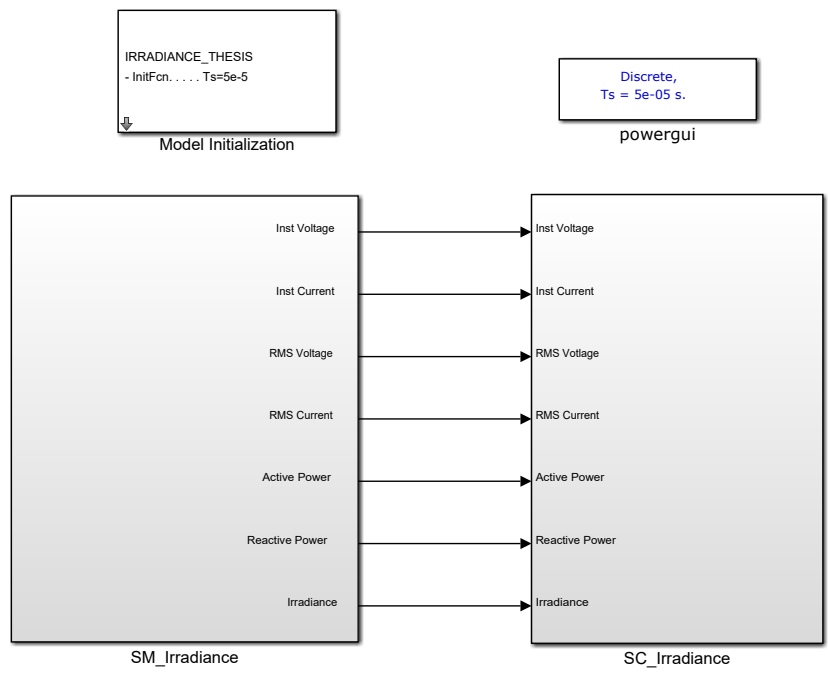


Figure 3.7. MATLAB/Simulink model for measuring solar irradiance with solar panels as sensors.

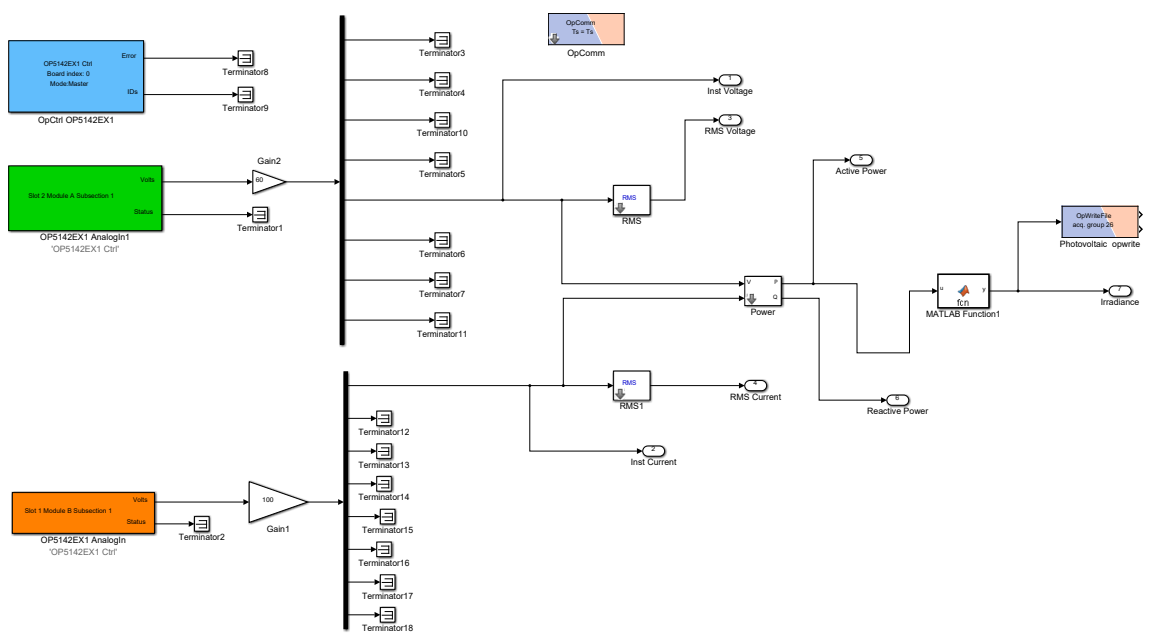


Figure 3.8. Master (SM) subsystem for the model shown in Figure 3.7.

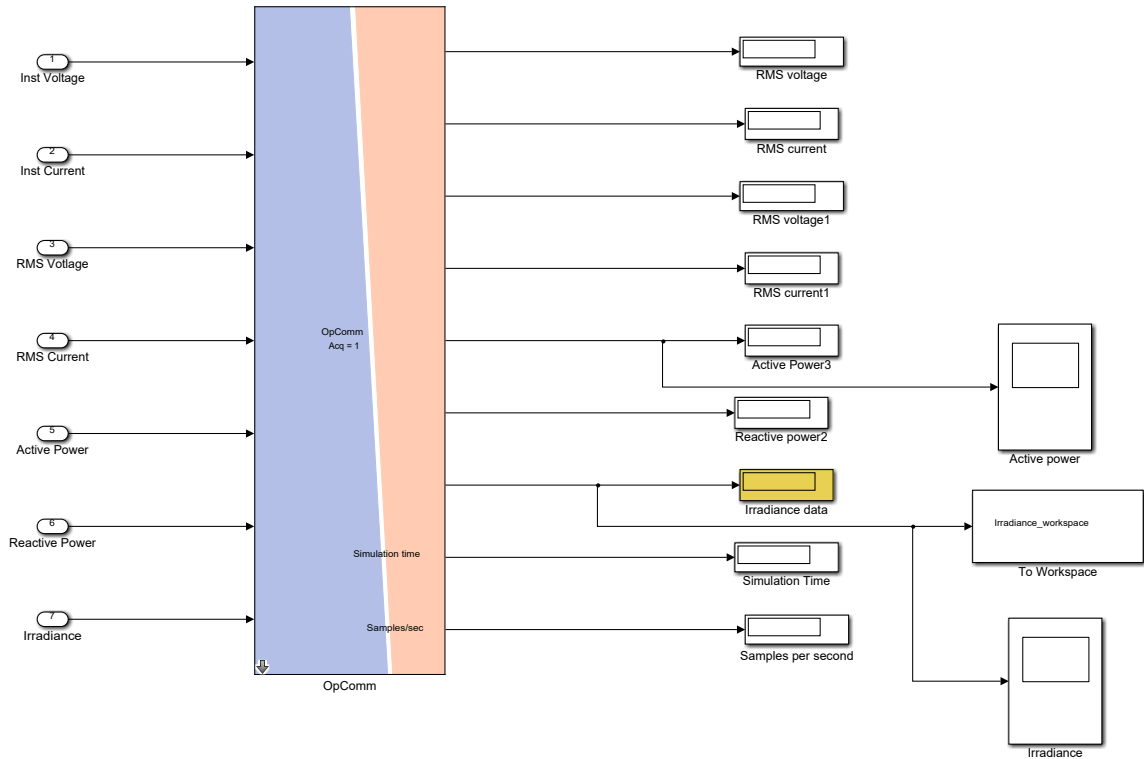


Figure 3.9. Console (SC) subsystem for the model shown in Figure 3.7.

3.3 Experimental setup for testing EMS (optimization of energy resources) in the micro-grid testbed

Figure 3.10 shows the microgrid testbed for testing scheduling and dispatch algorithms for the microgrid. The sources of energy in the testbed are 10.4 kW natural gas generator and PV system. The energy storage system is battery bank. In other words, the test setup consisted of 10.4 kW natural gas generator (Kohler generator), 4.1 kW PV system (Evergreen solar panels and SMA Sunny Boy inverter), 6 kW hybrid inverter/charger (Xantrex inverter/charger), lithium iron phosphate battery (International Battery), automatic load bank and OPAL-RT real-time digital simulator as central controller as shown in Figure 3.10. The OPAL-RT communicates with hybrid inverter/charger and BMS via CAN bus. It also sends control signal to the generator so as

to turn ON or OFF.

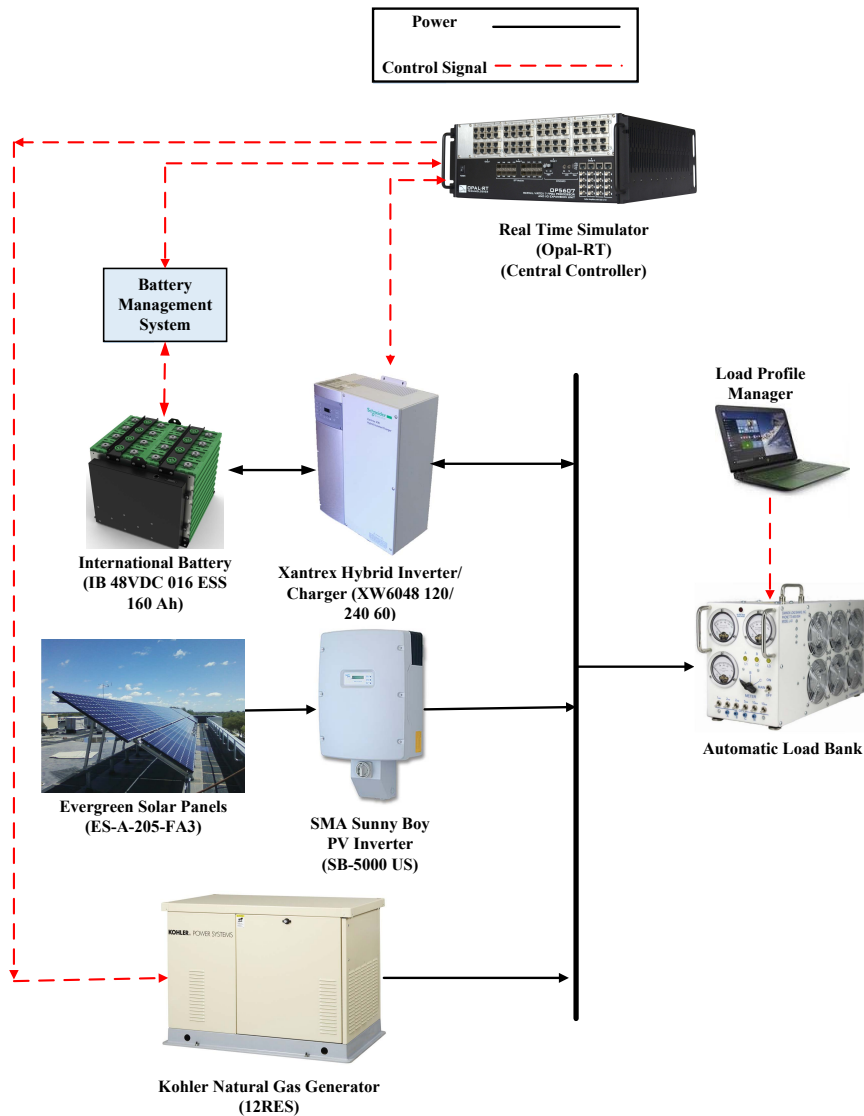


Figure 3.10. Microgrid testbed.

Figure 3.11 shows the connection of the inverter/charger with the battery bank and the AC bus. It was connected with the central controller through CAN physical layer with ISO standard 11898-2 high speed transmission terminated with 120 Ω resistor connection for matching the impedance of the physical layer. The rated speed is 250 kilobytes per second (kbps).

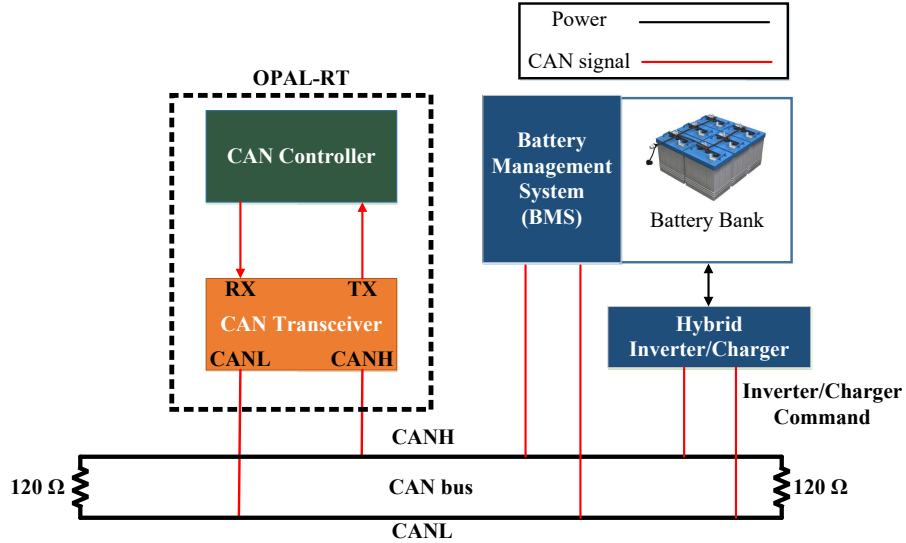


Figure 3.11. Inverter/charger connection with battery and AC bus.

3.4 Optimization model

Generator and battery are the two major components of the microgrid. The cost component of generator is only considered in this optimization model. The generator cost includes fuel consumption cost, maintenance cost, startup cost, generator hourly replacement cost, and emission cost. Only fuel consumption cost and generator hourly replacement cost are included in the model. The amount of fuel consumed by the generator per hour can be calculated by using Equation 2.1. The total fuel cost was calculated by multiplying the fuel volume per hour with fuel cost per unit volume as shown in Equation 3.4.

$$C_i(P_{G,i}) = C_{natural\ gas} \times \sum_{t=1}^{24} (a_i \times P_{G,i}^2(t) + b_i \times P_{G,i}(t) + c_i \times U_{i,t}) \quad (3.4)$$

$$U_{i,t} \times P_{G,imin} \leq P_{G,i}(t) \leq U_{i,t} \times P_{G,imax} \quad \forall t \in T, \forall i \in N \quad (3.5)$$

where N is the number of generators; C_i is the operating cost of the i^{th} generator in \$/hour; $P_{G,i}(t)$ is the generator output power in kW; a_i and b_i are coefficients of $P_{G,i}^2(t)$ and $P_{G,i}(t)$, respectively; c_i is the constant; $U_{i,t}$ is the generator ON/OFF indicator or status with 1 for ON and 0 for OFF status; $P_{G_i,min}$ and $P_{G_i,max}$ are the minimum and maximum power, respectively that can be delivered by the generator.

The lifetime of the generator was calculated to determine the generator hourly replacement cost. It depends on factors such as timely maintenance and usage [93]. From the manufacturer's documents of Kohler 12RES, the lifetime of the natural gas generator is 5 years i.e. 43800 hours. The generator's hourly replacement cost was calculated by using

$$\text{Generator hourly replacement cost} = \frac{\text{Initial investment on the generator}}{\text{Lifetime of the generator}} \quad (3.6)$$

The emission cost of the generator has been neglected because the natural gas produces comparatively lesser greenhouse gases as compared to diesel generators. The startup and shutdown costs of the generators were also neglected as the generator considered in the microgrid test system was small one. Thus, the total generator use cost is the summation of generator fuel cost and the hourly replacement cost. Thus, the objective function of the optimization problem for a day is

$$\text{Minimize } C_{\text{natural gas}} \times \sum_{t=1}^{24} \sum_{i=1}^N (a_i \times P_{G,i}^2(t) + b_i \times P_{G,i}(t) + c_i \times U_{i,t}) + \sum_{t=1}^{24} \sum_{i=1}^N U_{i,t} \times C_{i,hrc} \quad (3.7)$$

The constraints for the optimization model are shown below:

i) Power balance equation

$$P_{G,i}(t) - P_{batt}(t) = P_{load}(t) - P_{PV}(t) \quad \forall t \in T, \forall i \in N \quad (3.8)$$

ii) Generator loading limits

$$U_{i,t} P_{G,imin} \leq P_{G,i}(t) \leq U_{i,t} P_{G,imax} \quad \forall t \in T, \forall i \in N \quad (3.9)$$

iii) Limits for SOC of the battery

$$SOC_{min} \leq SOC(t) \leq SOC_{max} \quad \forall t \in T \quad (3.10)$$

iv) Battery charging and discharging rate limit

$$P_{batt,max_disch} \leq P_{batt}(t) \leq P_{batt,max_ch} \quad \forall t \in T \quad (3.11)$$

where,

t	Time of a day in hour
N	Number of generators
$P_{Gi,t}$	Output power of i^{th} generator at time t in kW
$C_{i,hrc}$	Hourly replacement cost of the i^{th} generator in $\$/hour$
$U_{i,t}$	i^{th} generator's ON/OFF binary status
$P_{batt}(t)$	Battery power at time t in kW (It is negative for discharging and positive for charging)
$P_{load}(t)$	Load at time t in kW
$P_{PV}(t)$	PV Output power at time t in kW
$P_{Gi,min}$	Minimum power that can be generated from the i^{th} generator at time t in kW
$P_{Gi,max}$	Maximum power that can be generated from the i^{th} generator at time t in kW
SOC_t	SOC of battery at time t
SOC_{min}	Minimum allowable SOC of battery
SOC_{max}	Maximum allowable SOC of battery
P_{batt,max_disch}	Maximum discharge rate of the battery in kW
P_{bat,max_ch}	Maximum charge rate of the battery in kW

The generator fuel consumption versus load plot of the generator is shown in

Figure 3.12.

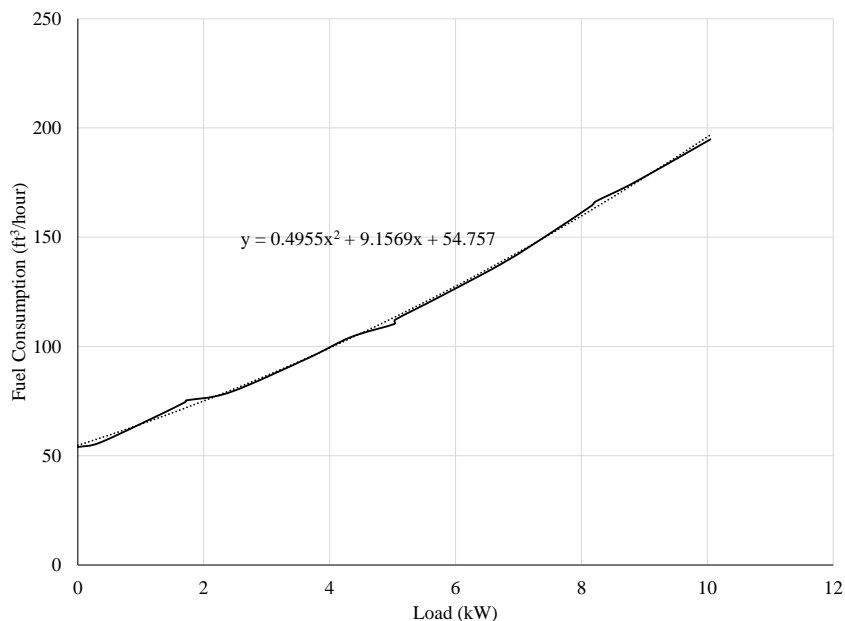


Figure 3.12. Plot of generator fuel consumption versus load for the natural gas generator (Kohler 12RES).

The coefficients a, b, and c were calculated using regression analysis. They are tabulated in Table 3.2. The initial cost of the generator was \$3,700 and the lifetime of the generator was 5 years. This resulted in the hourly replacement cost of the generator to be \$0.084 per hour using Equation 3.6.

Table 3.2. Coefficients of fuel consumption curve of 10.4 kW generator.

Coefficients	Values
a	$0.4955 \text{ ft}^3 / (\text{kW})^2 \text{ h}$
b	$9.1569 \text{ ft}^3 / \text{kW h}$
c	$54.757 \text{ ft}^3 / \text{h}$

The average cost of the natural gas was taken as \$0.0047 per cubic feet. A single generator was considered i.e. $N = 1$. The operation of the generators was limited to a minimum of 30% of the rated output. The SOC constraint as shown in Equation 3.10 ensures that the battery is operated within certain predefined SOC limits so as to guarantee

longer lifetime and to serve the load. For lithium iron phosphate battery the minimum and maximum SOC limits were taken as 10% and 90%, respectively. The battery should be capable enough to discharge to serve the load. The discharge rate of the battery was set to 1C (160 A) as per the specification sheet of the International Battery. Similarly, the charge rate was set to 0.3C. The battery charge and discharge limit constraint shown in Equation 3.11 ensures that the operation of the battery does not exceed the limits.

3.5 Procedure for implementing EMS in the testbed

Figure 3.13 shows a laboratory setup for experimenting EMS. The optimization was performed in IBM ILOG CPLEX Optimization Studio Version 12.6.1 and the results i.e. the scheduled output were run in the central controller so as to turn ON/OFF the generator and charge/discharge the battery accordingly (See Figure 3.14). Programmable load i.e., automatic load bank was programmed via a software called 'Load Profile Manager'.

Figure 3.15 shows a screenshot of the software. In this software, the power in watt and running time were provided. The load profile that was programmed in the load bank was the scaled down load from Nemiah Valley microgrid in Canada. Table 3.3 shows the 24 hour load profile of Nemiah Valley microgrid of January 3, 2012 and the scaled load used in the experiment to match the power output in the laboratory. The maximum limit of the generator was limited to 6 kW so as to match the maximum scaled load. The scaled load is the net load i.e. difference between the actual scaled load and the forecasted PV power. In other words, the PV power is incorporated in the net load i.e. the PV power forecasting is assumed to be ideal in this case study. The load forecasting is also assumed to be accurate so that the scheduled load is same as the actual load.

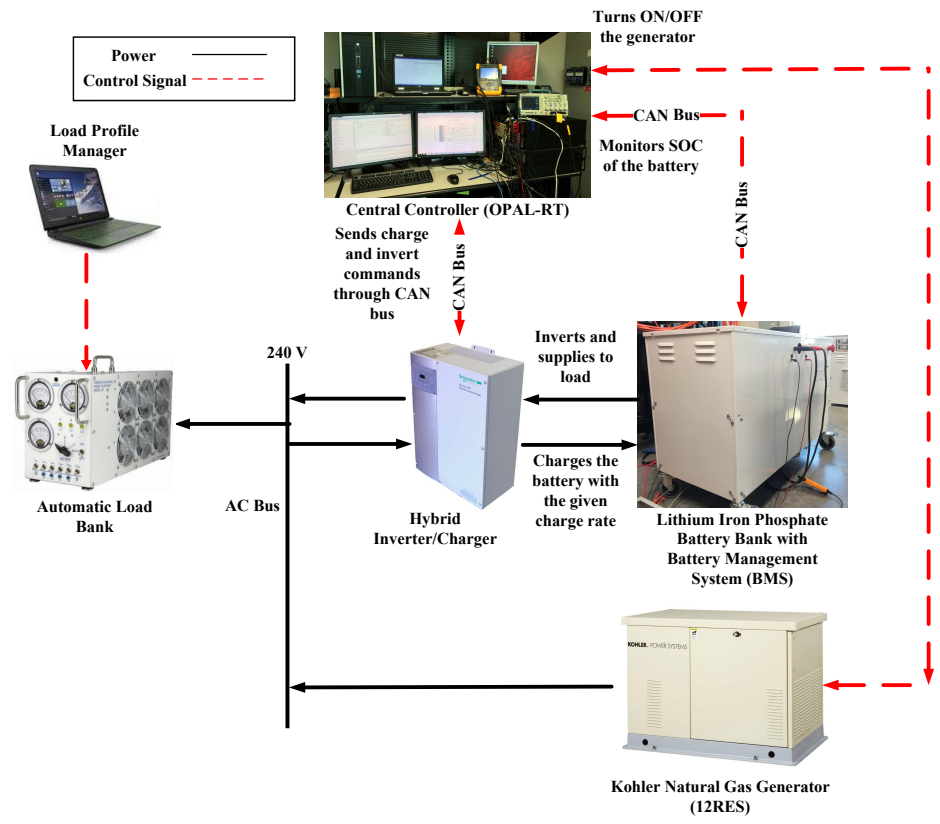


Figure 3.13. Plot of generator fuel consumption versus load for the natural gas generator (Kohler 12RES).

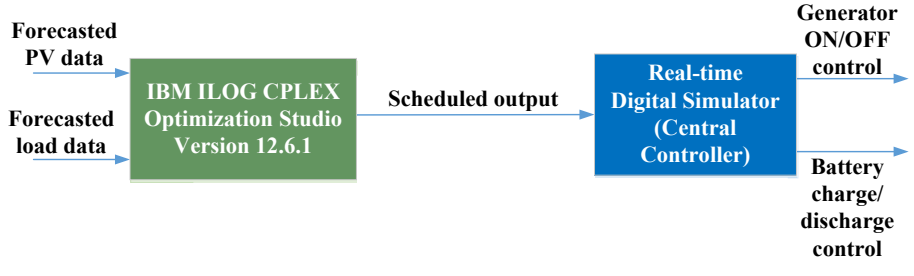


Figure 3.14. Scheduling and dispatch procedures carried out in the laboratory.

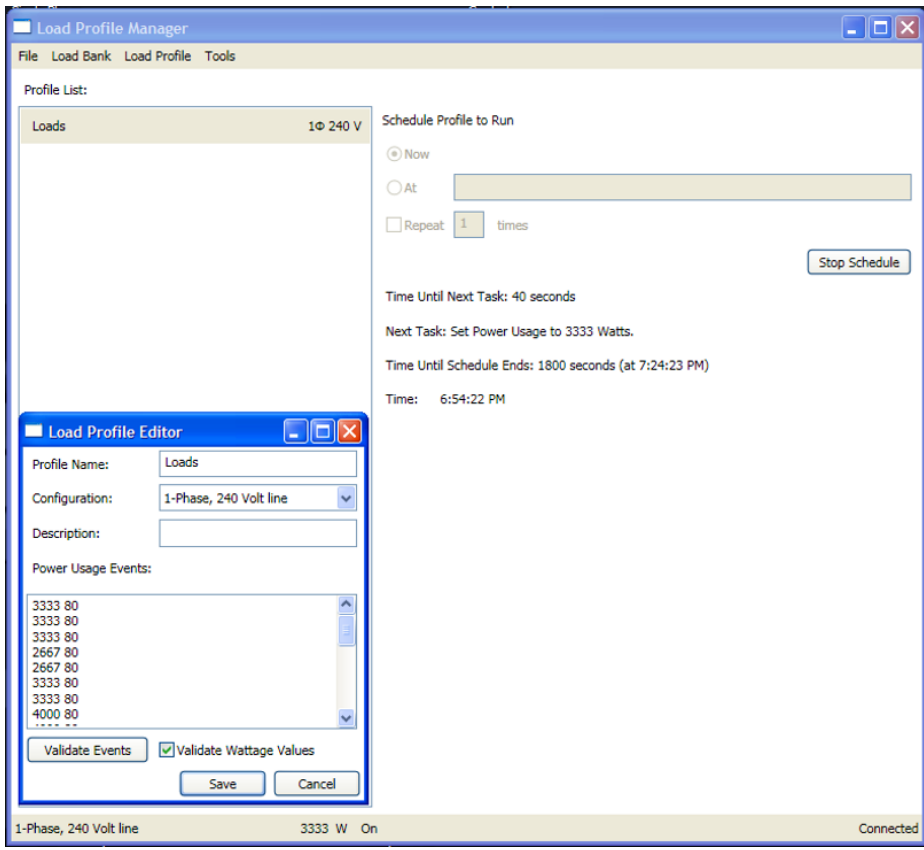


Figure 3.15. Screenshot of load profile manager software.

Table 3.3. Twenty four hour original load of January 3, 2012 from Nemiah Valley microgrid in Canada and scaled load used in the experiment

Hour	Actual load (kW)	Net Load (kW)
1	34.344	3.330
2	34.294	3.330
3	35.041	3.330
4	33.881	2.670
5	33.81	2.670
6	34.251	3.330
7	34.542	3.330
8	36.958	4.000
9	46.781	4.000
10	62.928	5.330
11	58.111	5.330
12	51.185	4.670
13	46.825	4.000
14	45.811	4.000
15	44.149	4.000
16	44.613	3.330
17	45.612	4.000
18	44.945	4.000
19	42.623	3.330
20	39.983	3.330
21	38.266	3.330
22	37.654	2.670
23	20.732	2.000
24	19.165	2.000

Figure 3.16 shows simulation model developed in MATLAB/Simulink, incorporated with RT-LAB to implement the scheduled output from the CPLEX. The model contains two top level subsystems: master (SM) and console(SC) subsystems for computations. The master and console subsystems are shown in Figure ?? and Figure ??, respectively.

The master subsystem consists of computational elements of the model whereas the console subsystem consists of Simulink blocks related to display and acquisition of data [92]. The communication between these two subsystems is performed through OpComm blocks. These OpComm blocks are used to enable and save communication setup information. The sample time was set to about 8×10^{-4} s for the system.

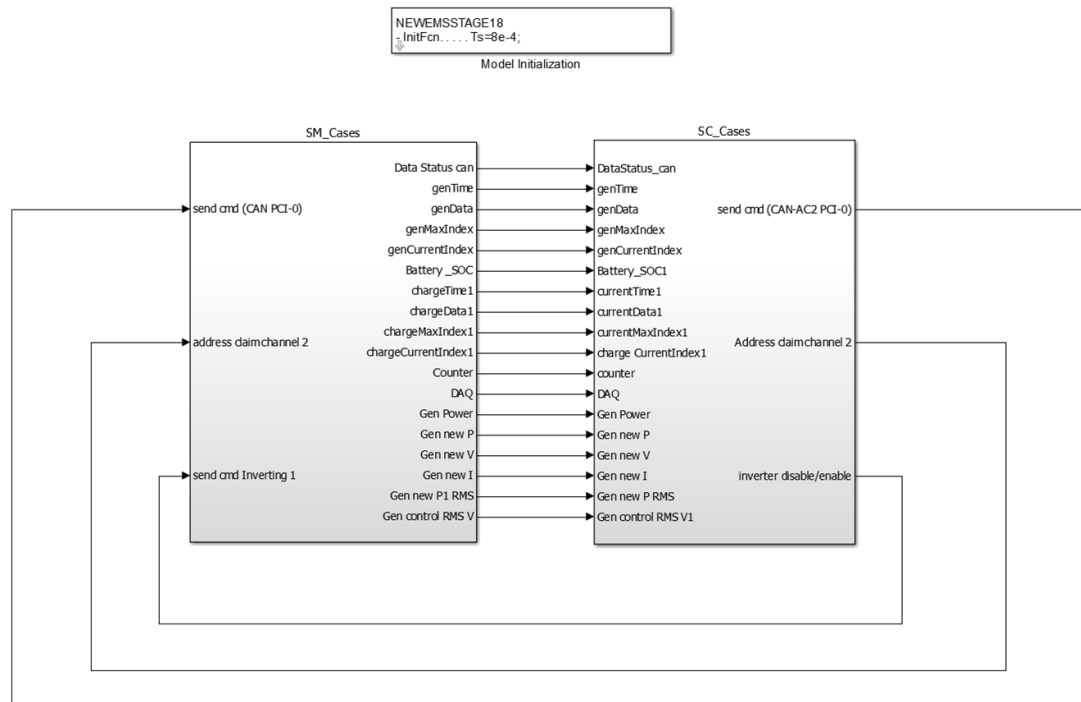


Figure 3.16. MATLAB/Simulink model for dispatching the scheduled output from the optimization tool.

The fuel consumption of generators at different load was measured using Sierra 620S fuel flow meter. The measured data was acquired using National Instrument's LabVIEW Data Acquisition System in the laboratory. The measured data was then compared with the theoretical fuel consumption.

CHAPTER 4 RESULTS AND ANALYSIS

Chapter 4 presents results and analysis of the solar irradiance forecasting. The results of the case study, presented in Chapter 3, are discussed in this chapter. The forecasting technique was validated for a number of days with the historical irradiance data. The forecasting error analysis is also presented in this chapter. Similarly, the results of the implementation of the solar irradiance forecasting in the OPAL-RT real-time digital simulator are also presented. Likewise, the implementation of EMS in the developed microgrid testbed is also shown.

4.1 Validation of the forecasting method using historical irradiance data

As an example of validation of the algorithm, solar irradiance for August 16, 2011 was considered. Fig. 4.1 shows a plot of solar irradiance for this day. The red, green, and blue curves indicate irradiance for high, medium, and low energy states, respectively. The magenta and black curves indicate actual and forecasted irradiance, respectively. The actual irradiance plot for the first four hours of the day was closer to the low energy state, which caused the forecasted irradiance to remain in the low energy state. However, the irradiance for the first four hours in the morning was forecasted on the basis of the state of August 15, 2011. Fig. 4.2 shows the irradiance prediction for August 15. Here, the irradiance was forecasted to be high energy state. This resulted in the forecasted irradiance for the first four hours of August 16 to remain in the high energy state. The RMSE, and MAPE for this day were calculated to be $127.2 \text{ W}/\text{m}^2$ and 47.5%, respectively. The RMSE and MAPE over a one year period (8760 hours) for the year 2011 were computed to be $106.8 \text{ W}/\text{m}^2$ and 31.9%, respectively.

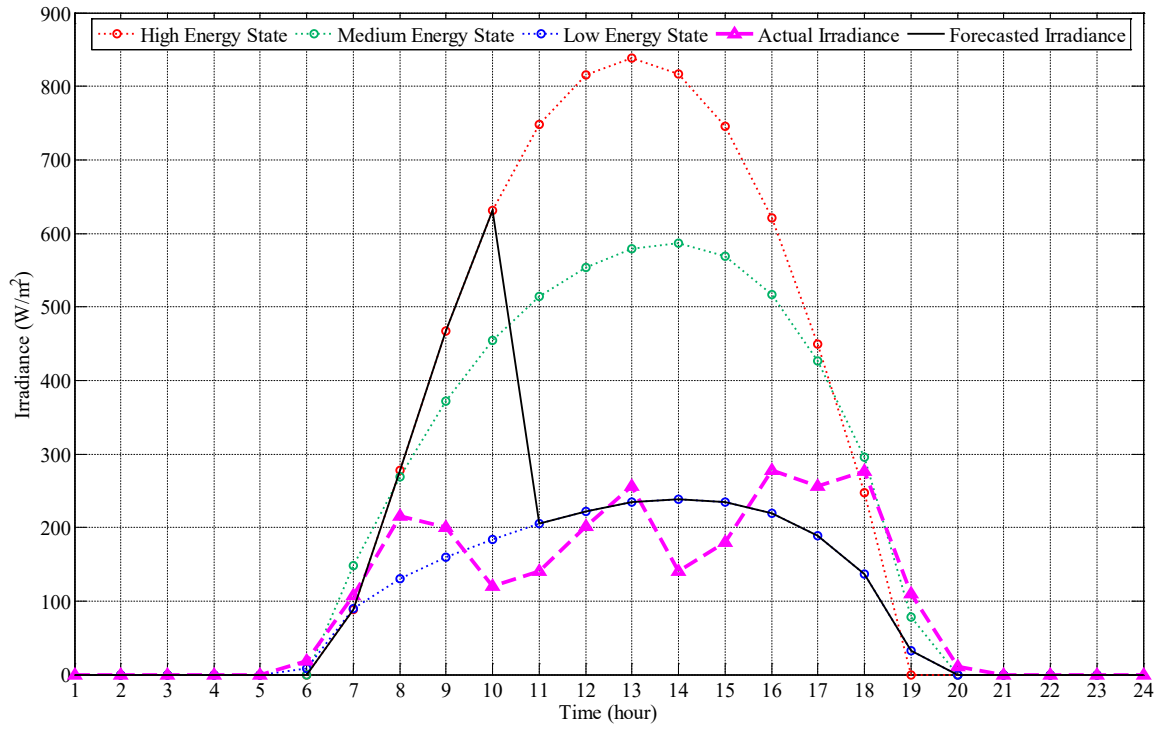


Figure 4.1. Irradiance variation for August 16, 2011.

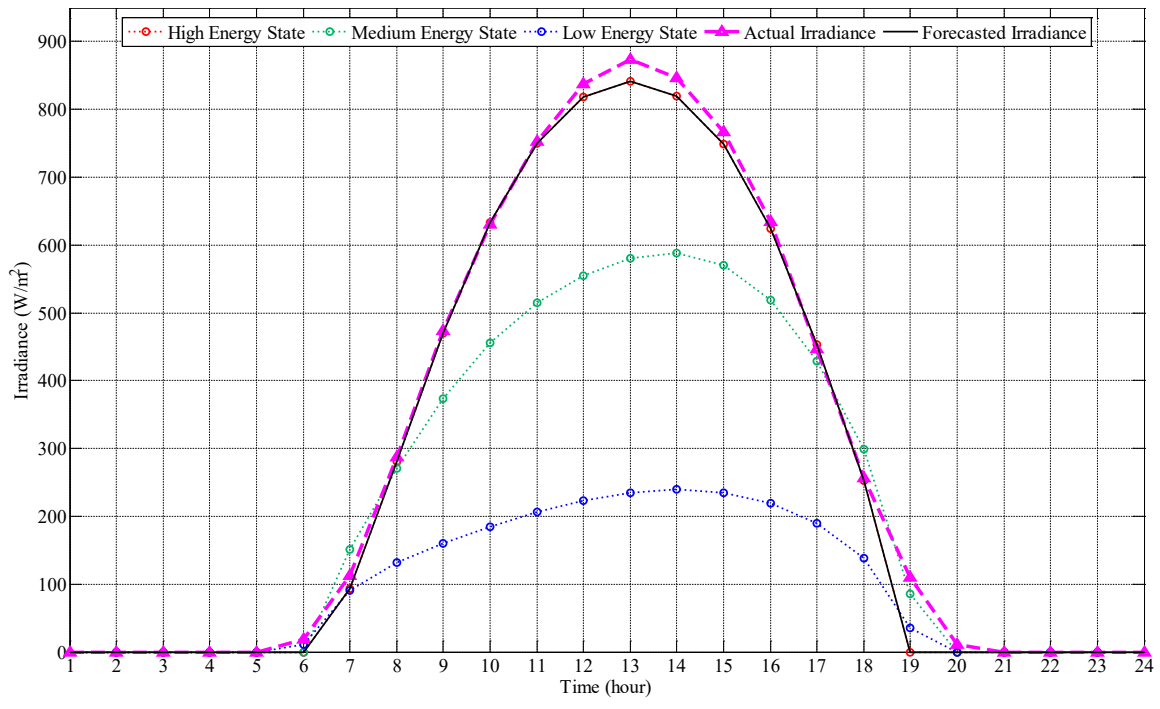


Figure 4.2. Irradiance variation for August 15, 2011.

Similarly, another validation was performed for May 14, 2008, which falls in the

leap year. Fig. 4.3 shows the plot of solar irradiance for this day. The actual irradiance plot for the first four hours of the day was closer to the high energy state, which caused the forecasted irradiance to remain in the high energy state. The first four hours irradiance was predicted to be in the low energy state as the irradiance on the previous day, May 13, 2008, was predicted to lie in low energy state as shown in Fig. 4.4. The RMSE, and MAPE for this case were calculated to be $102.6 W/m^2$ and 18.1%, respectively. The RMSE and MAPE over a one year period (8784 hours) for the year 2008 was computed to be $99.6 W/m^2$ and 29.9%, respectively.

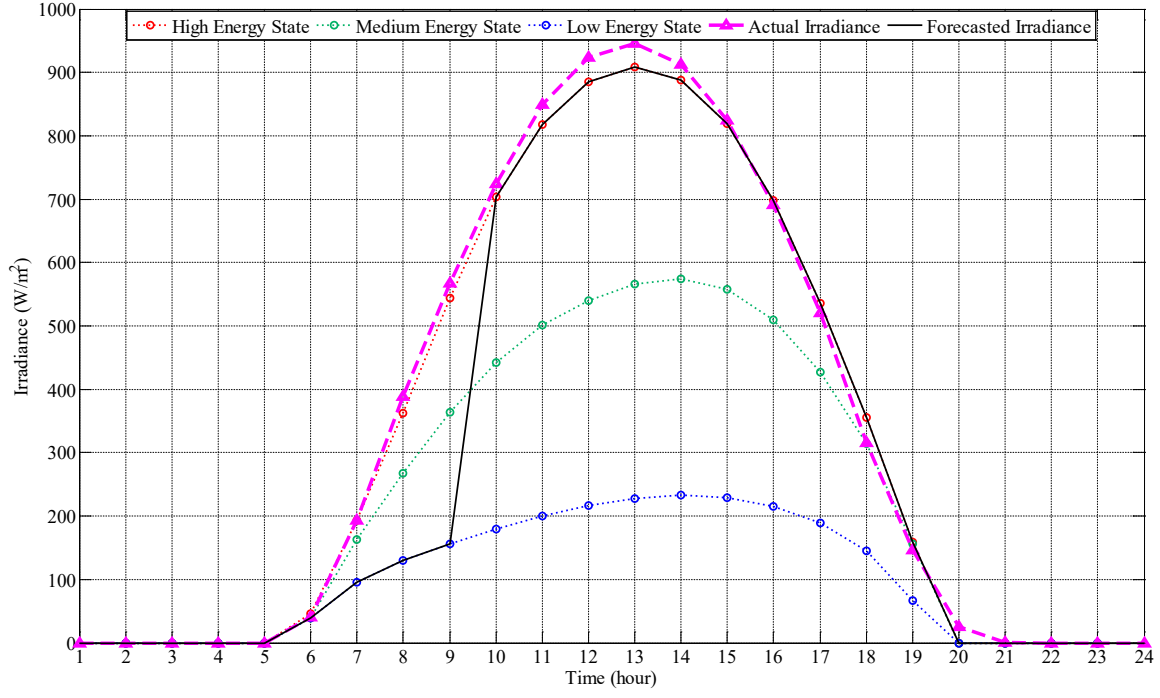


Figure 4.3. Irradiance variation for May 14, 2008.

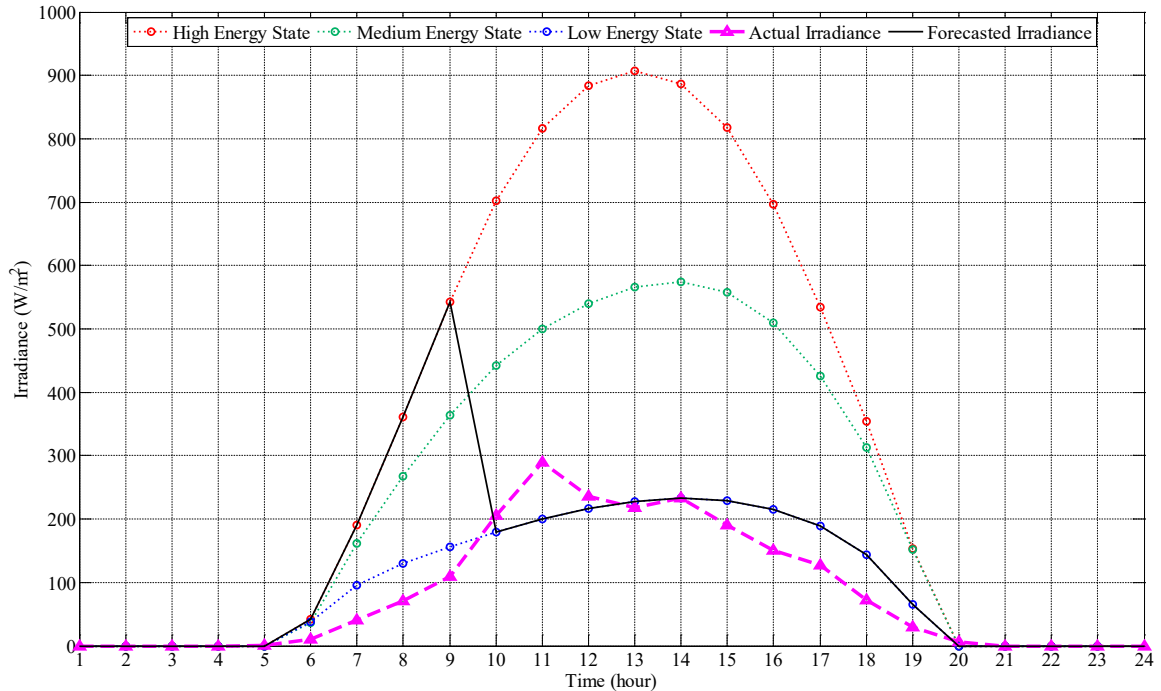


Figure 4.4. Irradiance variation for May 13, 2008.

Likewise, Figure 4.5 shows the plot of solar irradiance for July 24, 2012, which falls in the leap year. The actual irradiance plot for the first four hours of the day was closer to a high energy state, which resulted forecasted irradiance to lie in the high energy state. The first four hour irradiance was predicted to be in low energy regime as the irradiance on the previous day, i.e. July 23, 2012, was predicted to lie in low energy regime as shown in Figure 4.6. The RMSE, and MAPE for this case were calculated to be 79.4 W/m^2 and 21.7%, respectively. The RMSE and MAPE over a one year period (8760 hours) was computed to be 108.4 W/m^2 and 31.9%.

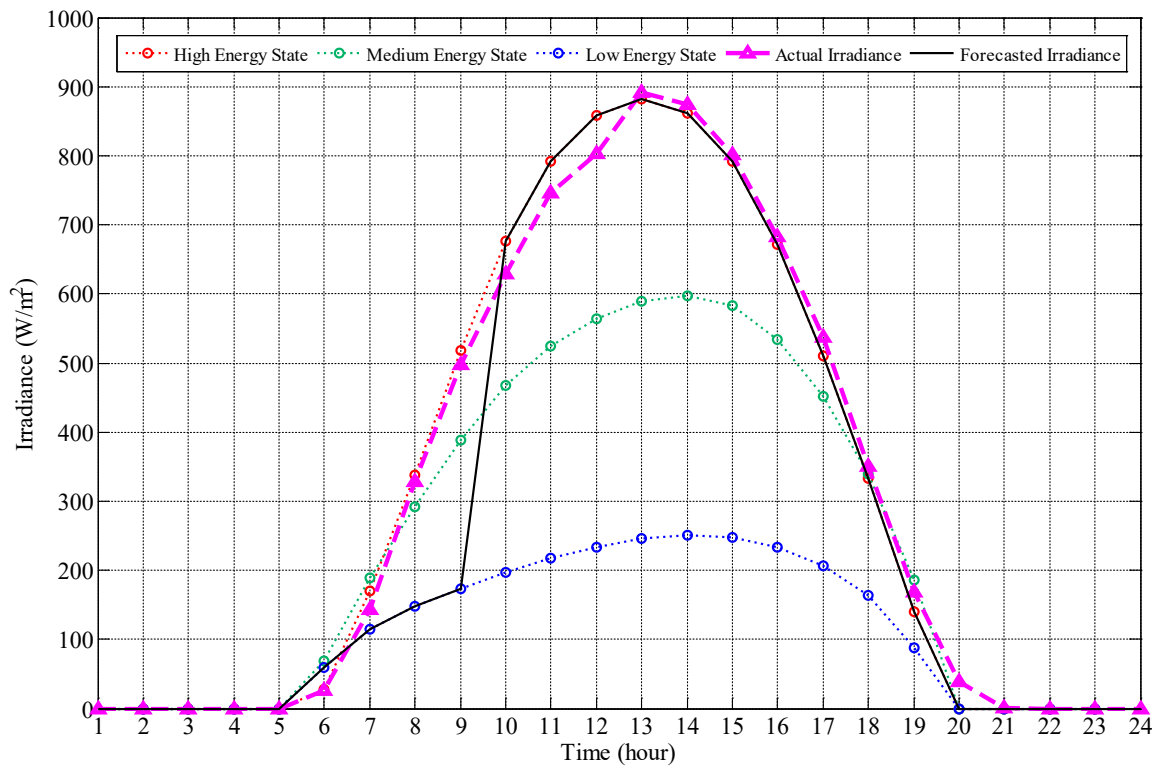


Figure 4.5. Irradiance variation for July 24, 2012.

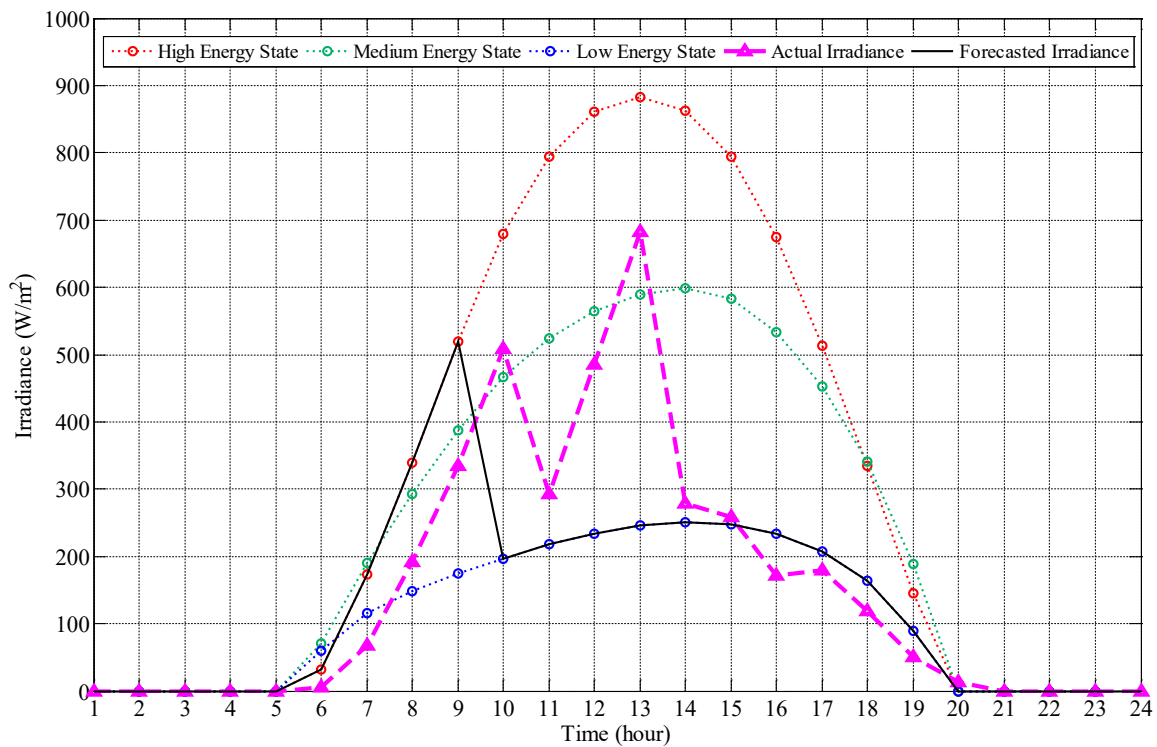


Figure 4.6. Irradiance variation for July 23, 2012.

4.1.0.1 Error assessment

Figure 4.7 shows the box plot of monthly RMSE for the year 2001. The RMSE is comparatively higher during the summer season, since total daylight hours are high as illustrated in Figure 2.22. Higher daylight hours imply a higher number of forecasts and hence higher error. The highest and lowest RMSE were calculated to be 341.8 W/m^2 and 17.5 W/m^2 , respectively. The RMSE throughout the whole year was computed to be 105.8 W/m^2 . However, monthly MAPE, being relative error metric is similar during all the seasons as illustrated in Figure 4.8. The MAPE throughout the whole year was calculated to be 32.9%.

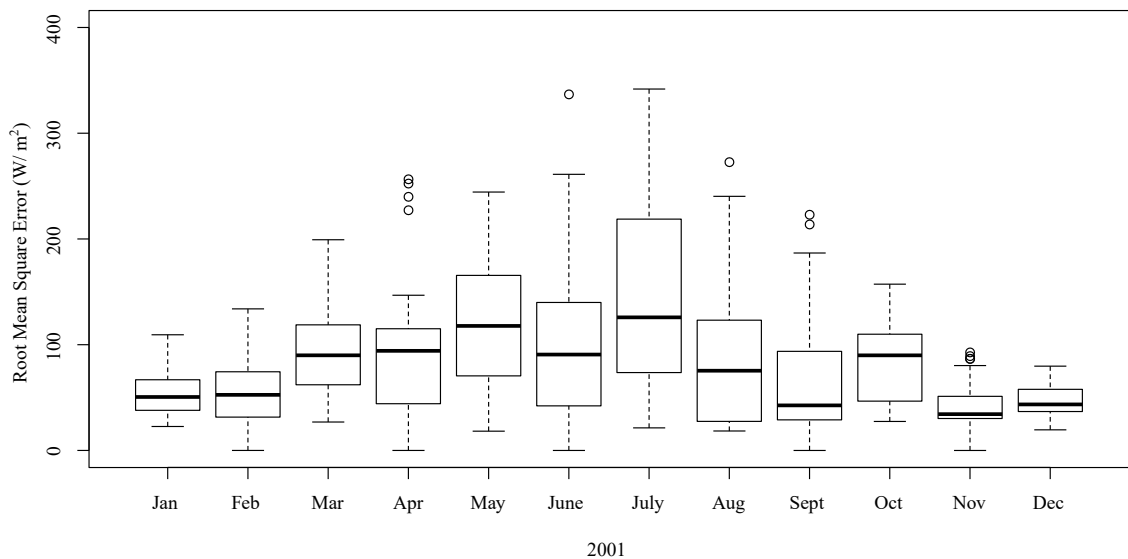


Figure 4.7. Boxplot of monthly RMSE for the year 2001.

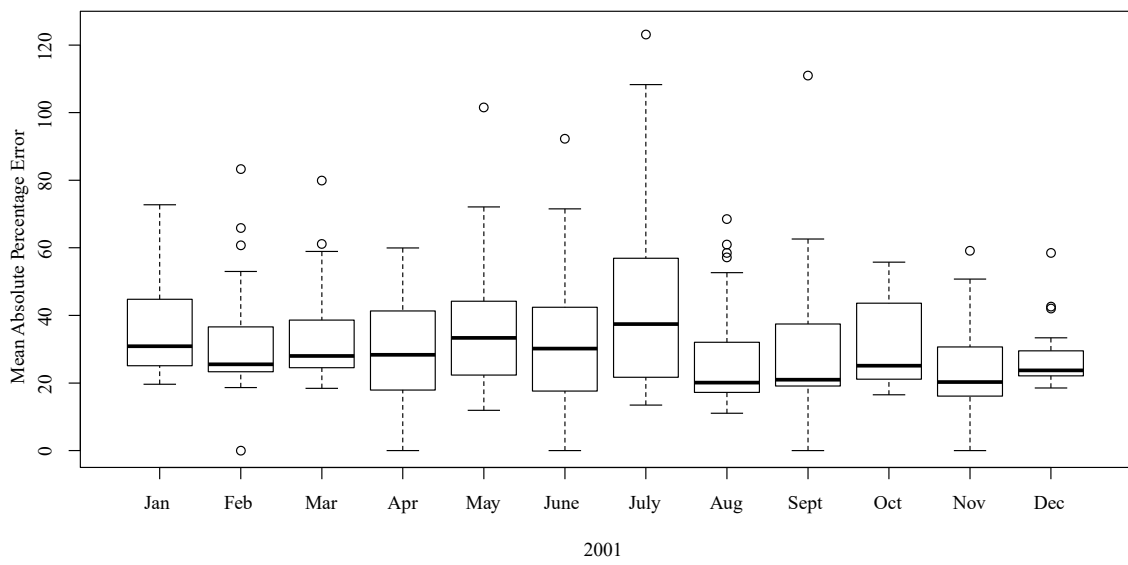


Figure 4.8. Boxplot of monthly MAPE for the year 2001.

Figure 4.9 shows RMSE from 2001 to 2005. For all these years, the RMSE is higher during summer seasons and lower during winter seasons. Table 4.1 shows RMSE throughout the year, maximum RMSE, minimum RMSE and MAPE for the years 2001 to 2005. The upper point in each month indicates the monthly average RMSE plus one standard deviation, while the lower point indicates monthly average RMSE minus one standard deviation.

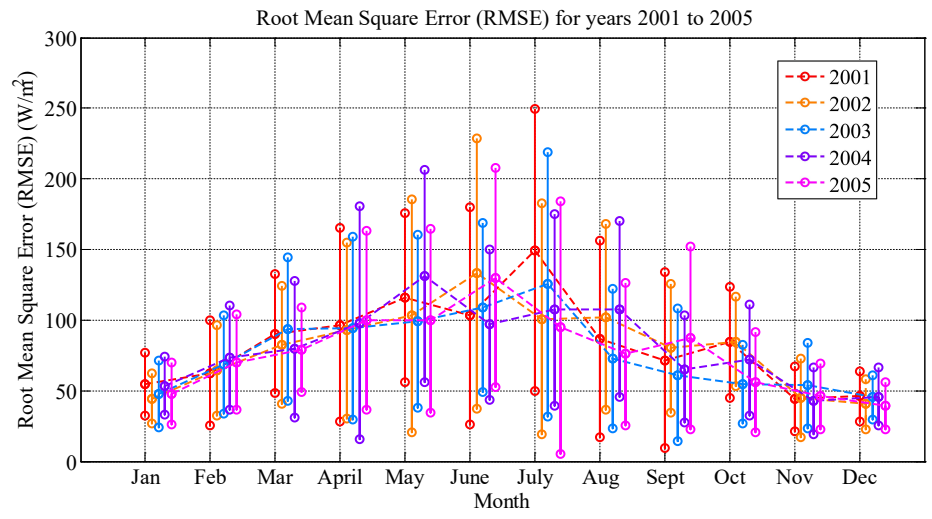


Figure 4.9. RMSE for years 2001 to 2005.

Table 4.1. RMSE for years 2001 to 2005

Year	RMSE throughout the year (W/m^2)	Maximum RMSE (W/m^2)	Minimum RMSE (W/m^2)	MAPE throughout the year (%)
2001	105.8	341.8 (July)	17.5 (June)	32.9
2002	102.9	360.5 (May)	12.4 (Nov)	31.6
2003	96.2	348.5 (July)	14.5 (July)	30.7
2004	100.0	365.8 (May)	14.2 (Dec)	32.3
2005	97.5	306.7 (July)	13.3 (Oct)	31.7

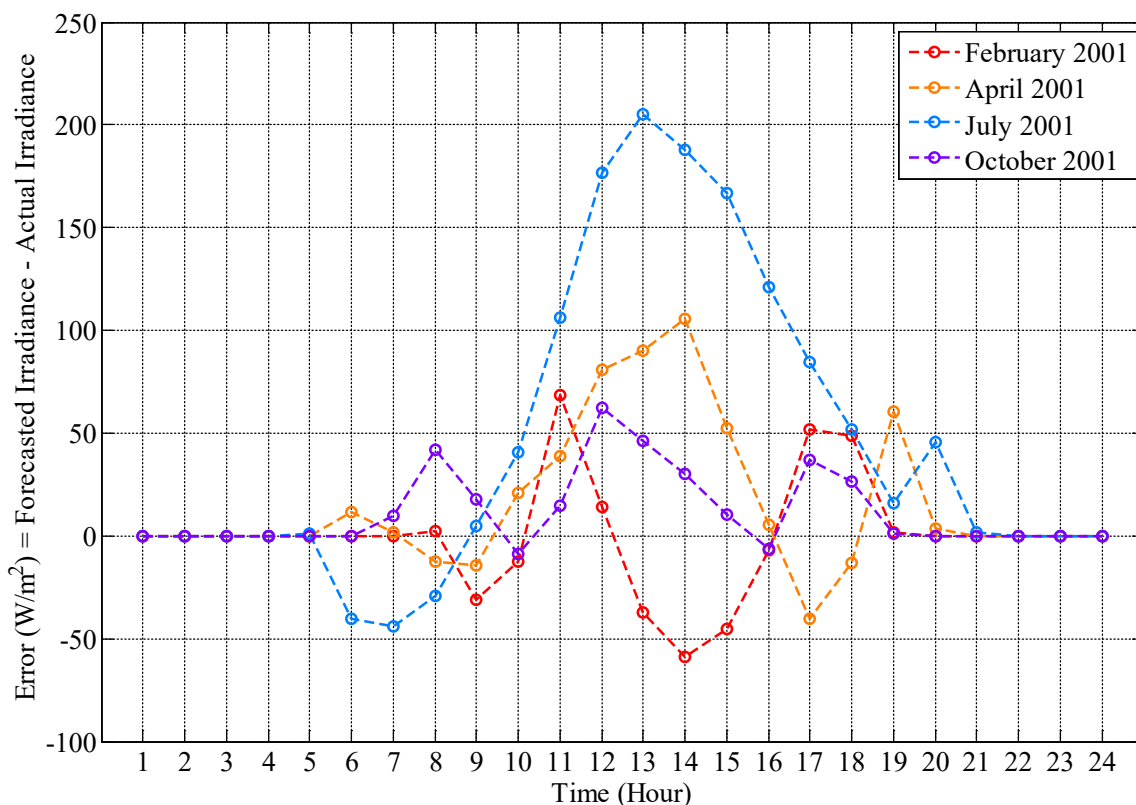


Figure 4.10. Plot of difference between hourly forecasted and actual irradiance for four different months of year 2001.

Figure 4.10 shows hourly error plot for four different months: February for winter, April for spring, July for summer and October for fall for the year 2001. The error is fairly high for the summer month. There is more overestimation in forecasting in July and

underestimation in February. As a future work, this trend in overestimation or underestimation among different months in a year can be taken into consideration to minimize the forecasting error.

4.2 Implementation of solar irradiance forecasting in real-time digital simulator at micro-grid research laboratory

For the implementation of solar irradiance forecasting in real-time digital simulator at the microgrid research laboratory, the first four hours of solar irradiance in the morning was measured using PV panels as sensors.

4.2.1 Irradiance data acquisition using PV panels as sensors

Figure 4.11 shows real-time data acquired through OPAL-RT at Microgrid Research Laboratory in South Dakota State University, Brookings. It shows one minute irradiance data of May 4, 2016. This acquired irradiance data was validated using irradiance sensor i.e. pyranometer.

4.2.2 Irradiance forecasting at the laboratory

Figure 4.12 shows the plot of solar irradiance for June 10, 2015. This result was obtained in real-time by implementing in OPAL-RT. The actual irradiance plot for the first four hours of the day was closer to a low energy state, which resulted forecasted irradiance to lie in the low energy state. The first four hours irradiance was predicted to be in the medium energy regime as the irradiance on the previous day, i.e. June 9, 2015, was predicted to lie in the medium energy regime as shown in Figure 4.13. The RMSE, and MAPE for this case were calculated to be $131.08 \text{ W}/m^2$ and 45.45% , respectively.

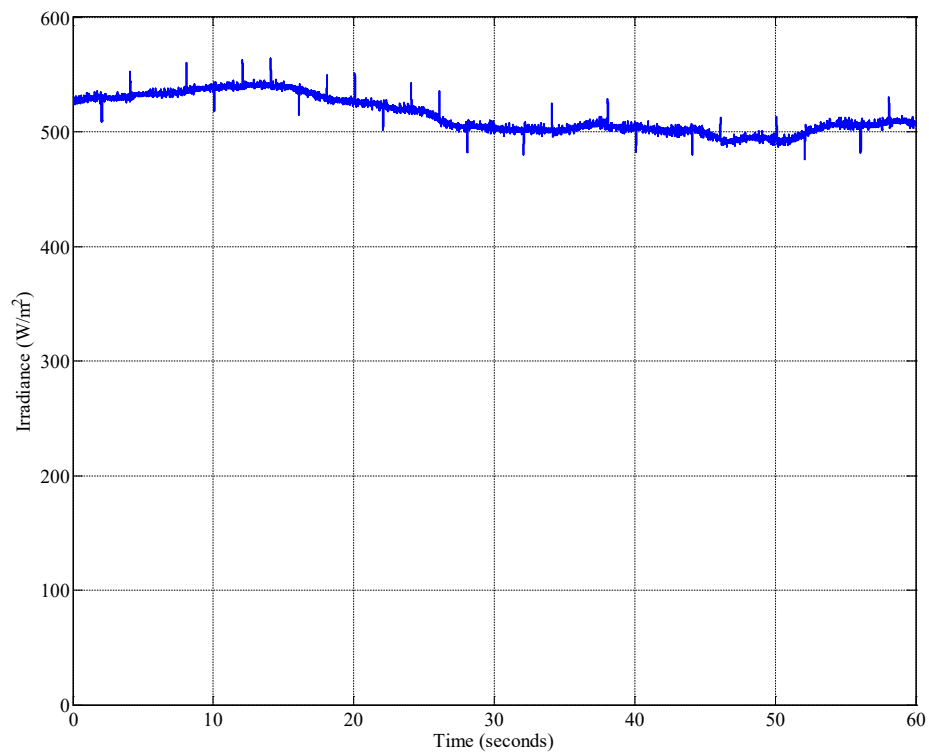


Figure 4.11. Solar irradiance data logged through OPAL-RT in real-time with solar panels as sensors for 60 seconds.

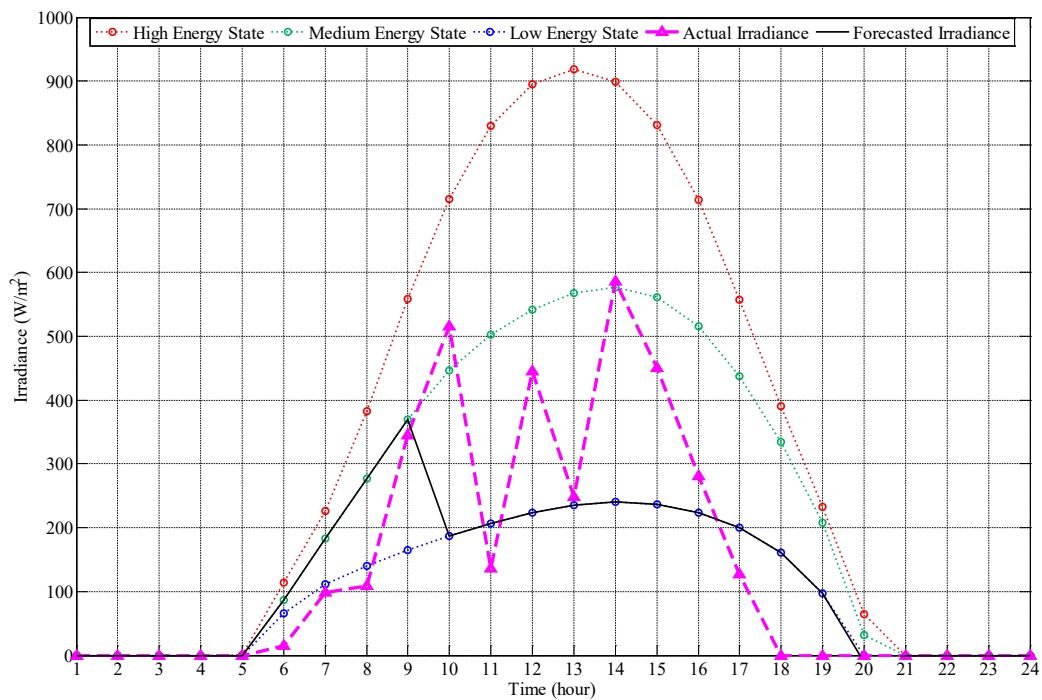


Figure 4.12. Irradiance variation for June 10, 2015.

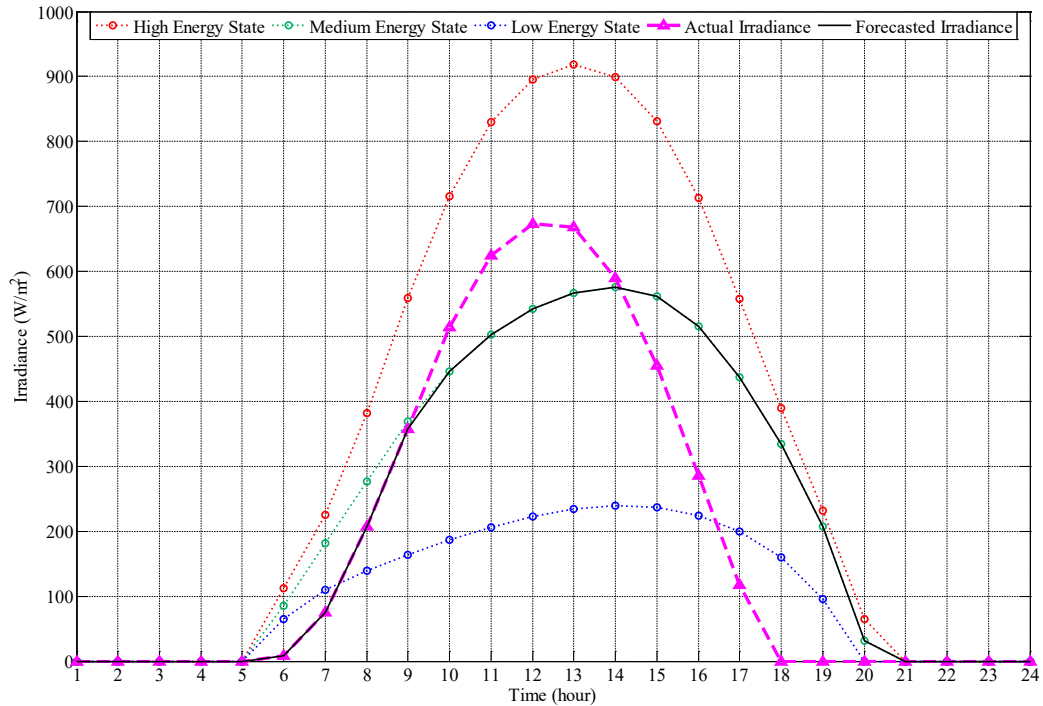


Figure 4.13. Irradiance variation for June 9, 2015.

4.3 Implementation of EMS in the microgrid testbed

The output of the optimization i.e. the scheduled output is shown in Figure 4.14.

The orange colored bars represent generator power, the blue colored bars represent battery power and the green dotted line represents the net load. The optimization was run for 30.67 minutes considering 80 seconds as 1 hour period so as to simulate 24 hours period i.e. a day. It can be observed that the generator operated near to 6 kW so as to operate in its higher efficiency region and to limit the SOC of the battery within the specified range.

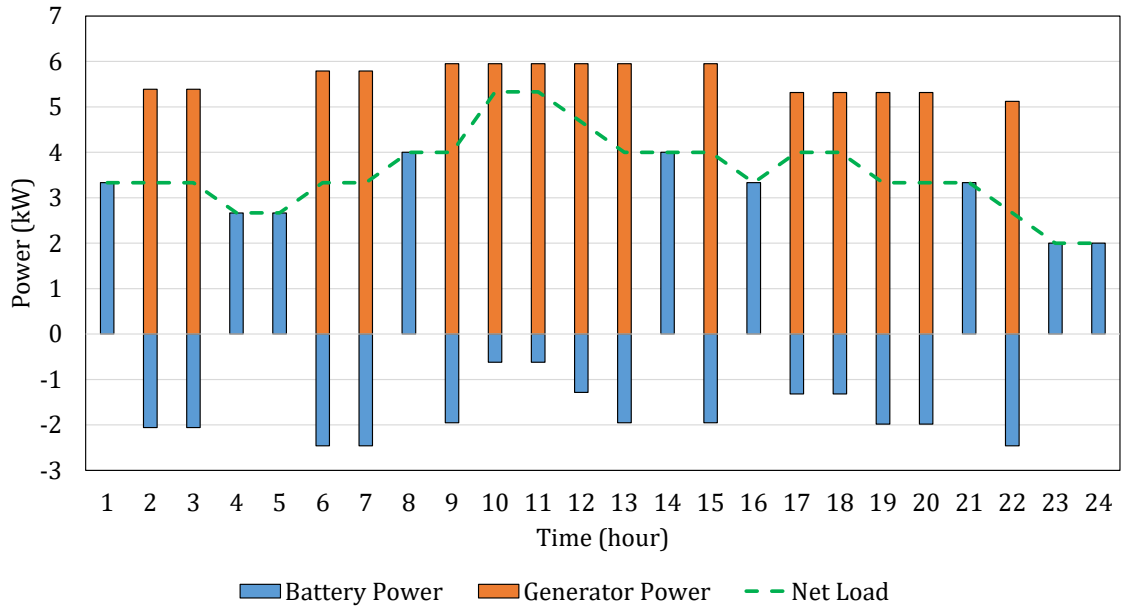


Figure 4.14. Scheduled Power Output.

Table 4.2 shows generator power, battery power and load for the 24 hours. The positive sign in the battery power implies that the battery is being charged and the negative sign implies that it is being discharged. The scheduled output was read in the central controller so as to dispatch generator and inverter/charger accordingly.

Table 4.2. Scheduled output obtained from optimization in CPLEX

Hour	Generator Power (kW)	Battery Power (kW)	Net Load (kW)
1	0.00	-3.33	3.33
2	5.39	2.06	3.33
3	5.39	2.06	3.33
4	0.00	-2.67	2.67
5	0.00	-2.67	2.67
6	5.79	2.46	3.33
7	5.79	2.46	3.33
8	0.00	-4.00	4.00
9	5.95	1.95	4.00
10	5.95	0.62	5.33
11	5.95	0.62	5.33
12	5.95	1.28	4.67
13	5.95	1.95	4.00
14	0.00	-4.00	4.00
15	5.95	1.95	4.00
16	0.00	-3.33	3.33
17	5.32	1.32	4.00
18	5.32	1.32	4.00
19	5.32	1.98	3.33
20	5.32	1.98	3.33
21	0.00	-3.33	3.33
22	5.12	2.46	2.67
23	0.00	-2.00	2.00
24	0.00	-2.00	2.00

Figure 4.15 shows the scheduled SOC of the battery. It can be observed that the SOC was limited within the range of 10% to 90%.

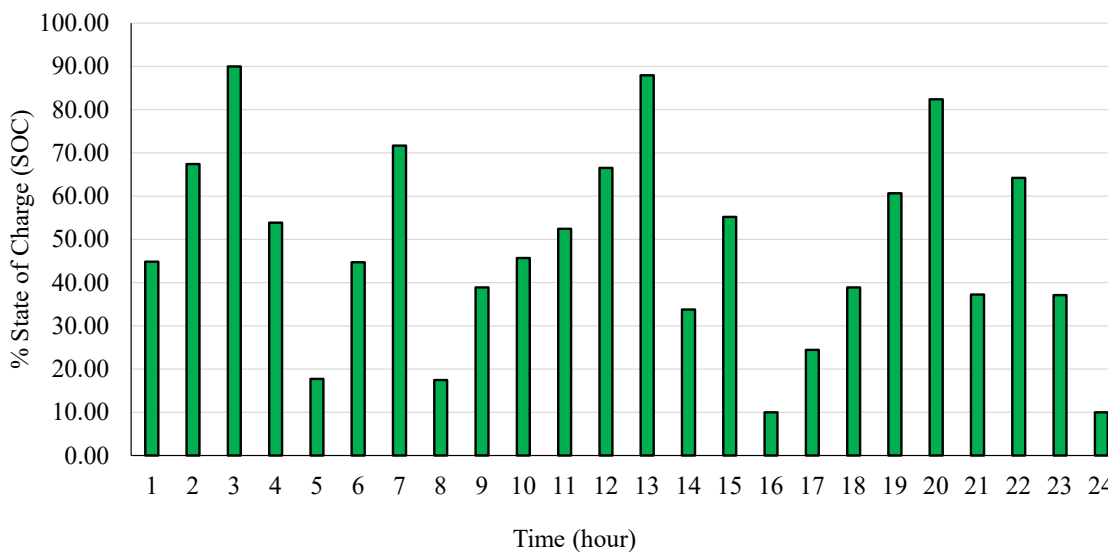


Figure 4.15. SOC of the battery throughout the day.

Figure 4.16 shows plots of generator power, load power, and battery power for the 24 hour period during dispatch stage. There are slight differences among the power obtained in scheduled stage and dispatch stage. This shows that the generator and energy storage system can handle the variations obtained during the dispatch stage. For the case study, the maximum and minimum difference between the scheduled and the actual generator output was computed to be 8.93 kW and 0 kW , respectively. The average power difference between the scheduled and the actual generator outputs were calculated to be 4.07 kW . Similarly, the maximum and minimum difference between the scheduled and the actual battery power were calculated to be 1.05 kW and 0.32 kW , respectively. The average absolute power difference between the scheduled and the actual battery power was computed to be 0.48 kW .

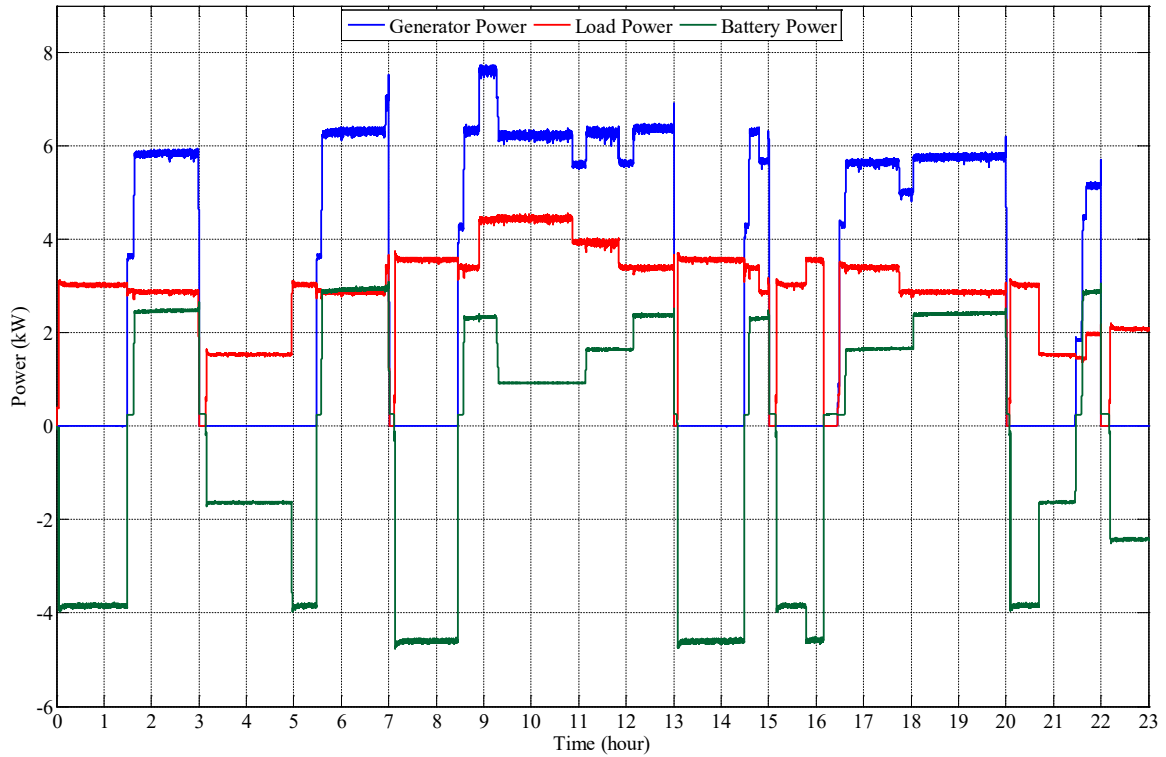


Figure 4.16. Generator power, load power and battery power.

Figure 4.17 shows bar diagram of theoretical and actual fuel consumed by the generator. The blue and orange bars represent theoretical and actual fuel consumed by the generator, respectively. The theoretical fuel consumption was obtained by substituting generator power in the generator fuel consumption curve. The actual fuel consumption was measured using the fuel flow meter in the laboratory. There was maximum difference of 8.93 ft^3 between the theoretical and actual fuel consumption. The values are tabulated in Table 4.3 as well. The energy consumed by load and that delivered by generator were estimated to be 71.3 kWh and 91 kWh , respectively. The net energy in the battery was computed to be 6.2 kWh . Then energy consumed by battery during charging was found to be 32.5 kWh and that delivered by the battery during discharging was found to be 26.3 kWh .

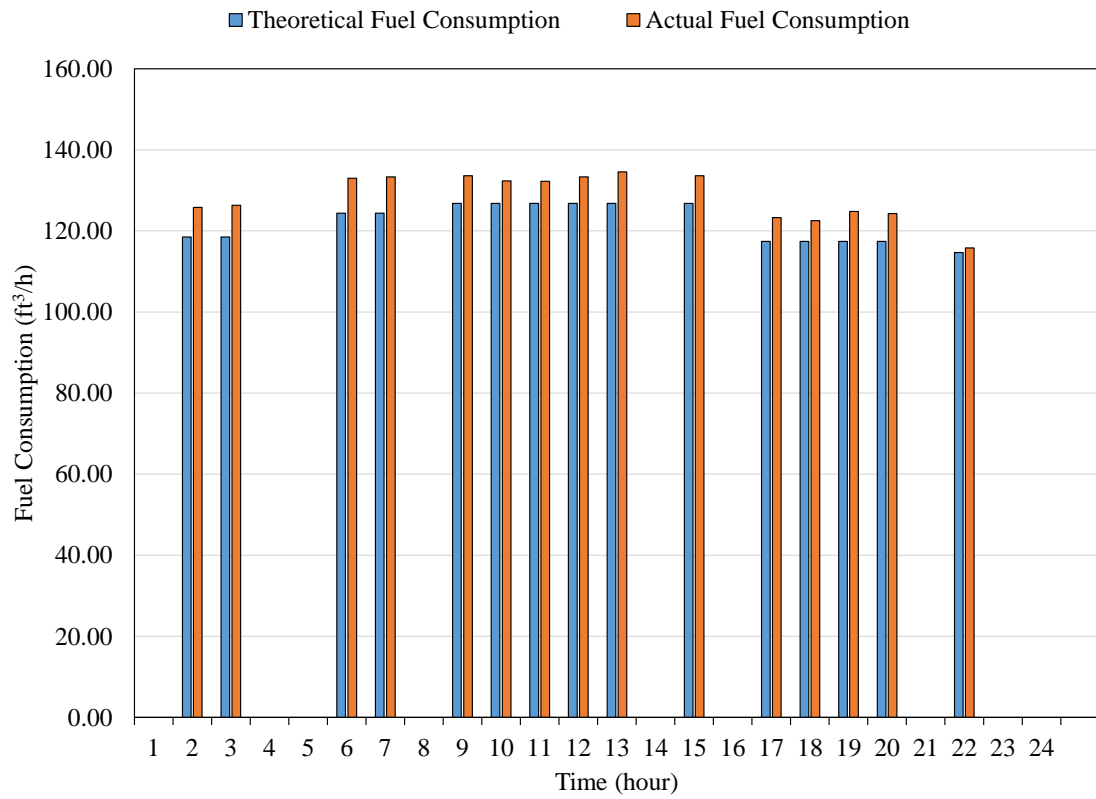


Figure 4.17. Comparison between theoretical and actual fuel consumed by the generator.

Table 4.3. Natural gas generator fuel consumption

Hour	Theoretical Fuel Consumption (ft^3)	Fuel flow meter reading (ft^3)
1	0.00	0.00
2	118.51	125.70
3	118.51	126.30
4	0.00	0.00
5	0.00	0.00
6	124.39	132.90
7	124.39	133.30
8	0.00	0.00
9	126.80	133.60
10	126.80	132.30
11	126.80	132.20
12	126.80	133.30
13	126.80	134.5
14	0.00	0.00
15	126.80	133.60
16	0.00	0.00
17	117.43	123.30
18	117.43	122.50
19	117.43	124.80
20	117.43	124.30
21	0.00	0.00
22	114.69	115.80
23	0.00	0.00
24	0.00	0.00

Figure 4.18 shows battery voltage profile for the 24 hour period. There was rise and fall in the voltage level during charging and discharging (inverting) modes. Similarly,

Figure 4.19 shows battery current profile. The negative battery current implies discharging

and the positive battery current implies charging.

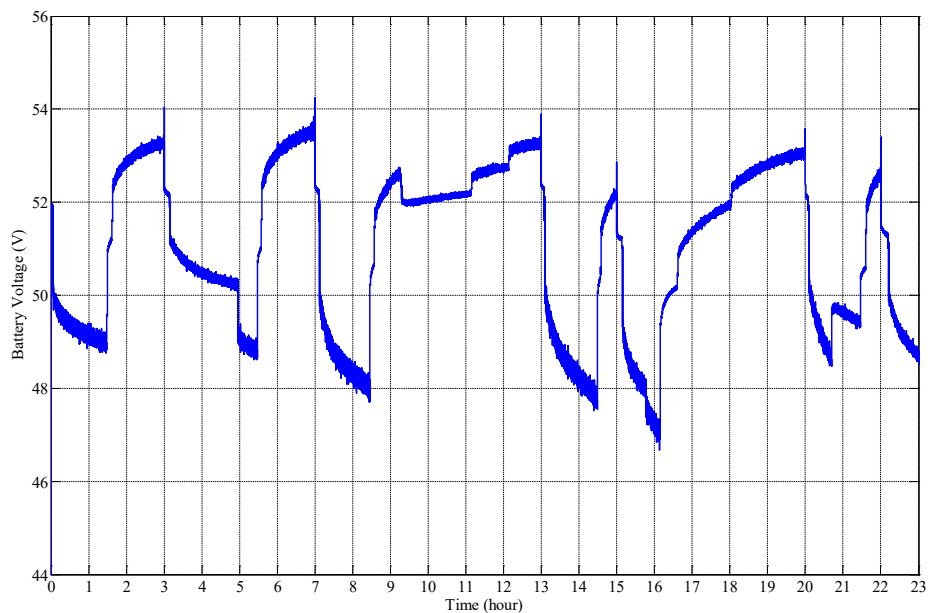


Figure 4.18. Plot of battery voltage versus time.

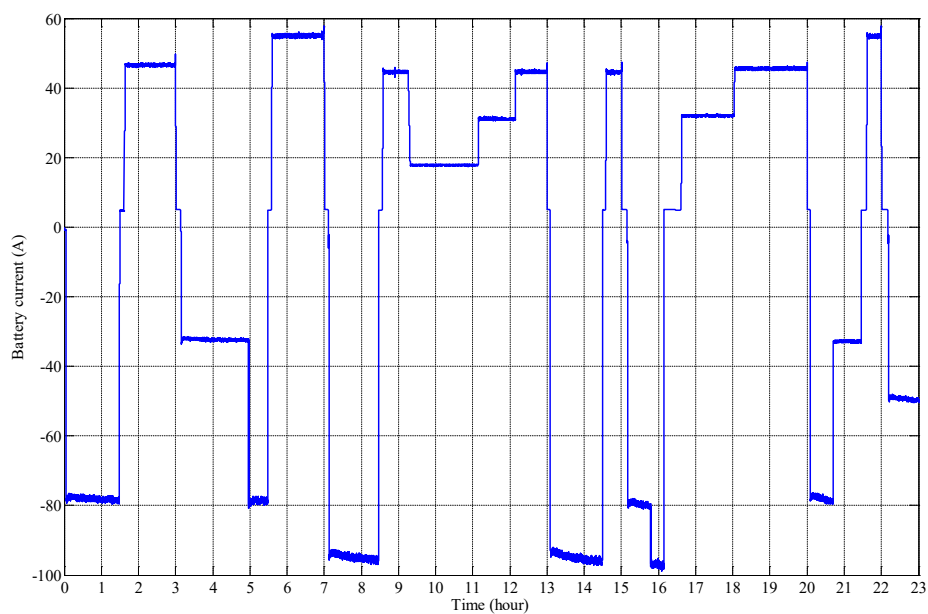


Figure 4.19. Plot of battery current versus time.

Figure 4.20 shows frequency of the natural gas generator. The frequency was 60 Hz when the generator was in operation and it was 0 Hz when the generator was turned OFF.

Figure 4.21 shows RMS value of generator voltage which was measured to be 240 V when the generator was in operation. Similarly, Figure 4.22 shows RMS value of generator current, which varied with variation in generator loading conditions.

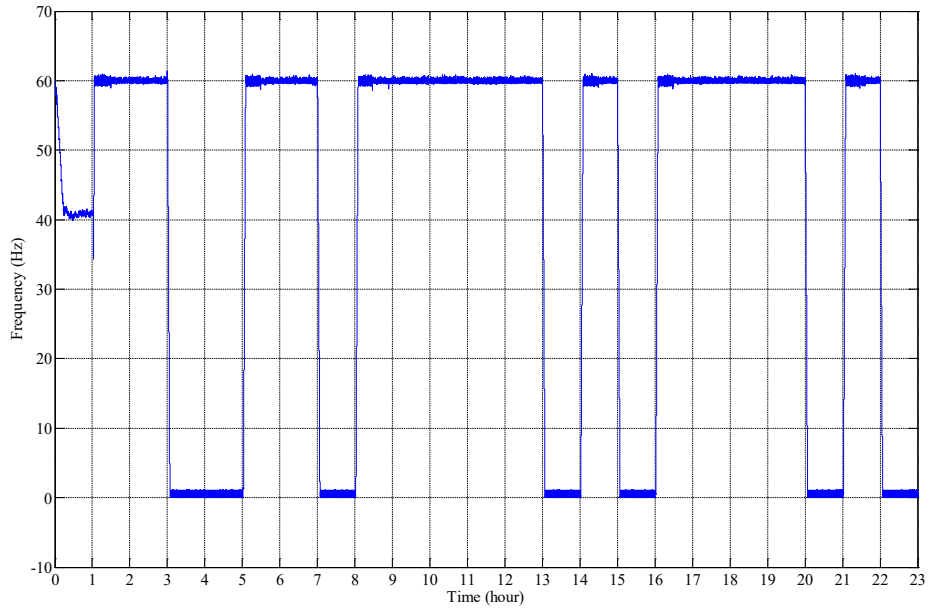


Figure 4.20. Plot of generator frequency versus time.

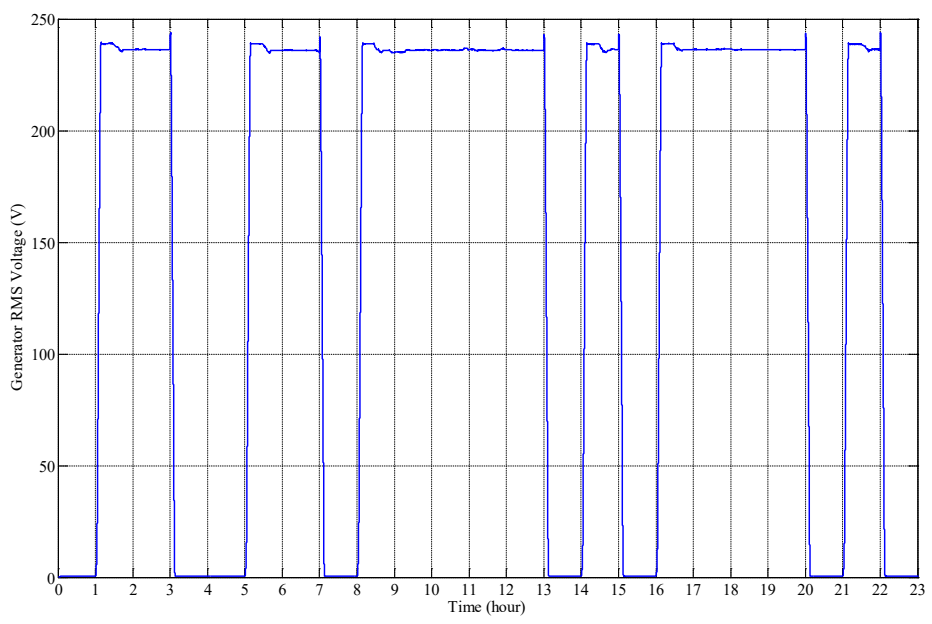


Figure 4.21. Plot of generator RMS voltage versus time.

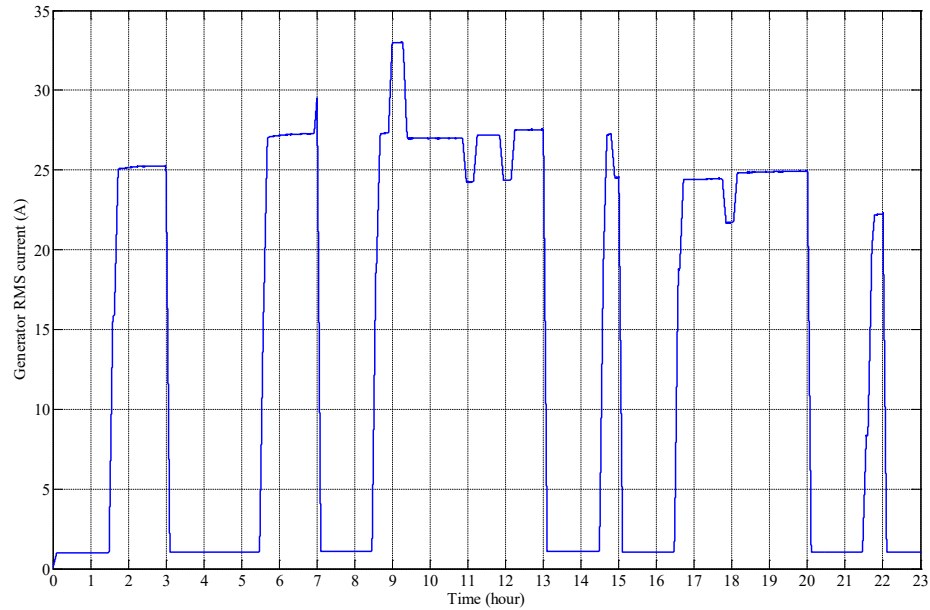


Figure 4.22. Plot of generator RMS current versus time.

Figure 4.23 shows load frequency for the 24 hour period. The frequency is about 60 Hz . There are some notches in the frequency profile. These notches are due to transition of sources from inverter to generator and vice-versa. Similarly, Figure 4.24 shows load voltage profile. The voltage is zero during the transition period. This is due to the fact that the hybrid inverter/charger takes some time to sense the participation of generator in the microgrid system. Likewise, Figure 4.25 shows the current drawn by the load for the 24 hour period.

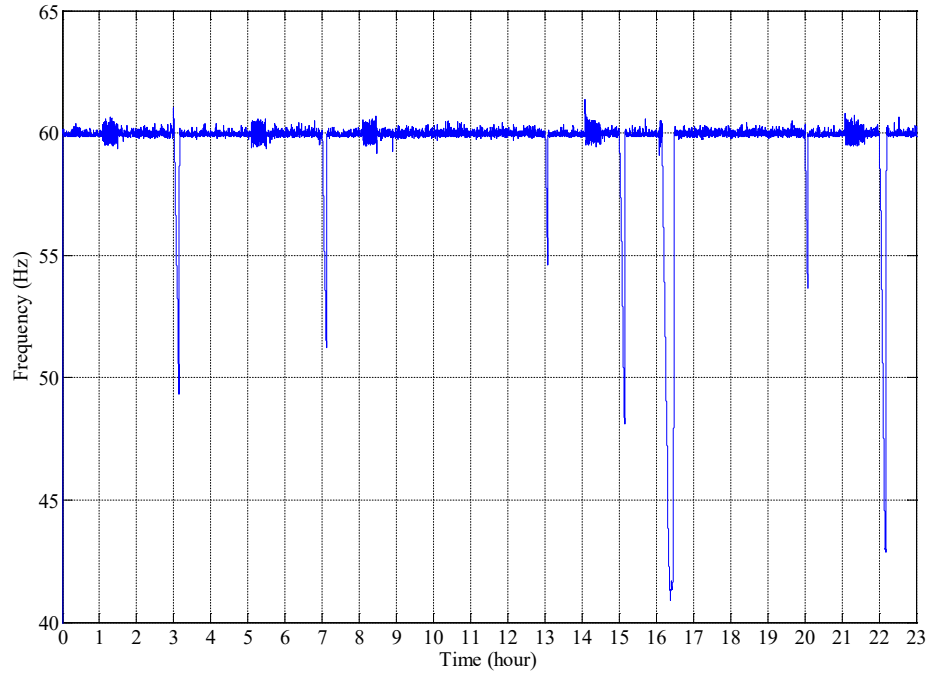


Figure 4.23. Plot of load frequency versus time.

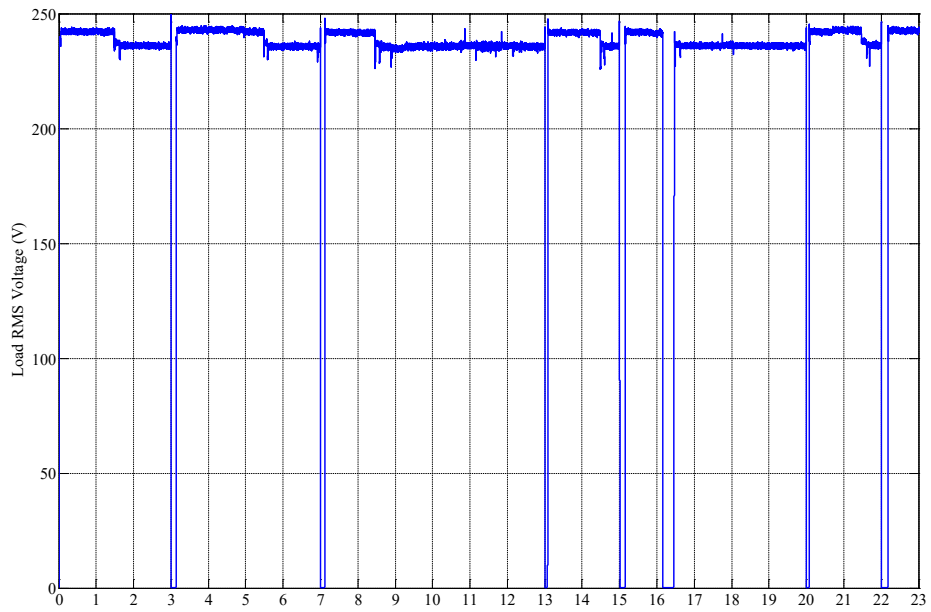


Figure 4.24. Plot of load RMS voltage versus time.

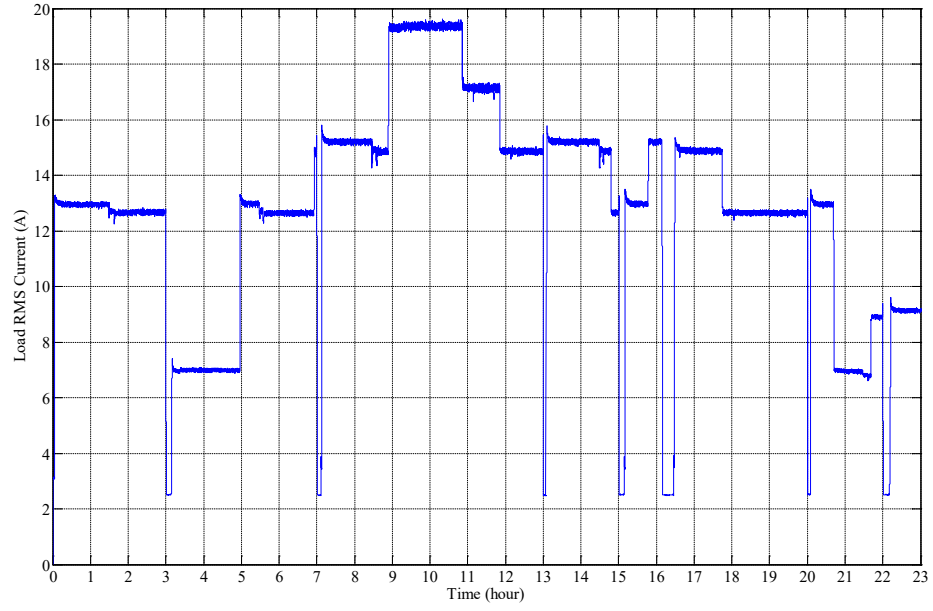


Figure 4.25. Plot of load RMS current versus time.

CHAPTER 5 CONCLUSIONS

5.1 Conclusions

A novel solar irradiance forecasting technique using MSM has been developed. The model uses historical irradiance data and gives a day ahead forecast. MSM was used to capture dynamic behavior of solar irradiance by permitting switching between the states. Based on the rotation of the earth around the sun and its own axis, periodicity is observed in data. This was captured by Fourier basis expansions. The deterministic irradiance value *i.e.*, *CSI* and the predicted Fourier basis expansions were used as independent variables, resulting in a fitted irradiance value for each state. A case study was conducted using a readily available historical irradiance data for Brookings, SD. The best model selected based on BIC had three regimes: referred as high, medium and low energy regimes for a day, corresponding to sunny, mildly cloudy and extremely cloudy days, respectively. The MAPE for the case study in Brookings for years 2001 through 2005 ranged between 30.7%-32.9% indicating that the model was not biased towards the data used for fitting. The average MAPE throughout the five years, was calculated to be 31.8%. The RMSE was found to be higher during summer months as there are more hours of sunlight in the summer. This forecasting technique mostly applies to remote locations where sophisticated forecasting techniques such as those based on satellite images and numerical weather prediction are not options. This method uses publicly and freely available past irradiance data for model fitting and once fitting is done, any further information is not required. The fitted model can be used for forecasting a number of years.

The irradiance forecasting method was successfully implemented in OPAL-RT

real-time digital simulator using solar panels as sensors. The first four hours of irradiance data were measured using the solar panels rather than using pyranometers as the sensors . A case study for real-time irradiance forecasting on June 9, 2015 in Brookings, SD showed RMSE and MAPE of $131.08 \text{ W}/\text{m}^2$ and 45.45%, respectively.

Only hourly solar irradiance was considered for forecasting purpose although there may exist intra-hour variations in the irradiance data. In a microgrid system, the intra-hour variations can be handled by using reserves. The hourly irradiance forecasts are used in the scheduling stage of the EMS in the microgrid system. The deviations in the forecasted and actual irradiance in real-time can be compensated in the dispatching stage using batteries and generators.

The EMS consisting of schedule and dispatch stages, was implemented in a laboratory scale single-phase microgrid testbed. The testbed comprised of central controller and easily available and cheaper COTS equipment. With the use of the COTS rather than customized equipment, the real performance of the system can be known. There were slight variations in the scheduled and dispatched values. The average power difference between the scheduled and the dispatched generator outputs were calculated to be 4.07 kW . Similarly, the average absolute power difference between the scheduled and the dispatched battery power was computed to be 0.48 kW . The difference between the scheduled and the dispatched values were taken into account by the generator and the energy storage system.

5.2 Future work

In this research work, it was observed that the forecasting error was fairly higher during summer months than during winter months. There were overestimation and underestimation in some particular months. As a future work, this trend in overestimation or underestimation among different months in a year can be taken into consideration to minimize the forecasting error. Likewise, in this thesis, Fourier basis expansions were considered to represent periodicity in irradiance. However, in future study, other basis expansion that gives lower forecasting error rate can be considered. In the scheduling layer of the EMS, the forecasting of load and PV power was considered ideal. In other words, the forecasted PV power was considered to be same as the actual PV power. Similarly, the forecasted load was considered to be same as the actual load. As a future work, the actual forecasted data can be considered to run the optimization in the EMS. Similarly, the developed EMS can be compared with other rule based EMS using the developed microgrid testbed.

REFERENCES

- [1] T. Mohn, "It takes a village: Rural electrification in east africa," *IEEE Power and Energy Magazine*, vol. 11, no. 4, pp. 46–51, 2013.
- [2] *Modern energy for all*, 2016. [Online]. Available: <http://www.worldenergyoutlook.org/resources/energydevelopment/> (Accessed: May 24, 2016).
- [3] *Energy access database*, 2015. [Online]. Available: <http://www.worldenergyoutlook.org/resources/energydevelopment/energyaccessdatabase/> (Accessed: May 24, 2016).
- [4] E. Hayden, "Introduction to microgrids," 2013.
- [5] C. Marnay, S. Chatzivasileiadis, G. Joos, C. Abbey, P. Lombardi, R. Iravani, P. Mancarella, and J. von Appen, "Microgrid evolution roadmap," in *2015 International Symposium on Smart Electric Distribution Systems and Technologies (EDST)*, IEEE, 2015, pp. 139–144.
- [6] A. Dehamna and P. Asmus, "Energy storage for microgrids," Navigant Research, Tech. Rep., 2014. [Online]. Available: <http://atargroup.com/blog/wp-content/uploads/2014/05/ESMG-14-Navigant-Research.pdf>.
- [7] S. Pelland, D. Turcotte, G. Colgate, and A. Swingler, "Nemiah valley photovoltaic-diesel mini-grid: System performance and fuel saving based on one year of monitored data," *IEEE Transactions on Sustainable Energy*, vol. 3, no. 1, pp. 167–175, 2012.
- [8] R. Tonkoski, *Impact of High Penetration of Photovoltaics on Low Voltage Systems and Remedial Actions*. LAP LAMBERT Academic Publishing, 2014.
- [9] S. Chakraborty, M. D. Weiss, and M. G. Simoes, "Distributed intelligent energy management system for a single-phase high-frequency ac microgrid," *IEEE Transactions on Industrial Electronics*, vol. 54, no. 1, pp. 97–109, 2007.
- [10] S. Chalise and R. Tonkoski, "Day ahead schedule of remote microgrids with renewable energy sources considering battery lifetime," in *2014 11th IEEE/IAS International Conference on Industry Applications (INDUSCON)*, IEEE, 2014, pp. 1–5.
- [11] E. Lorenz, T. Scheidsteger, J. Hurka, D. Heinemann, and C. Kurz, "Regional pv power prediction for improved grid integration," *Progress in Photovoltaics: Research and Applications*, vol. 19, no. 7, pp. 757–771, 2011.
- [12] S. Chalise, F. B. Dos Reis, J. Sternhagen, and R. Tonkoski, "Power management strategies for microgrids with high penetration of renewables," in *Fifth International Conference on Power and Energy Systems*, 2013, pp. 1–6.

- [13] D. E. Olivares, C. Cañizares, M. Kazerani, *et al.*, “A centralized optimal energy management system for microgrids,” in *Power and Energy Society General Meeting, 2011 IEEE*, IEEE, 2011, pp. 1–6.
- [14] M. N. S. Ariyasinghe and K. T. M. U. Hemapala, “Microgrid test-beds and its control strategies,” *Smart Grid and Renewable Energy*, vol. 4, no. 1, pp. 11–17, 2013.
- [15] S. Krishnamurthy, T. Jahns, and R. Lasseter, “The operation of diesel gensets in a certs microgrid,” in *2008 IEEE Power and Energy Society General Meeting-Conversion and Delivery of Electrical Energy in the 21st Century*, IEEE, 2008, pp. 1–8.
- [16] C. Wan, J. Zhao, Y. Song, Z. Xu, J. Lin, and Z. Hu, “Photovoltaic and solar power forecasting for smart grid energy management,” *CSEE Journal of Power and Energy Systems*, vol. 1, no. 4, pp. 38–46, 2015.
- [17] R. Perez, E. Lorenz, S. Pelland, M. Beauharnois, G. Van Knowe, K. Hemker, D. Heinemann, J. Remund, S. C. Müller, W. Traunmüller, *et al.*, “Comparison of numerical weather prediction solar irradiance forecasts in the us, canada and europe,” *Solar Energy*, vol. 94, pp. 305–326, 2013.
- [18] E. Geraldini, F. Romano, and E. Ricciardelli, “An advanced model for the estimation of the surface solar irradiance under all atmospheric conditions using msg/seviri data,” *IEEE transactions on geoscience and remote sensing*, vol. 50, no. 8, pp. 2934–2953, 2012.
- [19] H. M. Diagne, P. Lauret, and M. David, “Solar irradiation forecasting: State-of-the-art and proposition for future developments for small-scale insular grids,” in *WREF 2012-World Renewable Energy Forum*, 2012.
- [20] S. Pelland, J. Remund, J. Kleissl, T. Oozeki, and K. De Brabandere, “Photovoltaic and solar forecasting: State of the art,” *IEA PVPS, Task 14*, 2013.
- [21] R. Huang, T. Huang, R. Gadh, and N. Li, “Solar generation prediction using the arma model in a laboratory-level micro-grid,” in *2012 IEEE Third International Conference on Smart Grid Communications (SmartGridComm)*, IEEE, 2012, pp. 528–533.
- [22] P. Bacher, H. Madsen, and H. A. Nielsen, “Online short-term solar power forecasting,” *Solar Energy*, vol. 83, no. 10, pp. 1772–1783, 2009.
- [23] R. Perdomo, E. Banguero, and G. Gordillo, “Statistical modeling for global solar radiation forecasting in bogotá,” in *2010 35th IEEE Photovoltaic Specialists Conference (PVSC)*, IEEE, 2010, pp. 002 374–002 379.

- [24] A. Yona, T. Senjyu, A. Y. Saber, T. Funabashi, H. Sekine, and C.-H. Kim, "Application of neural network to one-day-ahead 24 hours generating power forecasting for photovoltaic system," in *International Conference on Intelligent Systems Applications to Power Systems, 2007. ISAP 2007.*, IEEE, 2007, pp. 1–6.
- [25] E. Lorenz, J. Hurka, D. Heinemann, and H. G. Beyer, "Irradiance forecasting for the power prediction of grid-connected photovoltaic systems," *IEEE Journal of Selected Topics in Applied Earth Observations and Remote Sensing*, vol. 2, no. 1, pp. 2–10, 2009.
- [26] Y. Huang, J. Lu, C. Liu, X. Xu, W. Wang, and X. Zhou, "Comparative study of power forecasting methods for pv stations," in *2010 International Conference on Power System Technology (POWERCON)*, IEEE, 2010, pp. 1–6.
- [27] A. Mellit and A. M. Pavan, "A 24-h forecast of solar irradiance using artificial neural network: Application for performance prediction of a grid-connected pv plant at trieste, italy," *Solar Energy*, vol. 84, no. 5, pp. 807–821, 2010.
- [28] C. Chen, S. Duan, T. Cai, and B. Liu, "Online 24-h solar power forecasting based on weather type classification using artificial neural network," *Solar Energy*, vol. 85, no. 11, pp. 2856–2870, 2011.
- [29] A. Yona, T. Senjyu, T. Funabashi, and C.-H. Kim, "Determination method of insolation prediction with fuzzy and applying neural network for long-term ahead pv power output correction," *IEEE Transactions on Sustainable Energy*, vol. 4, no. 2, pp. 527–533, 2013.
- [30] H.-T. Yang, C.-M. Huang, Y.-C. Huang, and Y.-S. Pai, "A weather-based hybrid method for 1-day ahead hourly forecasting of pv power output," *IEEE Transactions on Sustainable Energy*, vol. 5, no. 3, pp. 917–926, 2014.
- [31] S. M. Lurwan, N. Mariun, H. Hizam, M. A. M. Radzi, and A. Zakaria, "Predicting power output of photovoltaic systems with solar radiation model," in *2014 IEEE International Conference on Power and Energy (PECon)*, IEEE, 2014, pp. 304–308.
- [32] W. F. Holmgren, A. T. Lorenzo, M. Leuthold, C. K. Kim, A. D. Cronin, and E. A. Betterton, "An operational, real-time forecasting system for 250 mw of pv power using nwp, satellite, and dg production data," in *2014 IEEE 40th Photovoltaic Specialist Conference (PVSC)*, IEEE, 2014, pp. 0080–0084.
- [33] J. Liu, W. Fang, X. Zhang, and C. Yang, "An improved photovoltaic power forecasting model with the assistance of aerosol index data," *IEEE Transactions on Sustainable Energy*, vol. 6, no. 2, pp. 434–442, 2015.

- [34] B. M. Shah, A. Syahiman, H. Yokoyama, and N. Kakimoto, "High-precision forecasting model of solar irradiance based on grid point value data analysis for an efficient photovoltaic system," *IEEE Transactions on Sustainable Energy*, vol. 6, no. 2, pp. 474–481, 2015.
- [35] P.-J. Trombe, P. Pinson, and H. Madsen, "A general probabilistic forecasting framework for offshore wind power fluctuations," *Energies*, vol. 5, no. 3, pp. 621–657, 2012.
- [36] J. D. Hamilton, "A new approach to the economic analysis of nonstationary time series and the business cycle," *Econometrica: Journal of the Econometric Society*, vol. 57, pp. 357–384, 1989.
- [37] L. Rabiner and B.-H. Juang, *Fundamentals of Speech Recognition*. PTR Prentice-Hall, Inc., 1993.
- [38] R. Durbin, S. R. Eddy, A. Krogh, and G. Mitchison, *Biological sequence analysis: Probabilistic models of proteins and nucleic acids*. Cambridge University Press, 1998.
- [39] A. D. Sahin and Z. Sen, "First-order markov chain approach to wind speed modelling," *Journal of Wind Engineering and Industrial Aerodynamics*, vol. 89, no. 3, pp. 263–269, 2001.
- [40] A. Shamsad, M. Bawadi, W. W. Hussin, T. Majid, and S. Sanusi, "First and second order markov chain models for synthetic generation of wind speed time series," *Energy*, vol. 30, no. 5, pp. 693–708, 2005.
- [41] F. Y. Ettoumi, H. Sauvageot, and A.-E.-H Adane, "Statistical bivariate modelling of wind using first-order markov chain and weibull distribution," *Renewable Energy*, vol. 28, no. 11, pp. 1787–1802, 2003.
- [42] P. Ailliot and V. Monbet, "Markov-switching autoregressive models for wind time series," *Environmental Modelling & Software*, vol. 30, pp. 92–101, 2012.
- [43] P. Pinson, H. Madsen, P. E. Sørensen, and N. A. Cutululis, "Adaptive modelling of offshore wind power fluctuations," in *Proceedings of Nordic Wind Power Conference (NWPC)*, Citeseer, 2007.
- [44] K. Kazor and A. S. Hering, "Assessing the performance of model-based clustering methods in multivariate time series with application to identifying regional wind regimes," *Journal of Agricultural, Biological, and Environmental Statistics*, vol. 20, no. 2, pp. 192–217, 2015.
- [45] Y. Che, Z. Yang, and K. E. Cheng, "Construction, operation and control of a laboratory-scale microgrid," in *3rd International Conference on Power Electronics Systems and Applications, 2009. PESA 2009*, IEEE, 2009, pp. 1–5.

- [46] F. Guo, L. Herrera, M. Alsolami, H. Li, P. Xu, X. Lu, A. Lang, J. Wang, and Z. Long, "Design and development of a reconfigurable hybrid microgrid testbed," in *2013 IEEE Energy Conversion Congress and Exposition*, IEEE, 2013, pp. 1350–1356.
- [47] D. EERE, "Summary report: 2012 doe microgrid workshop," *Chicago, Illinois, Jul*, 2012.
- [48] W. Su and J. Wang, "Energy management systems in microgrid operations," *The Electricity Journal*, vol. 25, no. 8, pp. 45–60, 2012.
- [49] The Smart Grid Observer, *Remote microgrids sector poised for growth*, 2012. [Online]. Available: <http://www.smartgridobserver.com/n6-15-12-1.htm> (Accessed: May 23, 2016).
- [50] P. Asmus, "State of islanded grids-prospects, progress, and market insights," Navigant Research, Tech. Rep., 2015. [Online]. Available: http://www.islandedgrid.org/wp-content/uploads/2015/03/ISLANDEDGRID_ALL_PRESENTATIONS_Alaska-3-5-15.pdf (Accessed: May 23, 2016).
- [51] D. E. Olivares, C. A. Cañizares, and M. Kazerani, "A centralized optimal energy management system for microgrids," in *2011 IEEE Power and Energy Society General Meeting*, IEEE, 2011, pp. 1–6.
- [52] J. Belanger, P. Venne, and J. Paquin, "The what, where and why of real-time simulation," *2010 IEEE Power and Energy Society General Meeting*, vol. 1, no. 13, pp. 37–49, 2010.
- [53] L.-F. Pak, M. O. Faruque, X. Nie, and V. Dinavahi, "A versatile cluster-based real-time digital simulator for power engineering research," *IEEE Transactions on Power Systems PWRS*, vol. 21, no. 2, p. 455, 2006.
- [54] HowStuffWorks. (2016). What are natural gas generators? [Online]. Available: <http://auto.howstuffworks.com/fuel-efficiency/fuel-saving-devices/natural-gas-generator.htm>.
- [55] ClarkeEnergy, *Ge's jenbacher gas engines*, 2016. [Online]. Available: <https://www.clarke-energy.com/contact/>.
- [56] B. Lawson, *Gas turbine power plants*, 2015. [Online]. Available: http://www.mpoweruk.com/gas_turbines.htm.
- [57] J. Zhu, *Optimization of power system operation*. John Wiley & Sons, 2015, vol. 47.
- [58] R. Tonkoski, "Impact of high penetration of photovoltaics on low voltage systems and remedial actions," PhD thesis, Concordia University, 2011.

- [59] *How to construct a simple solar cell? (step by step) — basic operating principle of photovoltaic cell*, 2005. [Online]. Available: <http://www.electricaltechnology.org/2015/06/how-to-make-a-solar-cell-photovoltaic-cell.html>.
- [60] R. A. Messenger and J. Ventre, *Photovoltaic systems engineering*. CRC press, 2010.
- [61] J. Cubas, S. Pindado, and C. de Manuel, “Explicit expressions for solar panel equivalent circuit parameters based on analytical formulation and the lambert w-function,” *Energies*, vol. 7, no. 7, pp. 4098–4115, 2014.
- [62] HOMER. (2015). *Homer Energy*, [Online]. Available: <http://www.homerenergy.com>.
- [63] evergreensolar, “Es-a series photovoltaic panels 200, 205 and 210 w,” evergreensolar, Tech. Rep., 2009.
- [64] SMA America, *Pv inverter sunny boy 5000-us/6000-us/7000-us/8000-us installation manual*, English, SMA America, 2011, 104 pp.
- [65] X. Guan, Z. Xu, and Q.-S. Jia, “Energy-efficient buildings facilitated by microgrid,” *IEEE Transactions on Smart Grid*, vol. 1, no. 3, pp. 243–252, 2010.
- [66] International Battery, “48 vdc 8.2 kwh energy storage system - ess user manual ib 48v 016 ess 160 ah,” International Battery, Inc., Tech. Rep., 2011.
- [67] Schneider Electric, *Xantrex xw hybrid inverter/charger installation guide*, English, Schneider Electric, 2010, 68 pp.
- [68] R. I. Davis, A. Burns, R. J. Brill, and J. J. Lukkien, “Controller area network (can) schedulability analysis: Refuted, revisited and revised,” *Real-Time Systems*, vol. 35, no. 3, pp. 239–272, 2007.
- [69] L. Wolfhard, *Can system engineering: From theory to practical application*, 1997.
- [70] T. Logenthiran, D. Srinivasan, A. M. Khambadkone, and H. N. Aung, “Multiagent system for real-time operation of a microgrid in real-time digital simulator,” *IEEE Transactions on Smart Grid*, vol. 3, no. 2, pp. 925–933, 2012.
- [71] Q. Jiang, M. Xue, and G. Geng, “Energy management of microgrid in grid-connected and stand-alone modes,” *IEEE Transactions on Power Systems*, vol. 28, no. 3, pp. 3380–3389, 2013.
- [72] J. Driesen and F. Katiraei, “Design for distributed energy resources,” *IEEE Power and Energy Magazine*, vol. 6, no. 3, pp. 30–40, 2008.
- [73] R. Billinton and R. N. Allan, *Reliability evaluation of power systems*. Springer Science & Business Media, 2013.
- [74] M. Wang and H. Gooi, “Spinning reserve estimation in microgrids,” *IEEE Transactions on Power Systems*, vol. 26, no. 3, pp. 1164–1174, 2011.

- [75] W. Su, J. Wang, and J. Roh, “Stochastic energy scheduling in microgrids with intermittent renewable energy resources,” *IEEE Transactions on Smart Grid*, vol. 5, no. 4, pp. 1876–1883, 2014.
- [76] A. B. Meinel and M. P. Meinel, *Applied solar energy. An introduction*. Addison-Wesley Publishing Co., Reading, MA, 1976.
- [77] Photovoltaic Education Network. (2013). Declination angle, [Online]. Available: <http://www.pveducation.org/pvcdrom/properties-of-sunlight/declination-angle>.
- [78] J. A. Duffie and W. A. Beckman, *Solar engineering of thermal processes*. John Wiley and Sons, Inc., 2013, vol. 4.
- [79] J. O. Ramsay, *Functional data analysis*. Wiley Online Library, 2006.
- [80] C. M. Kuan, “Lecture on the markov switching model,” *Institute of Economics Academia Sinica*, pp. 1–30, 2002.
- [81] A. P. Dempster, N. M. Laird, and D. B. Rubin, “Maximum likelihood for incomplete data via the EM algorithm (with discussion),” *Journal of the Royal Statistical Society, Series B*, vol. 39, pp. 1–38, 1977.
- [82] J. A. Sanchez-Espigares and A. Lopez-Moreno, *Mswm: Fitting markov switching models*, R package version 1.2, 2014. [Online]. Available: <https://CRAN.R-project.org/package=MSwM>.
- [83] G. Schwarz, “Estimating the dimensions of a model,” *Annals of Statistics*, vol. 6, pp. 461–464, 1978.
- [84] S. Chalise, “Power management of remote microgrids considering battery lifetime,” PhD thesis, South Dakota State University, Brookings, South Dakota, USA, 2016.
- [85] Clean Power Research. (2016). Solaranywhere data, [Online]. Available: <http://www.solaranywhere.com>.
- [86] A. Kankiewicz, W. Kirkland, J. Dise, E. Wu, and R. Perez, “Solar 2014: Reducing solar project uncertainty with an optimized resource assessment tuning methodology,”
- [87] S. Chalise, J. Sternhagen, T. Hansen, and R. Tonkoski, “Energy management of remote microgrids considering battery lifetime,” *The Electricity Journal*, 2016.
- [88] Photovoltaic Education Network. (2013). Solar radiation on a tilted surface, [Online]. Available: <http://www.pveducation.org/pvcdrom/properties-of-sunlight/solar-radiation-on-tilted-surface>.
- [89] S. R. Wenham, M. A. Green, M. E. Watt, R. P. Corkish, and A. B. Sproul, *Applied Photovoltaics*. Earthscan, 2012.
- [90] SMA America, “Pv inverter sunny boy 5000-us/6000-us/7000-us/8000-us,” SMA America, Tech. Rep., 2011.

- [91] A. P. Dobos, "Pvwatts version 5 manual," *National Renewable Energy Laboratory*, September, 2014.
- [92] F. Mak, R. Sundaram, V. Santhaseelan, and S. Tandle, "Laboratory set-up for real-time study of electric drives with integrated interfaces for test and measurement," in *2008 38th Annual Frontiers in Education Conference*, IEEE, 2008, pp. 1–6.
- [93] T. A. Loehlein, "Maintenance is one key to diesel generator set reliability," Cummins Power Generation, Tech. Rep.